AIRCRAFT DESIGN WITH ACTIVE LOAD ALLEVIATION AND NATURAL LAMINAR FLOW

A DISSERTATION
SUBMITTED TO THE DEPARTMENT OF AERONAUTICS & ASTRONAUTICS
AND THE COMMITTEE ON GRADUATE STUDIES
OF STANFORD UNIVERSITY
IN PARTIAL FULFILLMENT OF THE REQUIREMENTS
FOR THE DEGREE OF
DOCTOR OF PHILOSOPHY

Jia Xu
March 2012

© 2012 by Jia Xu. All Rights Reserved.

Re-distributed by Stanford University under license with the author.

This work is licensed under a Creative Commons Attribution-Noncommercial 3.0 United States License.
http://creativecommons.org/licenses/by-nc/3.0/us/

This dissertation is online at: http://purl.stanford.edu/hz528zb1688

I certify that I have read this dissertation and that, in my opinion, it is fully adequate in scope and quality as a dissertation for the degree of Doctor of Philosophy.

Ilan Kroo, Primary Adviser

I certify that I have read this dissertation and that, in my opinion, it is fully adequate in scope and quality as a dissertation for the degree of Doctor of Philosophy.

Juan Alonso

I certify that I have read this dissertation and that, in my opinion, it is fully adequate in scope and quality as a dissertation for the degree of Doctor of Philosophy.

Antony Jameson

Approved for the Stanford University Committee on Graduate Studies.

Patricia J. Gumport, Vice Provost Graduate Education

This signature page was generated electronically upon submission of this dissertation in electronic format. An original signed hard copy of the signature page is on file in University Archives.

Abstract

In this thesis we incorporate maneuver load alleviation (MLA), gust load alleviation (GLA), and natural laminar flow (NLF) into aircraft conceptual design. While existing conceptual design frameworks tend to reduce the impact of these technologies to empirical weight and drag corrections, the present work uses physics-based methods to capture the dynamic interplay among natural laminar flow and load alleviation. The results demonstrate that the simultaneous application of MLA and GLA can tilt the balance of the transonic Mach-sweep-thickness ($M\Lambda T$) trade in favor of high aspect ratio, low-sweep natural laminar flow wings. A minimum cost turbulent aircraft designed concurrently with MLA and GLA control systems can achieve a significant 10% reduction in fuel burn and 3.4% reduction in cost relative to a baseline design without load control. The fuel and cost savings grow to 15% and 5% respectively when we introduce natural laminar flow into the design process. Sensitivity studies confirm that the control and actuator requirements of effective active load alleviation are consistent with the performance parameters of modern aircraft. Results also suggest that the combination of aggressive active load control and low-sweep NLF wing can be a viable alternative to a 3-D NLF wing design or complex active laminar flow control (LFC) schemes. Finally, the aeroservoelastic conceptual design framework developed in this thesis can serve as a platform for assessing future aircraft configurations and operational paradigms aimed at reducing aircraft fuel consumption and environmental impact.

This dissertation is dedicated to my parents Sarah and Yan;
and to my loving wife, Donna

Acknowledgments

My deepest gratitude goes to my advisor, Professor Ilan Kroo, who has taught me by example to seek out interesting questions and pursue them with rigor, intensity and integrity. I shall miss the precious *ah-ha* moments in our conversations about research and aircraft design

I would like to thank my committee members Professor Jameson and Professor Alonso. I shall miss my discussions with Professor Jameson on all things airplane. It was my honor and pleasure to be his course assistant in the well-loved Case Studies in Aircraft Design. Professor Alonso has always been there with incisive comments and timely encouragement. I am deeply grateful for the long discussions on both research and career paths. It is also entirely possible that I only learned aerodynamics by working with him on AA200B.

I want to thank Dr. Steve Smith for serving on my oral committee and for his leadership and insights in the NASA NRA that ultimately led to this thesis. Professor David Freyberg responded enthusiastically to my last-minute request for an oral examination chair. I am grateful for his time and for his questions and perspectives in the examinations.

I am deeply indebted to the members of the Aircraft Design Group. Most of all I thank Tristan Flanzer, Andrew Ning, Geoff Bower and Emily Schwartz. The FYI team effort was a highlight of my years at Stanford. I am grateful and proud to have you all as friends. While we were cruelly robbed of our 30,000€ prize money, what I cherish in its place are the priceless adventures and laughters – I will always

have Paris with my friends. I reserve a very special thanks to Tristan and Elyssa, for feeding me, for listening, and for being such awesome human beings. My best wishes for the two of you in all of life's journeys.

My experience at Stanford would be rendered incomplete – perhaps all too literally – without the words of wisdom and encouragement from Mathias Wintzer and Sara Smoot. I shall miss our long conversations. The same is true of former ADG members Peter Sturdza, Dev Rajnarayan and Brian Roth. And many thanks go to Alex Haas and Alex Stoll for the enlightening discussions.

A special thanks Aero/Astro alum Prasun Bansal for his joviality, hospitality, and for his long, arduous journey across the Himalayas (by Boeing 777) to my wedding.

I am indebted to the miracle workers in the Aero/Astro office. I want to give a big thanks to Jay Subramanian and Robin Murphy for their patience with my consistent procrastinations on all matters paperwork and deadline. I thank Ralph Levine, the departmental manager, for his constant encouragements, and for lunch.

I am grateful for the generous support from the National Science Foundation, the NASA Subsonic Fixed Wing Program and Airbus. I owe much to mentors and advocates beyond Stanford: Professor Jewel Barlow at the University of Maryland, Professors P.K.Yeung, Jerry Seitzman and Carol Senf at Georgia Tech, and Professor Christopher Coker at the LSE. I am forever indebted to the Marshall Aid Commemoration Commission for the opportunity of a lifetime to study in the UK.

Most importantly, none of this would have been possible without the unconditional love and tireless patience of my parents. My dream may have be an impossible one without their courage to start life anew in this once foreign land. And they, more than anyone else, have had to endure too many Christmases, thanksgivings and Chinese New Years without their son by their side.

Finally, I could not have walked this far without the constant, enveloping love of my dear wife Donna. And the journey would be rendered meaningless without her. Thanks to Donna I live with the joy and anticipation of a soon-to-be father. Why

built airplanes if not to see the faces of our loved ones that much faster; why travail in life if not to see the same people made happy and safe. Finally, it bears mention that this thesis would not be complete without Donna's patience, encouragements, warm hugs, and her timely realization that the deadline for thesis submission is in fact in two weeks.

Contents

List of Tables

List of Figures

Nomenclature

$\boldsymbol{x_{aircraft}}$	Aircraft design variables
$\boldsymbol{x_{CG}}$	Vector of longitudinal center-of-gravity positions for all flight conditions
$\boldsymbol{x_{GLA}}$	GLA design variables
$\boldsymbol{x_{mission}}$	Mission variables
$\boldsymbol{x_{MLA}}$	MLA design variables
$\boldsymbol{x_{pressure}}$	Pressure design variables
$\boldsymbol{x_{transition}}$	Transition design variables
$\boldsymbol{x_{wing}}$	Wing design variables
$\bar{\boldsymbol{C}}$	Modal damping matrix
$\bar{\boldsymbol{K}}$	Modal stiffness matrix
$\bar{\boldsymbol{M}}$	Modal mass matrix
$\bar{\boldsymbol{Q}}$	Orthonormal basis for modal decomposition
$\boldsymbol{C}$	Global damping matrix
$\boldsymbol{K}$	Global stiffness matrix
$\boldsymbol{L}$	Triangular Cholesky factorization matrix
$\boldsymbol{M^e}$	Element mass matrix
$\boldsymbol{M}$	Global mass matrix
$\boldsymbol{u}$	Generalized displacement
$\frac{dC_p}{dx}_l$	Lower surface airfoil pressure gradient
$\frac{dC_p}{dx}_u$	Upper surface airfoil pressure gradient
$\frac{D}{T}$	Drag-to-thrust ratio
κ_{if}	Inflation index

ν	Kinematic viscosity
$\overline{c}$	Mean aerodynamic chord
$\overline{C_p}$	Canonical pressure coefficient
$\tilde{C}_{p_l}$	Airfoil lower surface C_p in sweep-taper system
$\tilde{C}_{p_u}$	Airfoil upper surface C_p in sweep-taper system
$\tilde{u}_l$	Airfoil lower surface velocity in sweep-taper system
$\tilde{u}_u$	Airfoil upper surface velocity in sweep-taper system
A	Element cross section area
AR	Trapezoidal wing aspect ratio
c_a	Airplane cost (excluding engines)
c_a	The airplane cost
c_e	Engine cost
c_{ce}	engine material cost per flight hour
c_{he}	engine material cost per flight cycle
c_{tic}	Estimated ticket cost
D_a	Depreciation period (years)
E	Young's modulus
F	Generalized forces
f	Modal forcing
F_g	Gust alleviation factor
H	Boundary layer shape factor
h	Gust gradient length
h_c	Second segment climb gradient
H_{te}	Shape factor at trailing edge
I	Cross-section inertia
I_{ra}	Insurance rate
K^e	Element stiffness matrix
k_d	GLA derivative gain
k_p	GLA proportional gain
L	Element length
l_{land}	Landing field length

l_{to}	Balanced takeoff field length
LF	Load factor)
M_{dd}	Airfoil drag divergence Mach number
M_{land}	Landing Mach number
M_{to}	Takeoff Mach number
n	Load factor
N_e	Number of engines
N_{pax}	Passenger count
p_{fuel}	Price of aviation fuel ($\$/gal$)
p_{oil}	Price of lubrication oil ($\$/lb$)
R	Aircraft mission range
R_{req}	Required mission range
RF	Range factor
S	Stratford concavity parameter
s	Airfoil surface coordinate
S_h	Horizontal tail area
S_u	Upper surface Stratford concavity parameter
S_{ref}	Trapezoidal wing reference area
$t(x)$	Airfoil thickness distribution
T_0	Sea-level static engine thrust
T_m	Air and ground maneuver time
t_s	Wing box skin gauge thickness
t_w	Wing box web gauge thickness
t_{ce}	Labor man-hours per flight hour
T_{cl}	Climb time
t_{he}	Labor man-hours per flight cycle
t_{inv}	Airfoil thickness distribution from the inverse solution
$TSFC$	Thrust specific fuel consumption
U_a	Annual utilization
u_e	External velocity
u_r	Velocity at the start of recovery

U_{ds}	1–Cosine design gust amplitude
U_{ref}	Gust reference vertical design velocity
u_{te}	Velocity at trailing edge
V	Cruise velocity
V_{block}	Block speed
W_e	Engine dry weight
W_f	Final cruise weight
w_g	Gust vertical velocity
W_i	Initial cruise weight
W_{MLW}	Maximum landing weight (lb)
W_{MTOW}	Maximum takeoff weight
W_{MZFW}	Maximum zero-fuel weight
x	Effective boundary layer length
x_a	Longitudinal position of aft spar in the airfoil system
x_e	Longitudinal position of elastic axis in the airfoil system
x_f	Longitudinal position of forward spar in the airfoil system
x_t	Longitudinal location of transition in aircraft system
x_{mg}	Longitudinal position of main landing gear
x_{ng}	Longitudinal position of the nose gear
x_{root}	Longitudinal position of wing root
x_{TE}	Airfoil trailing edge
$z(x)$	Airfoil camber distribution
z_f	Final cruise altitude
z_i	Initial cruise altitude
z_{max}	Maximum operational altitude (ft)
$\overline{Re}_x$	Effective local Reynolds number
θ_{te}	Momentum thickness at trailing edge
C_{Lh}	Horizontal tail lift coefficient
$C_{l_{inv}}$	Airfoil C_l from the inverse
$C_{l_{max}}$	Section maximum lift coefficient
C_{Mac}	Pitching moment about aerodynamic center

$L_{e\delta_4}$	Elastic wing pitch moment due to aileron deflection
$L_{r\delta_4}$	Rigid wing pitch moment due to aileron deflection
Re_x	Local Reynolds number
$Re_{\exp 9}$	Local transition Reynolds number as predicted by e^9 fits
Re_{e^9}	Transition Re_x as predicted by e^9 fits.
RF_f	Final cruise range factor
RF_i	Initial cruise range factor
R_L	Labor rate $/hr
t_{ha}	Labor man-hours per flight hour
C_{Lhmax}	Maximum horizontal tail lift coefficient
$C_{p_{LEl}}$	Lower surface airfoil leading edge C_p
$C_{p_{LEu}}$	Upper surface airfoil leading edge C_p
AIC	Aerodynamic influence coefficient matrix
TSFC_0	Sea-level static TSFC
α_0	Zero-lift angle of attack
α_i	Local angle of attack at panel i
β	Prandtl-Glauert correction factor
$\boldsymbol{\delta}$	Flap deflections in between breakpoints
δ_i	Control surface deflection for channel i
Δc	Wing trailing edge extension ratio
δ_s	Slat deflection
η	Dimensionless span $\eta = y/(b/2)$
$\frac{d\delta_i}{dt}$	Control surface deflection rate for channel i
Γ_i	Circulation at panel i
λ	Trapezoidal wing taper ratio
$\Lambda_{1/4}$	Trapezoidal wing quarter-chord sweep
ν	Kinematic viscosity
ω	Wing natural frequency
ρ	Element mass density
σ	Bending stress
τ	Shear stress

θ	Wing jig twist
$\tilde{\tau}_{\delta_4}$	Wing torque due to aileron deflection
ζ	Damping ratio
δ_{land}	Landing flap deflection
δ_{to}	Takeoff flap deflection
σ_a	Allowable bending stress
τ_a	Allowable shear stress

Chapter 1

Introduction

1.1 Motivation

The classical Breguet Range equation decomposes aircraft range and hence, cruise efficiency into propulsive ($TSFC$), structural (W_i/W_f) and aerodynamic (L/D) components:

$$R = \left(\frac{L}{D}\right) \frac{V}{TSFC} \ln\left(\frac{W_i}{W_f}\right) \tag{1.1}$$

One can certainly improve the individual terms in the range equation: Historically, the most significant improvements in jet aircraft efficiency have come from improvements in the propulsive term associated with the development of high-bypass turbofan engines. The expanding use of high-strength composites can increase the weight fraction. And configuration changes such as increased wingspan can lead to improved L/D. However, the integrated nature of the aircraft design means that few substantive configuration changes can be made without incurring some multidisciplinary trade-offs. Increasing the wingspan for example also increases the wing weight.

Yet the same integrated nature of aircraft design is also an opportunity: significant improvements can come from configurations that can *simultaneously* exploit aerodynamic, control and structural advances to improve efficiency. The Boeing/NASA Sugar

Volt pictured in fig. 1.1 is one such multidisciplinary design concept. Developed as part of the NASA N+3 studies to envision future airliners, the Sugar Volt deploy a slew of advanced technologies from hybrid-electric open rotor engines to truss-braced wings (TBW) to greatly improve cruise efficiency and enviromental performance.[1]

Figure 1.1. The Boeing Sugar Volt – part of the NASA N+3 advanced subsonic transport study.[1]

The focus of this thesis is on the Sugar Volt's combination of extreme span and extensive natural laminar flow (NLF) – all made possible by the aggressive application of maneuver (MLA) and gust load alleviation (GLA). The combination of these technologies holds the potential to greatly improve both the weight and aerodynamic terms in the Breguet equation. However, the potential gains from a complex and highly coupled design like the Sugar Volt can be difficult to quantify. Conceptual design tools typically reduce laminar flow and active load alleviation to empirical technology factors applied on weight and drag.[1,3,4] The Sugar Volt design for example assumes that a properly designed active load alleviation system can reduce the wing weight by 25%. It also assumes that the wing transition Reynolds number lies somewhere between 15 to 17 million irrespective of the pressure distribution over the wing.[1] An empirical approach however can miss important trade-offs and constraints that drive the design: the effectiveness of load alleviation systems can be constrained by maximum lift, wing aeroelastic response and control power. And the design of a transonic NLF wing is driven by a balancing act to control profile drag, structural

weight and compressibility effects.

The objective of this research is to develop a new design framework that leverage physic-based methods to incorporate active load alleviation and natural laminar flow into conceptual design.

1.2 Natural Laminar Flow

Viscous drag accounts for upwards of half of the total aircraft drag in cruise. Achieving extensive laminar flow over the wings net significant drag reductions. One way to maintain laminar flow at high Reynolds numbers is to employ active laminar flow control (LFC) to reshape the pressure distribution, re-energize the boundary layer and delay flow transition. The notional geometry and pressure distribution of an active laminar flow control airfoil is shown in fig. 1.2. Active flow control systems however can incur significant weight, maintenance and power penalties.

An alternative to active LFC is to design the wing pressure distribution to *passively* stabilize the boundary layer, which gives rise to natural laminar flow (NLF). There is a substantial body of literature that aims to solve the NLF wing design problem using high fidelity tools.[5–9] However, these methods often require detailed definitions of the wing geometry, which may not be practical in the early stages of design. This has led aircraft designers to use empirical, design-oriented fits of flow transition in aircraft design problems.[4,10]

Yet the impact of laminar flow can be fundamental. And laminar flow wing design should be formally integrated into conceptual design. The potential fuel savings from airliners designed with NLF wings have been variously quoted as somewhere between 5-12%.[11–13] The extent of the fuel savings is subject to complex multidisciplinary trade-offs. The most important of which involves wing sweep.

In two dimensions an NLF airfoil can be designed with extended regions of flow acceleration to suppress streamwise Tollmien-Schlichting (TS) instabilities. In the

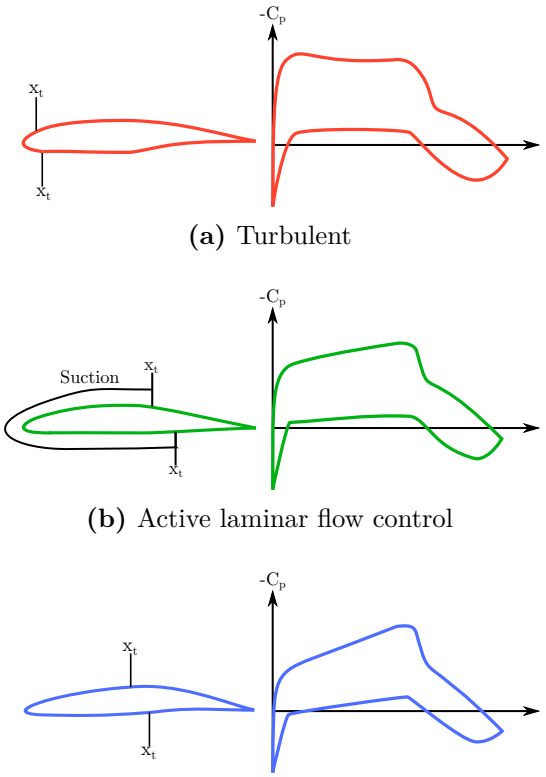

(a) Turbulent

(b) Active laminar flow control

(c) Natural laminar flow (NLF)

Figure 1.2. Representative airfoil geometries and C_p distributions.

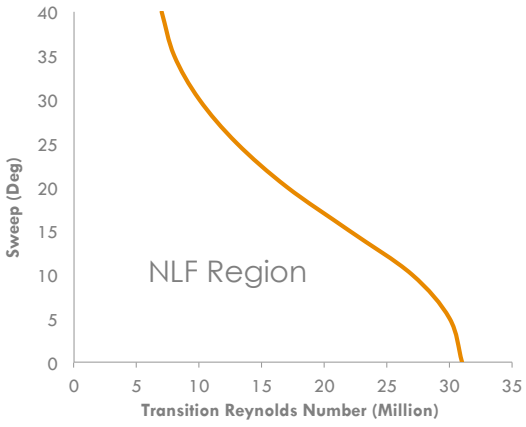

Figure 1.3. A plot of NLF transition as a function of wing sweep based on the results of historical laminar flow experiments.[2]

case of swept wings there exists a fundamental trade-off between the need to stabilize the streamwise and crossflow (CF) boundary layers: while flow acceleration stabilizes the streamwise boundary layer, it has the opposite, destabilizing effect on crossflow. The implication is that extensive natural laminar flow becomes progressively more difficult to maintain at higher wing sweep. Indeed flight tests demonstrate that at a sweep of 10° laminar flow can be reasonably achieved over 50% of a NLF wing. However, if sweep is increased to 25° then the laminar region is reduced to just 20% of the wing area.[11] The trend of reduced laminar flow with increasing sweep is also demonstrated by the complication of four decades of NLF flight test results in fig. 1.3.[2]

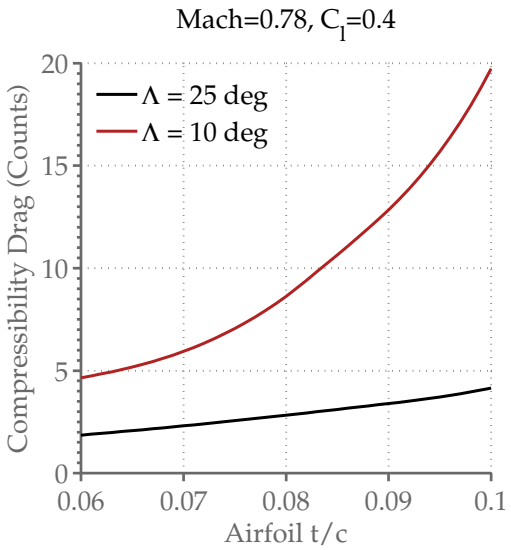

Figure 1.4. An illustration of typical compressibility drag rise trend as a function of streamwise t/c and wing sweep.

One could certainly reduce the sweep to render wings more compatible with NLF. However, unsweeping the wing at transonic speed carries steep penalties.[14–16] A typical plot of transonic drag rise as a function of sweep and thickness in fig. 1.4 shows that an unswept wing has to be made much thinner than its swept counterpart to prevent drag divergence. The structural consequences of reducing wing sweep and thickness

can be illustrated with the simple wing weight relationship of Cleveland:[17]

$$W_{wing_s} \propto \int \frac{M_x}{t} dy \propto \frac{b^3}{(t/c)\cos\Lambda^2 S_{ref}}$$

The equation shows that although unsweeping the wing may have a small, positive effect on structural efficiency, the effect of the $\cos^2(\Lambda)$ term is easily overshadowed by the linear weight increase with reduced t/c. A thin, unswept NLF wing can therefore weigh substantially more than its turbulent counterpart. And the weight penalties can wipe out the drag savings.

One way to cope with the aerostructural consequences of unsweep is to simply slow down. Indeed, most NLF design concepts are designed to cruise at Mach 0.70 to 0.75. The Sugar Volt for example is designed to cruise at Mach 0.71. However, in the absence of variable cycle technology, reduced cruise speed can negatively impact engine efficiency. And at today's fuel prices, slowing down can incur utilization and cost penalties. Moreover, air traffic control (ATC) could also be complicated by the presence of slower aircraft.

The alternative to slowing down is to reduce the weight penalties from a thin wing. Active load alleviation is one such technology that can tilt the balance of the Mach-sweep-thickness ($M\Lambda T$) trade in favor of low-sweep NLF wings.

1.3 Maneuver Load Alleviation

Maneuver load alleviation systems respond to pseudo-static maneuvers commanded by the pilot. Figure 1.5 shows two aircraft undergoing symmetric maneuver at the same load factor. The difference is that the MLA-equipped aircraft can use coordinated control deflections to concentrate lift inboard and reduce the wing bending moment. This allows the wing of the MLA-equipped aircraft to be made lighter, or longer and thinner at the same weight.

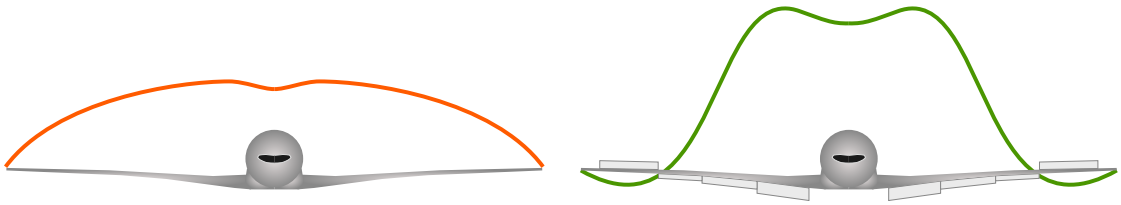

(a) Conventional **(b)** MLA

Figure 1.5. Lift distribution for conventional and MLA aircraft at the same maneuver load factor.

MLA has been the subject of numerous studies. Results suggest that MLA can achieve span increases of 10-15% and drag savings of 8-13% at fixed wing weight.[3,18–21] Experimental MLA systems have been flight tested under the NASA Mission Adaptive Wing (MAW) and Active Flexible Wing (AFW) programs. And production MLA systems have been integrated into commercial aircraft like the Airbus A320, A330.[22,23] However, the full benefit from load control can only be realized by incorporating the technology early on in the design process. The goal of the present research is to formally incorporate MLA into conceptual design.

1.4 Gust Load Alleviation

As MLA relaxes the structural design constraints imposed by maneuver loads, dynamic gust loads can becomes critical design conditions.[24] The implications are twofold: 1) gust loads should be considered when evaluating the effectiveness of MLA systems and 2) a gust load alleviation system is likely needed to realize the full benefits of MLA.

GLA responds to dynamic, unanticipated atmospheric turbulence. Unlike the MLA system, effectiveness of GLA systems may be fundamentally constrained by sensor and actuator bandwidths. The close interdependence between aircraft configuration and gust response complicates the process of GLA control law design. Previous studies have sought to address components of the integrated GLA design problem: 1) how to

find the worst-case gust for a given airplane,[25–29] 2) how to design aircraft structure to sustain a given gust[30–33] and 3) how to design a GLA control systems for a given airplane.[34–36] The more recent work of Fidkowski et al.[37] surveys stochastic gust design criteria and assesses the sensitivities of gust load to modeling assumptions. The present work extends these previous research and address the integrated problem of how to *simultaneously* design an aircraft with its GLA control system.

1.5 Organization

In chapter 2 we introduce the design framework, which extends our previous work on MLA and gust load alleviation.[38] In chapters 3 and 4 we develop new aerodynamic and structure analysis tools to incorporate laminar flow and active load alleviation into conceptual design. Next, the aeroservoelastic design framework is applied to a series of design studies in chapter 5. This is followed by a discussion of the results in chapter 6. Finally, we examine the performance sensitivities of the optimized aircraft to changes in critical design assumptions in chapter 7.

Chapter 2

Design Framework

The aeroservoelastic design framework developed in this thesis is based on the Program for Aircraft Synthesis Studies (PASS).[39] PASS in its basic form leverages fast, semi-empirical models to capture aircraft performance sensitivities to configuration and mission variables. In this chapter we introduce the components of the PASS mission analysis framework that are most relevant to load alleviation and NLF design. A more detailed discussion of the basic PASS framework can be found in Kroo.[39]

2.1 Aircraft Parameterization

The design framework is geared toward the analysis of "conventional" aircraft configurations characterized discrete fuselage, empennage and wing components. The wing parameterization and design are detailed in the next chapter.

The aircraft fuselage dimensions are dictated by the seating arrangement and passenger count, which are fixed for a given optimization. The horizontal tail is parameterized by its area ratio relative to the wing S_h/S_{ref}. The longitudinal position of the wing root x_{root} is an important parameter for trim, stability and landing gear integration.

The set of aircraft optimization variables can be summarized as:

$$\boldsymbol{x_{aircraft}} = \left[\frac{S_h}{S_{ref}}, x_{root}, W_{MTOW}, W_{MZFW}, T_0, x_{mg}\right]$$

The engine weight and dimensions are sized by the sea level static thrust variable T_0. The thrust and fuel consumption at a given flight condition are computed using a rubberized PW-2037 engine deck.[39] The sea-level static thrust-to-weight ratio and fuel consumption (TSFC) are scaled to match the more modern CFM-56-7B27 turbofan used on the comparable Boeing 737-800. The characteristics of the reference PW-2037 engine and the CFM-56-7B27 used in the engine scaling are summarized in table 2.1.

Engine	TSFC_0 (lb/lb-hr)	W_e (lb)	T_0 (lb)
PW-2037	0.326	7,160	34,250
CFM-56-7B27	0.380	5,216	24,000

Table 2.1. Engine parameters for the PW-2037 (reference engine deck) and CFM-56-7B27 turbofans.

A number of aircraft parameters are included as design variables to eliminate internal iterations. For example, the values of the maximum takeoff and zero fuel weights W_{MOTW} and W_{MZFW} are both needed *before* they can be evaluated in the analysis. Rather than relying on iterations to converge the weights, we simply include W_{MOTW} and W_{MZFW} as design variables and use compatibility constraints to enforce convergence. Similarly, the longitudinal placement of the landing gear x_{mg} is a function of the aircraft center-of-gravity (CG), which is itself dependent on the landing gear position. The aircraft-level compatibility constraints can be summarized as follows:

$$\left.\begin{aligned} x_{mg} &= \frac{\max\left(\boldsymbol{x_{CG}}\right) - 0.08 x_{ng}}{0.92} \\ W_{MTOW} &= W_{MZWF} + W_{fuel} + W_{res} \end{aligned}\right\} \quad \text{Aircraft Compatibility Constraints}$$

The weight constraint ensures that the sum of the empty weight, fuel weight and fuel reserves W_{res} adds up to the takeoff weight. The landing gear compatibility constraint

ensures that the nose carries at least 8% of the aircraft weight for traction.

2.2 Mission Analysis

We evaluate aircraft performance in the context of the representative short-haul mission profile illustrated in fig. 2.1. The mission includes takeoff, climb, cruise and approach segments. Not shown is a standard diversion reserve. The mission also includes *representative* gust encounters and limit maneuvers that combine to size the wing structure. The choice of the maneuver and gust flight conditions are detailed in chapter 4. The important mission parameters such as the initial and final cruise altitudes and the takeoff and landing Mach numbers and flap schedules are optimized concurrently with the aircraft:

$$\boldsymbol{x_{mission}} = [z_i, z_f, M_{to}, M_{land}, \delta_{to}, \delta_{land}]$$

The aircraft is designed to meet the range, field length, engine-out climb gradient and cruise thrust margin constraints summarized in eq. (2.1). The field performance requirements are based on published payload-range diagrams for the Boeing 737-800. The climb gradient constraint follows from the Federal Aviation Regulations (FAR). The cruise stage drag-to-thrust constraints ensure that the aircraft has sufficient thrust at altitude to sustain operational climb.

$$\left.\begin{array}{c} l_{to} < 7{,}900\text{ft},\ l_{land} < 5{,}500\text{ft},\ h_c > 0.024 \\ \dfrac{D}{T}_i < 0.88,\ \dfrac{D}{T}_f < 0.88,\ R > 2{,}000\text{nm} \end{array}\right\} \quad \text{Performance Constraints} \tag{2.1}$$

The computation of the climb gradient, cruise stage drag-to-thrust ratios and cruise range require the aircraft drag and thrust at different flight conditions. The available thrust comes from the rubberized engine deck discussed in section 2.1.[39] We compute

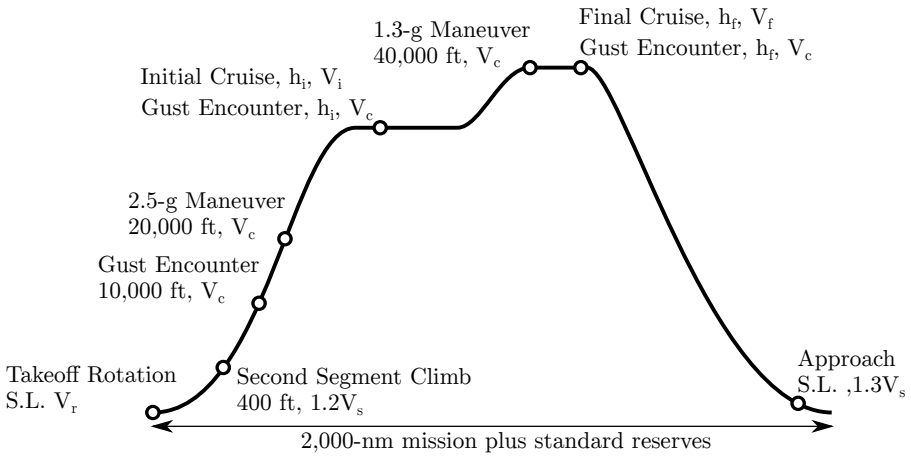

Figure 2.1. The design mission profile and flight conditions.

the fuselage and empennage parasite drag using equivalent plate area methods and empirical shape factors.[39] We assume that the wave drag of the fuselage and tail are negligible compared to the wing. The more wing drag build-up is discussed in detail in chapter 3.

To approximate the effects of step-climbs we assume a *linear* variation in aircraft weight, drag and $TSFC$ from an initial to a final cruise state.The aircraft range R can then be integrated as follows:

$$R = RF_i - RF_f + \left(RF_f - W_f \frac{RF_f - RF_i}{W_f - W_i} \right) \ln \left(\frac{W_i}{W_f} \right) \tag{2.2}$$

The aerodynamic and propulsion contributions to range are captured in the range factor:

$$RF = \frac{v}{TSFC} \left(\frac{L}{D} \right)$$

The aircraft is subject to trim, stability and maximum lift constraints at *each* of the flight conditions in fig. 2.1. The trim constraints consists of lift matching and tail maximum lift components:

$$\left. C_{Lh} < C_{Lhmax},\ nW = \frac{\rho v^2 S_{ref} C_L}{2} \right\} \quad \text{Trim Constraints}$$

A conservative static stability margin of 10% is imposed at all flight conditions to account for aeroelastic washout in cruise, which tends to move the aerodynamic center forward and thereby diminish the stability margin:

$$-\frac{dC_{Mac}}{dC_L} > 0.10\overline{c}\Bigg\} \quad \text{Stability Constraints}$$

In addition to the flight conditions outlined in the mission profile we also include a stability constraint for cruise at operational empty weight (OEW). For conventional configurations the empty aircraft typically has the aft-most center of gravity and is critical in stability. The lift-matching constraint enforces force balance in each equilibrium flight condition. The tail maximum lift coefficient prevents tail stall.

The wing C_L and the horizontal tail C_{Lh} needed to trim the aircraft are solved from the force and moment balance:

$$C_{mac} - \frac{C_{Lw}}{\overline{c}}(x_{acw} - x_{cg}) - \frac{C_{Lh}}{\overline{c}}(x_{ach} - x_{cg})\frac{S_h}{S_w} = 0$$

$$C_L = C_{Lw} + C_{Lh}\frac{S_h}{S_w}$$

The wing aerodynamic center x_{ac} and stability derivatives such as the pitch moment coefficient C_{mac} are evaluated using the Weissinger panel method. The pitch moment includes contributions from wing twist, control surface deflections and the zero-lift airfoil pitch moment, which is integrated from the inverse airfoil design discussed in more detail in section 3.5.1. Also included are the aeroelastic wing twist induced by control surface deflection.

Chapter 3

Wing Design

The multitude of new design sensitivities and constraints introduced by load alleviation and NLF call for physics-based wing design tools. The analysis is grounded on a detailed parameterization of the wing and structure box. A Weissinger panel method with compressibility corrections is used to solve the aerodynamic loads and stability derivatives. Finally, we develop a hybrid-inverse viscous design tool to incorporate NLF into aircraft design.

3.1 Geometry

The wing parametrization begins with the definition of the trapezoidal planform. The reference area S_{ref}, aspect ratio AR, taper ratio λ and quarter-chord sweep $\Lambda_{1/4}$ are all design variables. The vector of wing jig twists $\boldsymbol{\theta}$ at the exposed breakpoints are also subject to optimization. The trapezoidal wing is modified by trailing edge extensions defined at wing breakpoints. The extensions $\boldsymbol{\Delta c}$ are defined as fractions of the trapezoidal chord. All intermediate planform geometries and twists are linearly interpolated.

While the design framework can accommodate an arbitrary number of wing breaks, we

choose the six sections highlighted in fig. 3.1 to define the planform. The breakpoint positions as fractions of the semispan are held constant in the optimization.

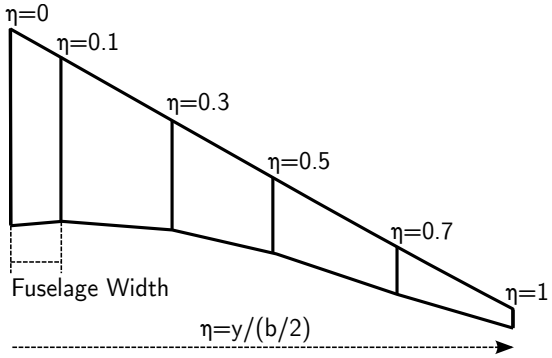

Figure 3.1. The wing break sections that define the planform and twist. The innermost section ($\eta = 0$) corresponds to the wing root. The next section defines the wing-fuselage intersection.

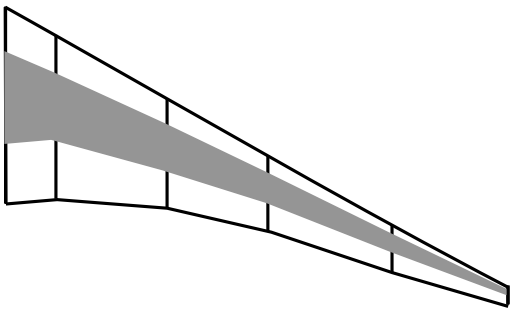

Figure 3.2. The wing structure box configuration.

The wing structural box in fig. 3.2 extends from 20 to 65% of the chord. The hexagonal wing box geometry is defined by the elastic axis and forward and aft spar heights at each breakpoint section. The skin and web thicknesses t_s and t_w at the breakpoints are also optimization variables. The intermediate wing box geometries are again interpolated. The wing load-bearing weight follows directly from the wing box geometry and material density. However, the weight of the spars and webs represents only a portion of the total wing weight. We establish the relationship between wing load-bearing and total weight using the empirical fit developed by Gallman,[40] which accounts for minimum gauge effects and non-structural weight. The wing geometry

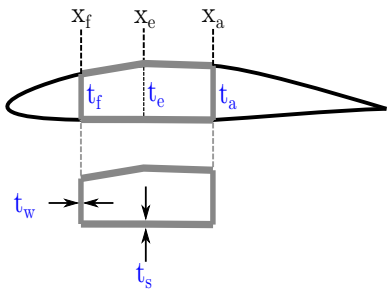

Figure 3.3. The parameterization of the wing box cross section.

design variables $\boldsymbol{x_{wing}}$ can be summarized as follows:

$$\boldsymbol{x_{wing}} = \left[S_{ref}, AR, \lambda, \Lambda_{1/4}, \boldsymbol{\Delta c}, \boldsymbol{\theta}, \boldsymbol{t(x_e)}, \boldsymbol{t(x_f)}, \boldsymbol{t(x_a)}, \boldsymbol{t_s}, \boldsymbol{t_w}\right]$$

The wingbox geometry is fully defined by the optimization variables. The winbox is sized by the spanwise static and dynamic stress constraints in the optimization. The resolution of the aerodynamic loads are discussed in detail in chapter 4.

3.2 Aerodynamics

We compute the wing lift distribution and stability derivatives using a modified Weissinger method, which is a vortex lattice method (VLM) with only one chord-wise panel.[41] Each semispan is modeled using 31 skewed bound vortices centered along the quarter chord line. The flow tangency boundary conditions are enforced at control points along the three-quarter-chord line. The control point arrangement is illustrated in fig. 3.4.

The linear system for the vortex strengths Γ_i can be written in terms of the aerodynamic influence coefficient matrix and the local angle of attack α_i:

$$[AIC]\,\Gamma_i = U_\infty \alpha_i$$

Where element AIC_{ij} relates the induced downwash at control point i to the vortex

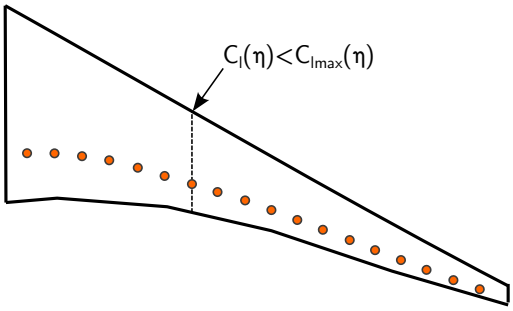

Figure 3.4. An illustration of wing aerodynamic control points and $C_{l_{max}}$ constraints.

strength at station j. The incompressible AIC matrix is strictly a function of the wing geometry. At high subsonic and transonic speeds we apply the 3-D Prandtl-Glauert corrections to give a preliminary account of compressibility effects. The longitudinal distances between each control points i and bound vortex j are sheared by the inverse of the Prandtl-Glauert factor β. This makes AIC both a function of the wing geometry and the flight Mach number.

$$\beta = \sqrt{1 - {M_\infty}^2}$$

The induced drag is solved from the Trefftz plane integration of the farfield normalwash. The total induced drag of the wing-tail systems follows from the application of Munk's biplane analogy.[39]

Both MLA and GLA rely on control deflections to alter the spanwise load. The aerodynamic effects of control deflections must be modeled in a physical way. To this end we represent the control surface deflections in the Weissinger method using equivalent wing twists. The control surface deflections are modeled as changes in the local zero-lift angle of attack α_0 that produce the same changes in section C_l.[42] This approximation allows us to study the effects of flap and aileron deflection on the 3-D lift distribution using the Weissinger method.

3.3 High Lift

The wing high lift performance not only helps to determine field performance but also influences the effectiveness of the MLA system.

The configuration of the high-lift system represents an important multidisciplinary trade. Active load alleviation systems favor high-bandwidth control surfaces that sacrifice outright lift capacity for speed and simplicity. Field-length stands however to benefit from more complex and heavy multi-slotted flaps. A more highly loaded wing – enabled by powerful high lift systems – is also more efficient in cruise. In subsequent studies the wing is configured with simple, single-slotted flaps to better support variable camber control.

Full span slats are active in takeoff and landing segments. The slats represents Kreuger flaps that retracts flush to the lower wing surface. The slat gaps can disrupt laminar flow on the bottom surface. We address the NLF implications of slat integration in more detail in chapter 5.

We appeal to the method of critical sections to estimate wing maximum lift: the wing is deemed lift-critical if any of its sections reach the local $C_{l_{max}}$.[43] Figure 3.4 shows that the η-position of the lift constraints n eq. (3.1) are collocated with the aerodynamic control points. The maximum lift constraints are imposed for all trimmed flight conditions. A lift coefficient margin of 0.2 is applied to stations outboard of the 75% semispan to guarantee aileron control authority.

$$C_l(\eta) < \begin{Bmatrix} C_{l_{max}}(\eta) & \text{if } \eta < 0.75 \\ C_{l_{max}}(\eta) - 0.2 & \text{otherwise} \end{Bmatrix} \quad \text{Wing Maximum Lift Constraints} \quad (3.1)$$

We model the section $C_{l_{max}}$ as functions of the section airfoil parameters, the wing sweep and the control surface deflections:[43]

$$C_{l_{max}}(\eta) = f\left(t/c, Re_c, M_\infty, \Lambda_{1/4}, \delta, \delta_s\right)$$

The effect of thickness is modeled using flight test data. Increased t/c moderates the severity of the leading edge suction peak, increases the robustness of the boundary layer against flow separation and increases maximum lift. The thickness effects on the maximum lift are disabled in takeoff and landing conditions when the slats are active. The effects of Reynolds number, Mach number and wing sweep on maximum lift are modeled using flight test data from the DC-10.[43]

We plot the variations in C_{lmax} as functions of the Mach number, wing sweep and flap deflection in figs. 3.5 and 3.7. The abscissa for each plot is the section t/c.

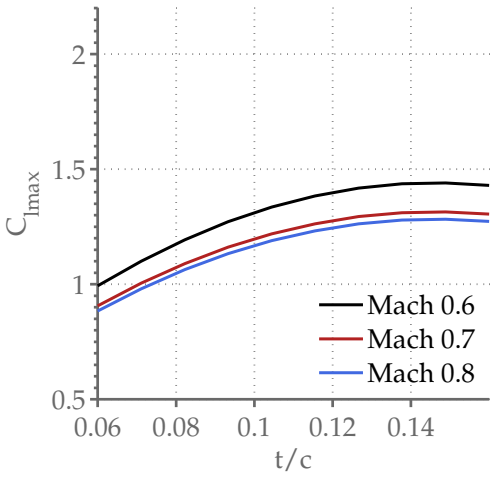

Figure 3.5. Section C_{lmax} as a function of t/c and Mach number. The airfoil is in its clean configuration and the chord Reynolds number is fixed at 20 million.

Figure 3.5 shows that the model captures the non-linear decrease in maximum lift at higher Mach numbers. The effect of Mach number is important when we consider the lift capacity of the wing in high-speed maneuvers to qualify the effectiveness of the MLA system. fig. 3.6 shows that the lift model captures the small but positive effect of reduced wing sweep on maximum lift. In low-sweep NLF wings we might expect the reduced sweep to offset in a small way the loss in maximum lift from the necessarily reduced wing t/c. Finally, fig. 3.7 shows that flap deflections has a significant impact on section maximum lift.

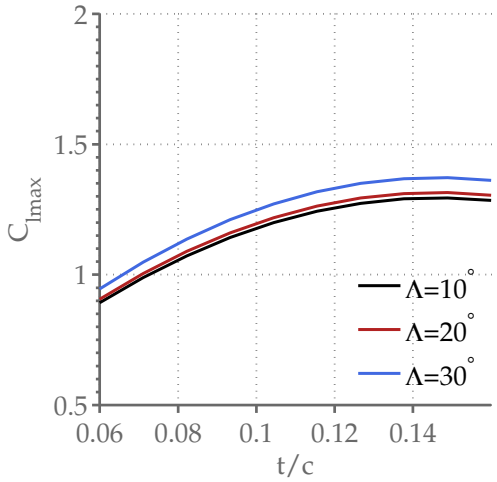

Figure 3.6. Section $C_{l_{max}}$ as a function of t/c and wing sweep in degrees. The airfoil is in its clean configuration and the chord Reynolds number is fixed at 20 million.

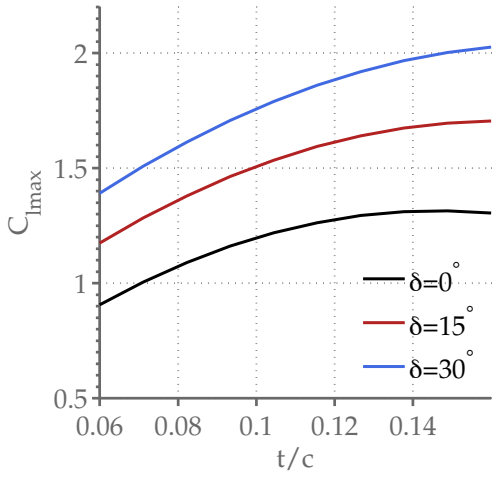

Figure 3.7. Section $C_{l_{max}}$ as a function of the t/c and flap deflection in degrees. The Reynolds number is fixed at 20 million.

The coupling between load alleviation and high lift means that changes in the optimum wing sweep, planform and thickness from the application of load alleviation also alter the high lift performance.

3.4 Structure

The wing structure is sized by cruise, maneuver and gust loads. We make the simplifying assumption that the bending loads are carried by spars and shear and torsional loads by webs. The wing is sized by the static stress constraints in eq. (3.2). The wing stresses are functions of the aerodynamic load and the wingbox geometry. Figure 3.8 shows that the y-position of the stress constraints are once again collocated with the aerodynamic control points.

$$\left.\{\sigma(\eta)\} < \sigma_a,\ \{\tau(\eta)\} < \tau_a\right\} \quad \text{Static Structure Constraints} \tag{3.2}$$

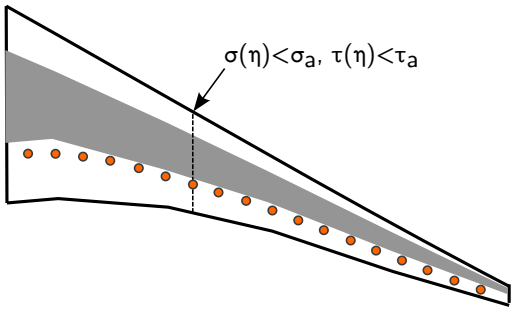

Figure 3.8. Wing static stress constraints.

As active load alleviation systems reduce the stresses in the wing, stiffness requirements become more import. The thin, high-aspect ratio wings enabled by load alleviation are prone to flutter and aileron reversal. It is necessary to impose an aileron reversal constraint at the maximum structural cruise speed V_c:

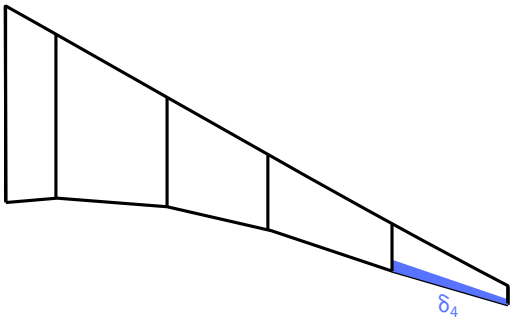

Figure 3.9. The aileron reversal constraint placed on the outboard deflections δ_4.

The reversal constraint is imposed on the outermost trailing edge control surface identified in Figure 3.9. We require the aileron roll moment of the flexible wing $L_{e\delta_4}$ to be at least 53% of its rigid counterpart ${L_{r\delta_4}}^{44}$ at V_c:

$$\left.\frac{L_{e\delta_4}}{L_{r\delta_4}}\right|_{V_c} > 0.525$$

The required aileron efficiency of 53% at V_c is rather conservative. The aileron reversal limit is an operational parameter and should be investigated in more detail. The rigid wing roll moment due to a unit aileron deflection can be readily solved using the Weissinger method. To obtain the elastic wing roll moment we add the aeroelastic twist θ_e to the panel method boundary conditions. The aileron-induced twist about the elastic axis can be integrated as follows:

$$\tilde{\tau}_{\delta_4} = q \int_{\tilde{y}}^{b/2} \cos^3 \Lambda_e c(\xi)^2 C_{m\delta_4}(\xi) d\xi$$
$$\tilde{\theta}_e = \int_0^{\tilde{y}} \frac{\tilde{\tau}_{\delta_4}(\xi)}{GJ(\xi)} d\xi$$

We transform the twist into the spanwise direction to obtain the modifications to the aerodynamic boundary conditions.

3.5 Inverse Design

The extent of attainable wing natural laminar flow is a strong function of the pressure distribution. We develop a hybrid-inverse viscous design tool to link flow transition and profile drag to the wing geometry and lift distribution. In the inverse approach, we first define the pressure distribution and then solve for the corresponding geometry. The pressure distribution and geometry are then combined with integral methods to solve for the boundary layer development, transition location and ultimately, the profile drag. The method is inspired by the work of Liebeck.[45] It can also be understood as a smooth, 2-D analogue of the more involved 3-D viscous design system of Allison el. al.[13]

3.5.1 Pressure Distribution

The pressure variables define the compressible streamwise C_p distributions at the exposed wing stations highlighted in fig. 3.10. The wing-fuselage intersection highlighted in red is always assumed to be turbulent to reflect the dominant effects of attachment line instabilities at the intersection.

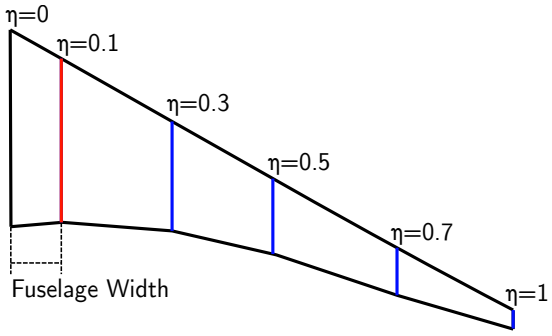

Figure 3.10. The wing breakpoints with inverse design sections highlighted. The blue sections can be designed for NLF while the red wing-fuselage intersection is always assumed to be turbulent to account for the dominant role of attachment line instabilities.

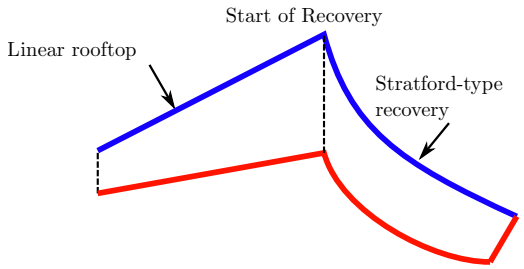

Figure 3.11. An illustration of the airfoil C_p parameterization with important pressure features labeled.

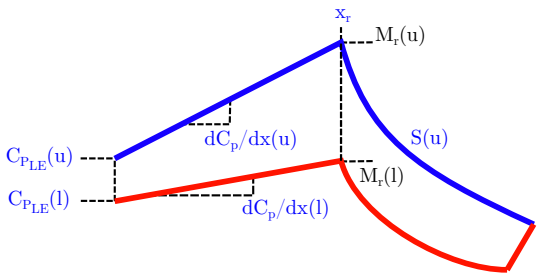

Figure 3.12. The inverse deisgn C_p parametrization with the pressure variables labeled in blue.

The motivation for an inverse approach stems chiefly from the commonality of NLF airfoil pressure distributions. Figure 3.11 illustrates the features of a representative NLF pressure distribution: 1) an extended region of accelerating, 2) a short transition ramp, 3) a weak shock and 4) a rapid recovery to the trailing edge. The pressure features can be even more succinctly described using the parameterization illustrated in fig. 3.12. Here the C_p distribution is parameterized by a linear ramp followed by a Stratford-type recovery.[46] The pressure variables are defined in eq. (3.3).

$$\boldsymbol{x_{pressure}} = \left[\boldsymbol{x_r}, \boldsymbol{C_{pLEl}}, \boldsymbol{C_{pLEu}}, \left(\frac{\boldsymbol{dC_p}}{\boldsymbol{dx}}\right)_{\boldsymbol{u}}, \left(\frac{\boldsymbol{dC_p}}{\boldsymbol{dx}}\right)_{\boldsymbol{l}}, \boldsymbol{S_u}\right] \tag{3.3}$$

The most important variable for laminar flow is the rooftop pressure gradient $\frac{dC_p}{dx}$ – a "favorable" pressure gradient can stabilize the streamwise boundary layer. The start of recovery x_r determines both the extent of the rooftop and the balance of aft loading. In the present analysis the value of x_r controls the start of recovery on both the upper and lower airfoil surfaces. This is done to reduce discretization and numerical integration errors.

The Stratford criteria in section 3.5.1 defines a rapid recovery that is everywhere on the verge of separation. By minimizing the recovery distance the Stratford recovery can maximize the length of the laminar rooftop. An added computational benefit of the Stratford recovery is its simplicity: the shape of the recovery can be defined using only the flow conditions at x_r and the concavity parameter S:

$$S = \frac{\overline{C_p}\sqrt{x\frac{d\overline{C_p}}{dx}}}{\left(10^{-6}\overline{Re}_x\right)^{0.1}}$$

Here the canonical pressure coefficient $\overline{C_p}$ and effective Reynolds number $\overline{Re}_x$ are defined in terms of the flow properties at the start of recovery:

$$\overline{Re}_x = \frac{xu_r}{\nu}$$
$$\overline{C_p} = 1 - \left(\frac{u}{u_r}\right)^2$$

The classical Stratford criteria is formulated with a concave recovery at $S = 0.39$. However, a flow that is everywhere on the edge of separation cannot be used for practical design. We derive therefore the solution to the Stratford criteria for an arbitrary S in section 3.5.1 and use a more conservative S of 0.35 to define the recovery.

$$\overline{C_p} = \begin{cases} \left[{\overline{C_p}_m}^3 + 0.1893 {\overline{Re}_x}^{1/5} \ln\left(\frac{x}{x_m}\right) S^2 \right]^{1/3} & \overline{C_p} < 4/7 \\ 1 - \frac{k_a}{\sqrt{k_b + \frac{x}{x_m}}} & \overline{C_p} \geq 4/7 \end{cases}$$

Here the free parameters k_a and k_b are solved numerically to match the canonical pressure $\overline{C_p}$ and its derivative at the inflection point where $\overline{C_p}$ exceeds 4/7.

Pressure Constraints

The pressure distribution generated using the current parameterization scheme are not guaranteed to be realistic. We use constraints to ensure that the design pressure distributions are consistent with the spanwise lift distribution and produce acceptable high-speed performance:

$$\left.\begin{aligned} \int_0^c \left[C_{p_l}(x) - C_{p_u}(x) \right] dx > C_l(\eta) \\ M_{ru\perp} < 1.1,\ M_{rl\perp} < 0.95 \end{aligned}\right\} \quad \text{Pressure Constraints} \tag{3.4}$$

The section lift coefficient integrated from the chord-wise pressure distribution must match the spanwise C_l from the Weissinger solution. We specify the lift-matching constraint as an inequality because the optimized pressure distribution should always reach the C_l upper bound.

A useful design heuristic for supercritical airfoils is to limit the pre-shock Mach number on the suction side $M_{ru\perp}$ to less than 1.1. Stronger shocks may lead to drag divergence and flow separation. We apply the sweep-taper transformation of Lock[47] to obtain $M_{ru\perp}$ from the design pressure distribution.

For a given C_l and thickness the pressure gradient is restricted only by the pre-shock

Mach number. The inverse design method captures therefore a fundamental trade-off between high speed performance and natural laminar flow. The restriction on the shock Mach number is conservative. Indeed, a recent study by Jameson, Vassberg and Shankaran[48] suggests that low sweep transonic wings may be attainable with modern CFD design tools. This would a significant effect on the extent of realizable laminar flow. Sensitivity studies show that even an increase from a limit pre-shock Mach number of 1.1 to 1.15 can lead to significant increases in the laminar run.

The compressibility drag is estimated using an assumed quartic drag rise profile. We assume 15 counts of compressibility drag for a top wing surface shock Mach number of 1.1. This is in line with the performance of well-designed supercritical sections. A single-parameter empirical model of C_{dc} is admittedly quite limited. However, by restricting the maximum recovery Mach number above and below the airfoil we ensure that the airfoil designs are reasonable. And by making the compressibility drag sensitive to the peak Mach number, we link the compressibility drag evaluation to NLF and structural design: the optimizer can trade C_{dc} against C_{dp} and structural efficiency. The compressibility drag is referenced to the sweep of the x-position of the start of pressure recovery (x_r) to better match the isobar ahead of the moderate shock. Implicit is the assumption that the compressible aerodynamics of the section is better related to the wing sweep incident of the shock.

$$C_{dc_\perp} \propto M_{x_r \perp}$$
$$C_{dc} = C_{dc_\perp} \cos^3(\Lambda_{x_r})$$

3.5.2 Airfoil Geometry

We use thin airfoil theory to map a defined pressure distribution to its associated airfoil geometry. Classical thin airfoil theory holds for incompressible flow. It is necessary then to apply both the sweep-taper and inverse Kármán-Tsien transformations to convert the compressible streamwise C_p to the equivelent incompressible pressure distribution $\tilde{C}_p$ normal to the local isobars. We map the incompressible pressure

distribution to airfoil thickness $t(x)$ and camber $z(x)$ distributions using the following integral equations:

$$\frac{\tilde{u}_u(x) + \tilde{u}_l(x)}{2} = \frac{1}{\pi}\int_0^c \frac{dt(\xi)}{d\xi}\frac{d\xi}{x-\xi}$$
$$\alpha - \frac{dz}{dx} = \frac{1}{4\pi}\int_0^c \frac{\left[\tilde{C}_{p_l}(\xi) - \tilde{C}_{p_u}(\xi)\right]d\xi}{\xi - x}$$

The induced velocity at the chord line are specified by the pressure distribution:

$$\tilde{u}(x) = \sqrt{1 - \tilde{C}_p(x)}$$

We discretize the airfoil and solve the integral equations using a panel method. Thickness constraints defined in the chordwise direction ensure that the inverse airfoil geometry can accommodate the previously defined wing box:

$$\left.\begin{array}{l} t_{inv}(x_e) > t_e,\ t_{inv}(x_f) > t_f \\ t_{inv}(x_a) > t_a,\ t_{inv}(x_{te}) = 0 \end{array}\right\} \quad \text{Wing Box Compatibility Constraints}$$

The inverse thicknesses solution at the forward spar, elastic axis and aft spar must match the wingbox geometry defined in $\boldsymbol{x_{wing}}$. The trailing edge thickness is constrained to close the airfoil. An example of optimized wing section C_p distributions and their corresponding geometries can be found in figs. 3.13 and 3.14. The first section at $\eta = 0.1$ corresponds to the wing root. The root section is forced to be turbulent to reflect the impact of attachment line boundary layer instabilities. The optimizer sees little incentive to design a favorable pressure gradient in that case. The outboard sections are designed for NLF and all show various degrees of favorable pressure gradient.

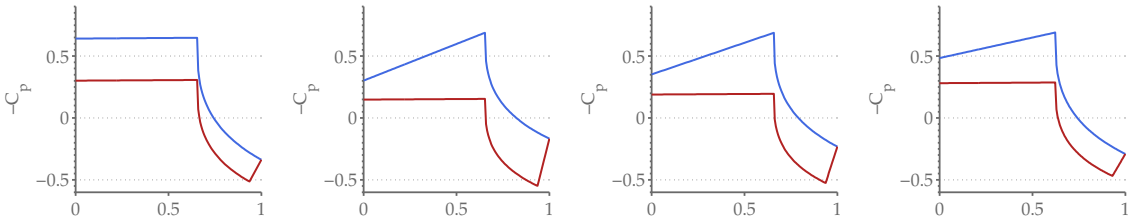

(a) $\eta = 0.1$ **(b)** $\eta = 0.3$ **(c)** $\eta = 0.5$ **(d)** $\eta = 0.7$

Figure 3.13. Example wing section pressure distributions at selected spanwise locations.

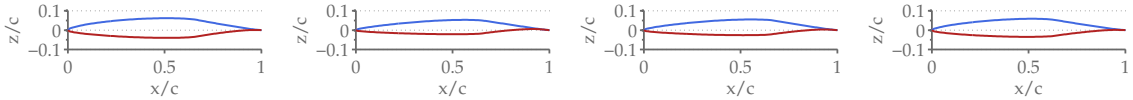

(a) $\eta = 0.1$ **(b)** $\eta = 0.3$ **(c)** $\eta = 0.5$ **(d)** $\eta = 0.7$

Figure 3.14. Example wing section geometry at selected spanwise locations.

3.5.3 Boundary Layer Solution

We employ the integral methods of Thwaites and Head to solve the laminar and turbulent boundary layers.[49] Compressible boundary layer solutions can certainly increase accuracy. However, since compressibility tends to stabilize the streamwise boundary layer,[14,50,51] an incompressible analysis is at least conservative. We do however, apply compressibility corrections to the turbulent surface friction coefficient C_f.[14]

Laminar Boundary Layer

The Thwaites solution for the laminar momentum thickness θ is given by equation section 3.5.3. The equation can be exactly integrated if the pressure distribution is analytic with respect to the surface coordinate s. However, the laminar ramp in the

present analysis is only linear in x; a numerical solution is still required.

$$\theta^2 = \frac{0.45\nu}{{u_e}^6} \int_0^s {u_e}^5 ds$$

Transition

To simulate turbulent sections we force flow transition near 3% chord. For NLF sections we allow the flow to transition freely.

Transition prediction remains an area of active research. An often used engineering transition criteria is the method of Michel.[49] Michel's method is simple to use but does not direct account for the effects of the pressure gradient. More importantly, the method is not smooth and therefore incompatible with gradient-based optimization.

The e^9 transition envelope fits of Drela and Giles[52] and those of Arnal, Habiballah and Delcourt[53] are smooth and are sensitive to the pressure gradient. However, these methods also require the numerical solution of both a point of critical stability and a point of transition. The two-point solution presents difficulties for surface discretization and numerical integration. To minimize numerical error we use the simpler, single-step $H - R_x$ transition criteria:[54]

$$\log[Re_{e^9}] = -40.4557 + 64.8066H - 26.7538H^2 + 3.3819H^3$$

The $H - R_x$ criteria defines the transition Reynolds number at all points on the airfoil as a function of the local shape factor of the boundary layer. Re_{e^9} is the local Reynolds number Re_x where the fits to the e^9 envelope predict flow transition. Transition occurs when the local Reynolds number exceeds the local transition Reynolds number:

$$Re_x(x) > Re_{e^9}(x)$$

At this point one could use interpolation on iterative solvers to solve the $H - R_x$ criteria. However, while an interpolation scheme may be sufficiently accurate for purposes of boundary layer analysis, it is not accurate enough for gradient-based optimization. The numerical problems becomes intractable at high Reynolds numbers where the transition location x_t is sensitive to even small changes in the pressure gradient. One way around this numerical problem is specify x_t as an optimization variable:

$$\boldsymbol{x_{transition} = x_t}$$

Of course the optimizer cannot be allowed to freely pick a transition point. That would be too easy. It is necessary to further apply a compatibility constraint to enforce laminar flow *before* x_t:

$$Re_x(x_t) < Re_{e^9}(x_t)$$

The application of optimizer-based decomposition leverages the non-linear solver already present in the optimizer to converge the transition location. This eliminates the costly internal iterations that would otherwise be needed to solve the transition problem. The decomposition also reduces the laminar boundary layer evaluation to just one point at x_t.

Turbulent Boundary Layer

We solve the turbulent boundary layer using the Heads method. The boundary layer solution is advanced to the trailing edge using the fourth-order Runge-Kutta scheme. The section profile drag of each surface is solved using the Squire-Young momentum equation:

$$C_{d_p} = 2\frac{\theta_{te}}{c}\left(\frac{u_{te}}{u_\infty}\right)^{\frac{H_{te}+5}{2}}$$

The total wing profile drag in cruise is integrated from the C_{d_p} solutions at the break sections.

Chapter 4

Active Load Alleviation

An important goal of this thesis is to find a way to develop the aircraft load control system concurrently with the configuration. The design framework includes therefore detailed parameterization of the MLA control schedule and the GLA control law. The dynamic loads in gust encounters are resolved using a combination of aircraft dynamics simulations and modal solutions of the wing structural response. The individual components of the structural dynamics solver are validated against standard beam test cases.

4.1 MLA and GLA Parameterization

Active load alleviation systems use coordinated control surface deflections to minimize wing stress. In principle any combination of control surfaces can be utilized. For simplicity we restrict the MLA and GLA control surfaces to the ailerons and flaps. This includes all of the trailing edge control surfaces in shown in fig. 4.1. The sensitivity of the aircraft design to control allocation is examined in more detail in chapter 7.

Figure 4.1 illustrates the trailing edge control surface arrangement and parameterization. Each exposed trailing edge section bounded by successive wing breakpoints

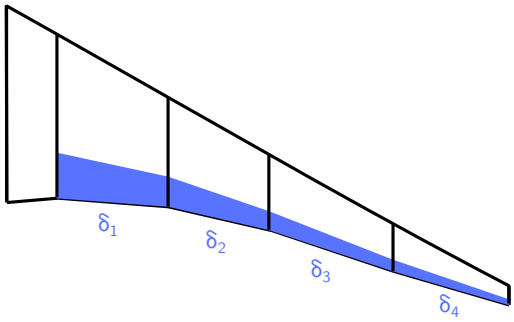

Figure 4.1. The wing control surfaces are defined by the wing break sections.

represents an independent control surface. The inboard sections simulate flap deflections; outboard sections simulate ailerons. Both the aileron and flap surfaces are assumed to extend over 25% of the chord. The chord ratio is somewhat lower than the typical extended chord of flaps. A conservative parameterization of the flap chord is however consistent with the need for lightweight, high-bandwidth control surfaces to achieve effective dynamic load alleviation. The control surface deflection schedules and dynamic gains are optimized with the aircraft.

4.2 Maneuver Load Alleviation

A first-order question in the design of the MLA system is the definition of the limit maneuvers. The aircraft should ideally be designed for the entire V–n envelope. An exhaustive search for the worst loads may not, however, be practical or indeed necessary for conceptual design. An alternative is to identify *representative* maneuvers that can efficiently capture the key aerostructural trade-offs and inform design.

The Federal Aviation Regulations (FAR) require commercial aircraft structures to be designed to withstand a 2.5-g maneuver at a structural safety factor of 1.5. For a conventional aircraft the speed and altitude of the limit maneuver flight condition are not particularly important – the stress is determined by the load factor. Defining representative maneuvers becomes more complicated for aircraft designed with MLA.

Here the wing stress state is fundamentally dependent on the effectiveness of load alleviation, which can in turn be dictated by aerodynamic constraints such as the wing maximum lift.

We design the aircraft for a 2.5-g symmetric pull-up at an altitude of 30,000 feet and the structural design velocity V_c. The maneuver altitude is justified by two observations. First, drastic maneuvers at altitudes higher than 30,000 feet are likely constrained by available engine thrust and maximum lift. The flight control system of commercial aircraft typically restrict the maneuver envelope at altitude to prevent stall.[22,23] Second, drastic maneuvers for obstacle avoidance and stall recovery are far more likely at lower altitudes. We also design the aircraft for a 1.3-g pull-up at 40,000 feet and the cruise velocity. The maximum-lift constraints help to ensure that the wing remains buffet-free in cruise-stage maneuvers at high altitude.

The MLA design variables are the vector of trailing edge control deflections $\boldsymbol{\delta}$ for each of the design maneuver conditions:

$$\boldsymbol{x_{MLA}} = \boldsymbol{\delta}$$

The range of trailing edge deflections are limited by hinge moment, control reversal and flow separation considerations. We impose a generous absolute MLA deflection limit of 10° on each of the control surface:

$$-10^\circ < \delta_i < 10^\circ$$

The deflection limit is consistent with the published parameters of the load alleviation systems on the Airbus A320, A330 and A340, which share a maximum control deflection of 11°.[22,23] The limit is further supported by experiments, which show that high-speed trailing edge deflections on the order of 8° can be sustained without significant flow separation.[18] And since limit maneuvers need not be performed at constant altitude, drag penalties from the control surface deflections do not meaningfully impact the design. The sensitivity of the optimized aircraft to the allowable range of control surface deflections is examined in more detail in chapter 7.

4.3 Gust Load Alleviation

The wing structure is also sized by time-dependent gust load constraints in eq. (4.1). The gust load constraints are imposed at the three different gust encounter flight conditions discussed in section 2.2: at 10,000 ft and the initial and final cruise altitudes. The y-positions of the gust-induced stress constraints are collocated with the aerodynamic control points.

$$\Big\{\sigma(\eta,t)\Big\} < \sigma_a,\ \Big\{\tau(\eta,t)\Big\} < \tau_a\Big\} \quad \text{Dynamic Stress Constraints} \tag{4.1}$$

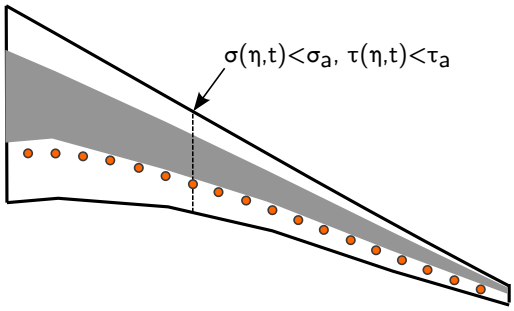

Figure 4.2. The wing static and dynamic stress design constraints are collocated with y-position of the aerodynamic control points.

Aircraft gust load experienced is a complex function of gust shape, aircraft dynamics and wing structural dynamics. Active load control introduce additional couplings among the aircraft configuration, GLA control law and gust shape. An important feature of the design framework is its integration of multi-point aircraft and wing structural dynamics simulations into the design optimization.

4.3.1 GLA Parameterization

The GLA system is driven by a proportional-derivative (PD) controller. The control inputs are the gust-induced apparent α and $\dot{\alpha}$. The outputs are the trailing edge

control surface deflection commands $\delta(t)$:

$$\boldsymbol{\delta(t)} = \boldsymbol{k_p}\alpha(t) + \boldsymbol{k_d}\dot{\alpha}(t)$$

The GLA design variables $\boldsymbol{x_{GLA}}$ includes the proportional and derivative gains for the control surface channels:

$$\boldsymbol{x_{GLA}} = [\boldsymbol{k_p}, \boldsymbol{k_d}]$$

The deflection commands are subject to actuator deflection and rate limits:

$$\begin{aligned} -10^\circ < \delta_i < 10^\circ \\ \frac{d\delta_i}{dt} < 25^\circ/s \end{aligned} \tag{4.2}$$

The GLA control surface deflection limits match those of the MLA system for consistency. The GLA actuator rates are conservative relative – typical commercial aircraft ailerons can deflect at 35-40°/s.[55] The parameterization treats the inboard control surfaces more like inboard ailerons than traditional, slow moving flaps. The impact of the trailing edge control surface rates are examined in more detail in chapter 7. Finally, while we assume exact knowledge of the control inputs in this initial study, measurement uncertainty and delay can be included in subsequent studies to improve the accuracy of the results.

4.3.2 Gust Load Design Criteria

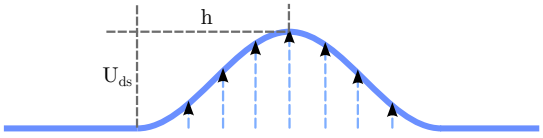

Figure 4.3. The 1–Cosine gust.

The Federal Aviation Regulations (FAR) specifies both a *continuous* and a *discrete* vertical gust criteria.[28,56] The former continuous criteria is important for fatigue analysis and passenger comfort. The latter discrete gust criterion – the focus of the

present thesis – is meant to characterize significant gust events that can size the wing. The FAR discrete gust criteria in eq. (4.3) requires the aircraft structure to withstand encounters with the so-called 1–Cosine gust illustrated in fig. 4.3.

$$w_g(t) = \pm\frac{U_{ds}}{2}\left[1 - cos\left(\frac{\pi V}{ht}\right)\right] \tag{4.3}$$

The gust amplitude U_{ds} is a function of the design reference velocity U_{ref}, the gust alleviation factor F_g and the gust gradient length h:

$$U_{ds} = U_{ref}F_g\left(\frac{h}{350}\right)^{1/6}$$

Where h is one half of the gust wavelength:

$$h = \frac{\lambda_g}{2} = [35, 350] \text{ ft}$$

The gust amplitude increases with $h^{1/6}$ in accordance with the theoretical scaling properties of severe atmospheric turbulence. The gust reduction factor is an empirical approximation of the alleviation effects of unsteady aerodynamics:

$$F_g = f(W_{MZFW}, W_{MTOW}, W_{MLW}, z_{max})$$

The reference gust design velocity U_{ref} in the 1–Cosine definition is a piecewise function of altitude:

$$U_{ref}|_{V_c} = \begin{cases} 56 - 12\left(\frac{z}{15{,}000}\right) \text{ ft/sec} & \text{for } 0 \leq z \leq 15{,}000 \text{ ft} \\ 44 - 18\left(\frac{z-15{,}000}{35{,}000}\right) \text{ ft/sec} & \text{for } 15{,}000 \leq z \leq 50{,}000 \text{ ft} \end{cases}$$

The diminishing reference velocity at altitude reflects the reduced likelihood of severe weather-related gusts at higher altitudes. The reference velocity at the aircraft dive velocity V_d is half of its magnitude at the structural design velocity V_c:

$$U_{ref}|_{V_d} = \frac{U_{ref}|_{V_c}}{2}$$

Figures 4.4 and 4.5 show families of the 1–Cosine gusts for a 737-class aircraft as functions of the gradient length and altitude.

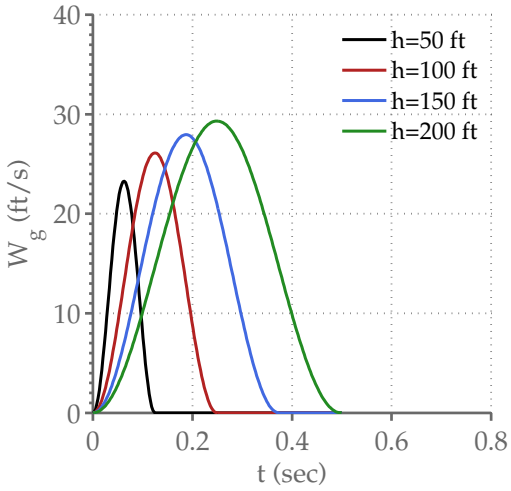

Figure 4.4. Positive 1–Cosine vertical gust fields at different gust gradient lengths H.

The discrete gust criterion defines a large number of potential gust encounters. We make a number of simplifying assumptions to render the design problem tractable. First, the FARs calls for both positive and negative gust encounters to be included in any airworthiness analysis. However, since a trimmed aircraft enters the gust at 1-g, positive gusts that add to the load are far more likely to be critical. We therefore exclude the negative gusts to halve the number of gust encounter simulations. Validation studies of optimized aircraft confirm that negative gusts do not represent critical design conditions.

Second, the gust design criteria is defined at both the structural design velocity V_c and the dive velocity V_d. One might expect the higher dive speed to present critical design conditions since gust loads scale linearly with velocity. However, the required vertical gust amplitude at V_d is only half of its value at V_c. We can then safely restrict the analysis to gust encounters at V_c.

Finally, we identify three representative gust encounter altitudes to simplify the

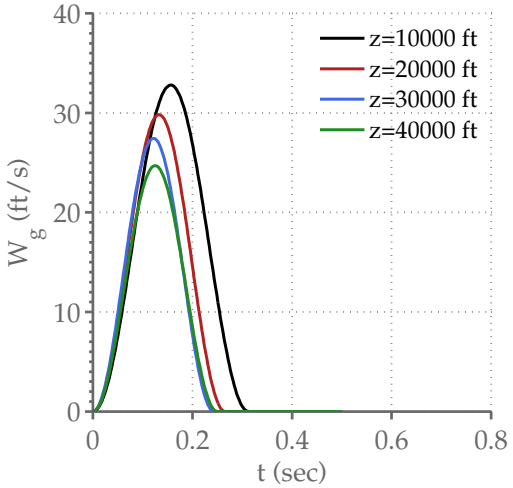

Figure 4.5. Positive 1–Cosine vertical gust fields at different gust encounter altitudes z.

analysis. Each aircraft is designed for gust encounters at 10,000 feet, initial cruise and final cruise. At each altitude we simulate gust encounters at 12 different gradient lengths ranging from 35 to 800 feet. The inclusion of longer, higher amplitude gusts – beyond the 350 feet maximum required by the FAR – adds a measure of conservatism to the analysis. The low altitude gust encounter combines high dynamic pressure with high gust amplitudes. Recall that U_{ref} increases with decreasing altitude. And below 10,000 feet the aircraft speed and dynamic pressure are restricted by regulations. The high-altitude cruise stage encounters may see reduced gust amplitudes but can still be critical because of the simultaneous and conflicting needs to achieve high span efficiency and low gust load.

The 1–Cosine criteria is a simplified *model* of atmospheric gust. The deterministic gust model fails to capture the stochastic nature of gust. The 1–Cosine gust model also cannot generally produce the "worst-case" gust.[37] And since the 1–Cosine gust for an aircraft at a given altitude is fully characterized by the gust gradient length, the gust shape can be fully anticipated by a more sophisticated GLA controllers. More sophisticated stochastic descriptions of gust such as the statistical discrete

gust (SDG)[28] and matched filter technique (MFT)[26] may be needed to address the shortfalls of the 1–Cosine gust. We give some preliminary thoughts on the challenge and opportunities presented by these gust design methods in chapter 8. As a model for sophisticated GLA control design, the 1–Cosine model clearly falls short. However, the model is still a useful for studying the performance limits of simple, reactive GLA controllers. The design framework should be understood as an aircraft design tool that incorporates gust constraints and rather than a detailed GLA design tool.

4.3.3 Gust Encounter Simulation

We include aircraft and structural dynamics in the gust load analysis. The immediate implication is that the maximum wing stress does not necessarily come from the highest amplitude gust. Aircraft can rise and fall with long-wave, high-amplitude gusts to reduce the effective induced angle of attack. We integrate the aircraft equations of motion in time to obtain the aircraft dynamic response. The 2-D pitch-plunge equations of motion can be written as:

$$\frac{W}{q_\infty S_{ref} \bar{c} g} \ddot{z} = C_{L\alpha} \alpha_g + C_{Lq} \dot{\theta}$$

$$\frac{W {r_y}^2}{q_\infty S_{ref} \bar{c} g} \ddot{\theta} = C_{M\alpha} \alpha_g + C_{Mq} \dot{\theta}$$

$$\alpha_g = \theta + \frac{w_g - \dot{z}}{V_\infty}$$

The aircraft weights and radii-of-gyration r_y are estimated based on a component buildup of aircraft mass and inertia at the relevant gust encounter flight conditions. The stability derivatives are computed using panel method and includes the effect of both control surface deflections and wing elasticity. The analysis assumes pseudo-steady aerodynamics: the stability derivatives and control inputs are updated at each time step. The pseudo-steady assumptions can be considered conservative because unsteady effects delay the lift buildup over the wings and afford the aircraft more time to adjust to gust.[37]

Although the analysis includes a 2-D pitch-plunge model, we typically restrict the simulation to a plunge-only model in the optimization. This is done to cope with dynamically unstable designs that generally arise in the course of the optimization. Fortunately, the plunge-only dynamics model is reflective of the fact that a GLA system would likely operate in the context of pitch stability augmentation. Figure 4.6 shows example aircraft dynamics from a series of simulations. The aircraft is an optimized laminar design with both MLA and GLA. The details of the design are discussed in chapter 6.

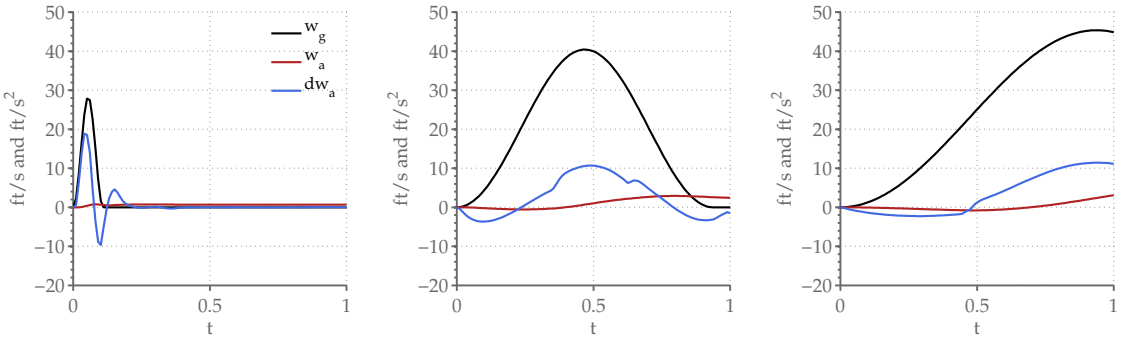

(a) H=35 ft **(b)** H=200 ft **(c)** H=600 ft

Figure 4.6. Aircraft dynamics through gust encounters.

The time histories of GLA control action can be found in figs. 4.7 and 4.8. Notice the effect of both the deflection bounds and the rate saturation in the actuator signals.

4.3.4 Structural Dynamics

The aircraft structural response is a function of the frequency content of the gust. Short-wave gusts in the 1–Cosine criteria contain little energy but can rate-saturate the GLA actuators. However, the wing would experience little stress if the structure is slow to respond to high speed excitations. For an aircraft flying at a typical Mach number of 0.78 at 30,000 ft, the FAR-specified gust gradients have reduced

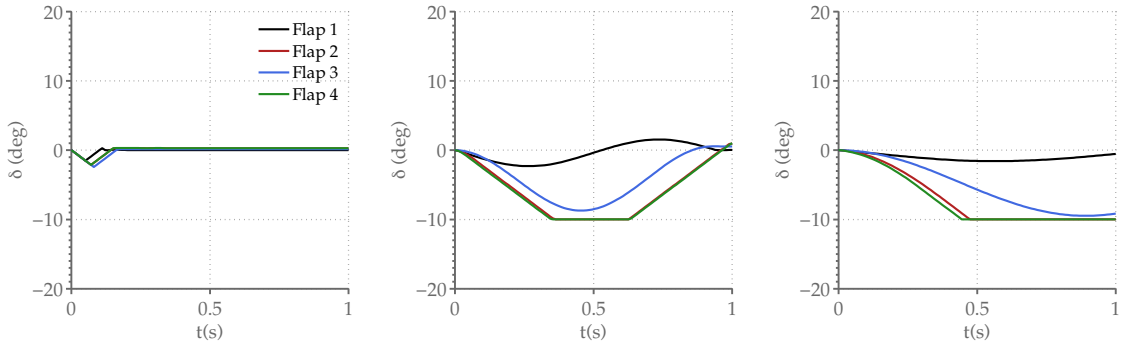

(a) H=35 ft **(b)** H=200 ft **(c)** H=600 ft

Figure 4.7. Control surface deflection time history for each trailing edge channel.

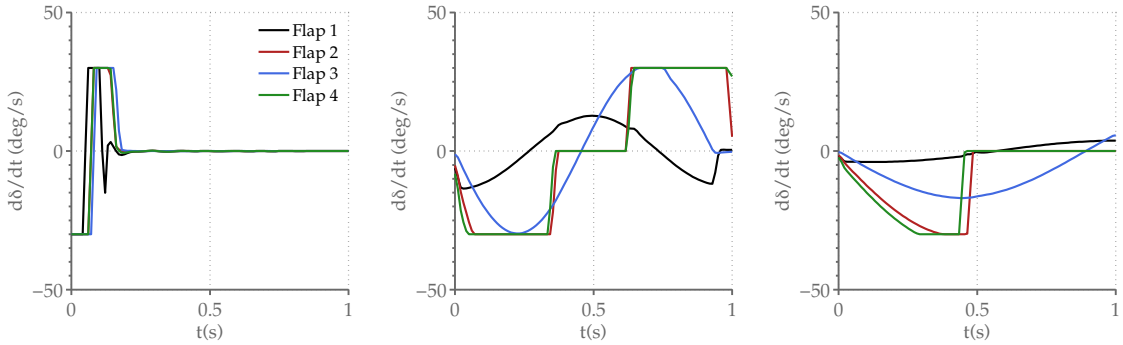

(a) H=35 ft **(b)** H=200 ft **(c)** H=600 ft

Figure 4.8. Control deflection rate laminar MLA+GLA design.

frequencies of between 0.2 to 8Hz. The natural frequency of typical transport wings is around 2Hz. The high frequency components of the gust spectrum can therefore be much faster than the fundamental bending frequency of the wing. The implication is that an accurate analysis of gust load should include the structural dynamics of the wing.

Direct Stiffness Solution

We model the wing structure as a variable cross section beam in forced vibration to characterize its dynamic response. The equation of motion of the wing can be written in terms of its global mass, stiffness and damping matrices and the generalized displacement $\boldsymbol{u}$:[57,58]

$$\boldsymbol{M}\ddot{\boldsymbol{u}}(t) + \boldsymbol{C}\dot{\boldsymbol{u}}(t) + \boldsymbol{K}\boldsymbol{u}(t) = \boldsymbol{F}(t) \tag{4.4}$$

The stiffness matrix of the Euler-Bernoulli beam element with rigidity EI and length L is:

$$\boldsymbol{K^e} = \frac{EI}{L}\begin{bmatrix} 12/L^2 & 6/L & -12/L^2 & 6/L \\ 6/L & 4 & -6/L & 2 \\ -12/L^2 & -6/L & 12/L^2 & -6/L \\ 6/L & 2 & -6/L & 4 \end{bmatrix}$$

The centroids of the FEM elements are collocated with the y-positions of the aerodynamic control points. A beam element with cross sectional area A and uniform material density ρ has the following *consistent* mass matrix:

$$\boldsymbol{M^e} = \frac{\rho AL}{420}\begin{bmatrix} 156 & 22L & 54 & -13L \\ 22L & 4L^2 & 13L & -3L^2 \\ 54 & 13L & 156 & -22L \\ -13L & -3L^2 & -22L & 4L^2 \end{bmatrix}$$

We develop a beam finite element methods (FEM) kernel to assemble the global stiffness and mass matrices.[57,58] The global mass and stiffness are then used to obtain the direct stiffness solution.

Modal Decomposition

The discretized equations of motion can be numerically integrated in time for the wing displacement. Direct integration of eq. (4.4) is however both expensive and error-prone. A more efficient approach is to apply the principles of linear modal decomposition to decouple the structure modes. We can then integrate only the low-frequency modes, which contain the majority of the vibrational energy. We transform the equations of motion into the modal coordinate system $\boldsymbol{y}(t)$ using the orthonormal set of eigenvectors $\bar{\boldsymbol{Q}}$:

$$\begin{aligned}
\boldsymbol{u}(t) &= \bar{\boldsymbol{Q}}\boldsymbol{y}(t) \\
\bar{\boldsymbol{M}} &= \bar{\boldsymbol{Q}}^{\boldsymbol{T}}\boldsymbol{M}\bar{\boldsymbol{Q}} = [\boldsymbol{I}] \\
\bar{\boldsymbol{K}} &= \bar{\boldsymbol{Q}}^{\boldsymbol{T}}\boldsymbol{K}\bar{\boldsymbol{Q}} = \left[\omega^2\right] \\
\bar{\boldsymbol{C}} &= \bar{\boldsymbol{Q}}^{\boldsymbol{T}}\boldsymbol{C}\bar{\boldsymbol{Q}} \\
\bar{\boldsymbol{F}}(t) &= \bar{\boldsymbol{Q}}^{\boldsymbol{T}}\boldsymbol{F}(t)
\end{aligned}$$

For proportionally damped and undamped systems the modal solution of the natural frequency and mode shapes represents a generalized eigenvalue problem:

$$\boldsymbol{KQ} = \boldsymbol{\omega}^2\boldsymbol{MQ}$$

An explicit inversion of the mass matrix is inefficient and potentially inaccurate. We leverage the symmetric properties of the mass matrix and use Cholesky factorization to recast the eigenvalue problem into the standard form:

$$\begin{aligned}
\boldsymbol{L^{-1}KL}^{-T}\left[\boldsymbol{L}^T\boldsymbol{Q}\right] &= \boldsymbol{\omega}^2\left[\boldsymbol{L}^T\boldsymbol{Q}\right] \\
\boldsymbol{M} &= \boldsymbol{L^{-1}KL}
\end{aligned}$$

The equations of motion can now be readily decoupled into scalar ODEs of the form:

$$\ddot{y}_i(t) + 2\zeta_i\omega_i\dot{y}_i(t) + {\omega_i}^2 y_i(t) = \bar{f}_i(t)$$

We conduct validation studies to ensure that the numerical solution of the mode shapes and natural frequencies match the analytic solutions for beams in free vibration.

Each decoupled ODE can be independently integrated as a superposition of piecewise exact second-order impulse responses.[59] The numerical integration scheme is outlined in appendix B. We validate the numerical integration using analytic solutions of second-order system response to impulse and step excitations. We choose to retain the first 4 structural modes in the numerical integration to reduce the dimensionality of the problem. The generalized displacement $\boldsymbol{u^e}$ can be recovered from the modal displacement using the inverse of the modal transformation. The element bending moment is related to the displacement by the strain-displacement transformation $\boldsymbol{B^e}$:

$$M^e = EI\frac{d^2v}{dx^2} = EI\boldsymbol{B^e}\boldsymbol{u^e}$$

$$\boldsymbol{B^e} = \begin{bmatrix} \frac{-6}{L^2} + \frac{12x}{L^3} & \frac{-4}{L} + \frac{6x}{L^2} & \frac{6}{L^2} - \frac{12x}{L^3} & \frac{-2}{L} + \frac{6x}{L^2} \end{bmatrix}$$

The element bending moment are finally related to the stress by the Euler-Bernoulli equation. The time-dependent wing stresses from the gust load constraints that ultimately size the wing. The numerical solutions of the structural dynamics are validated using beam test cases.

Aerodynamic Stiffness and Damping

Strictly speaking the modal decomposition scheme is only valid for *proportionally* damped system, where the damping matrix $\boldsymbol{C}$ can be written as a linear combination of the mass and stiffness matrices:

$$\boldsymbol{C} = \alpha\boldsymbol{M} + \beta\boldsymbol{K}$$

In general proportional damping is an artificial construction and does not capture the physics of damping in real structures. In the present problem for example the wing structural dynamics is characterized by strong non-proportionally aerodynamic damping $\boldsymbol{\theta}_d$ from wing flapping:

$$\boldsymbol{\theta}_d \approx \frac{\dot{\boldsymbol{u}}}{V_\infty}\sin\Lambda_e$$

One way to incorporate non-proportional aerodynamic damping is to include it as external force. At each time-step we first compute the equivalent wing twist from flapping using the deflection rates from the previous time-step. We use the apparent twist to update the aerodynamic boundary conditions for the panel method and obtain the flow solution at the next step. The process is repeated at all time steps.

An analogous numerical approach is used to include the time-dependent aerodynamic stiffness term $\boldsymbol{\theta}_s$ in the analysis:

$$\boldsymbol{\theta}_s \approx \frac{2\boldsymbol{u}}{b} \sin \Lambda_e$$

The modified equations of motion can be written as:

$$\boldsymbol{M}\ddot{\boldsymbol{u}}(t) + \boldsymbol{C}\dot{\boldsymbol{u}}(t) + \boldsymbol{K}\boldsymbol{u}(t) = \boldsymbol{F}(t) + \boldsymbol{F_d}(t) + \boldsymbol{F_s}(t)$$

Where F_d and F_s are the generalized pseudo-forces from wing damping and stiffness. The advantage of this numerical approach is that it leaves the wing modal decomposition unchanged. The updated damping and stiffness pseudo-forces must however be converted into the modal coordinate system at every time step. An example of the dynamic stress constraint time history through a gust encounter can be found in fig. 4.9. The aircraft is the same Laminar MLA+GLA design. The results show that a GLA system has effectively suppressed the low to intermediate frequency gusts, which leaves the high frequency gusts to design the wing.

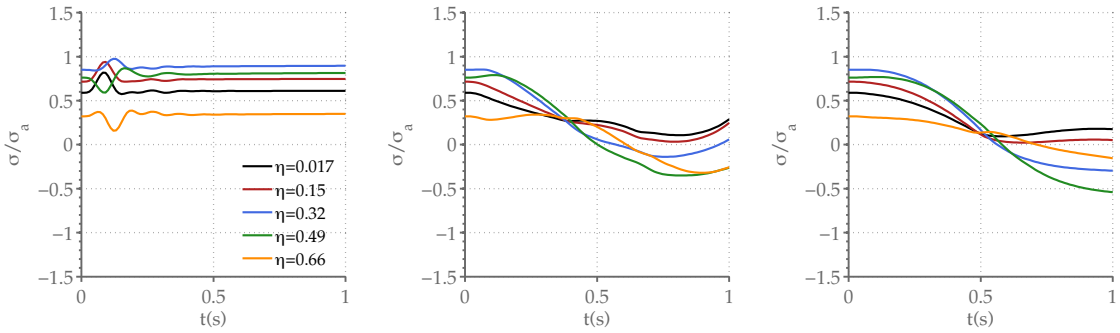

(a) H=35 ft **(b)** H=200 ft **(c)** H=600 ft

Figure 4.9. Dynamic wing stresse constraints.

Chapter 5

Design Studies

In this chapter we apply the aeroservoelastic conceptual design framework to a series of short-haul aircraft design studies. The goal is to quantify the system-level performance impacts of active load control and natural laminar flow. The design studies are driven by optimization: we rely on the non-linear optimizer to *synthesize* the aircraft.

5.1 Optimizer

The introduction of load alleviation and NLF greatly increases the number of required design variables compared to a more conventional design. The scale of the design problem leads us to use a monolithic optimization architecture. We use the FMINCON constrained nonlinear optimization system in MATLAB to optimize the aircraft design. FMINCON use a quasi-Newton solver with BFGS updates. In this thesis the active-set algorithm is used to efficiently handle the large numbers of dynamic and static stress constraints. Importantly, the analysis methods have been made smooth to support the gradient-based optimizer.

5.2 Baseline

The baseline aircraft use in the optimization is a Boeing 737-class airliner with a cruise range of 2,000 nautical miles. The passenger and payload capacity are based on published figures for the Boeing 737-800: 162 passengers in a 3-class layout. All aircraft have low-wing, T-tails and fuselage-mounted engines. The configuration is meant to keep the wing clean and compatible with NLF. The primary structures are conventional aluminum.

(a) Turbulent **(b)** Laminar

Figure 5.1. Examples of the high-sweep turbulent and low-sweep NLF aircraft families. The transition fronts are shown in green.

In the optimization we distinguish between aircraft designed with turbulent and laminar wings. The discontinuity between the designs reflects a basic limitation in our viscous design tool. Namely that the 2-D transition prediction method outlined in section 3.5 is applicable only to high-aspect ratio wings of moderate sweep. Turbulent aircraft on the other hand are not subject to this methodological limitation. To cope with the limitation in the viscous design tool we develop two distinct optimization baselines: 1) turbulent aircraft with wing sweep of up to 40° and 2) NLF designs with wing sweep of less than 10°. We force transition near the leading edge on the turbulent wings. And the wing-fuselage intersection is assumed to be turbulent even on the NLF aircraft to reflect the dominant effects of attachment line instabilities at the intersection. The two baselines are compared in fig. 5.1.

Finally, the NLF wings in this study are designed with turbulent lower surfaces. This may seem counterintuitive because laminar flow is easier to maintain on the lower wing surface, where flow acceleration is modest and the pressure recovery relatively benign. However, surface contamination can be more likely on the bottom wing surface and lead to early transition. Moreover, since the wing profile drag arises from the interaction between boundary layer growth and supervelocity,[12] maintaining laminar flow on the upper wing, where the supervelocity is high, is far more important for the purpose of drag reduction. Finally, as discussed in section 3.3, slat gaps integrated on the bottom wing surface can disrupt laminar flow.

5.3 Objective

We optimize the aircraft for minimum operating cost, which is estimated using an extended version of the Airline Transport Association (ATA) method.[60] The utility of the simplified cost model is limited to comparing the *relative* merit of designs with *comparable* technology contents. The ATA model cannot therefore account for the development and maintenance cost of novel load alleviation systems or NLF wing. However, a preliminary operating cost estimate can still be used to assess the economic viability of new programs to develop NLF wings or aggressive active load control systems. Details of the cost analysis can be found in appendix C. The key cost assumptions and inputs are summarized in table 5.1. In particular, the market price of aviation fuel can have a decisive role influence on the aircraft design. The results presented in this thesis can change significantly with fluctuating fuel prices. This sensitivity to fuel price should be investigated in future studies.

Fuel Cost	\$2.5/gal
Labor Rate	\$38/hour
Insurance Rate	0.2%

Table 5.1. Key cost assumptions.

5.4 Variables

We introduce the design variables in the methodology chapters to provide context for the aircraft parameterization and optimization. We now summarize all of the variables in table 5.2 for clarity and to convey the scale of the design problem.

Variables	
Mission	$\boldsymbol{x_{mission}} = [z_i, z_f, M_{to}, M_{land}, \delta_{to}, \delta_{land}]$
Aircraft	$\boldsymbol{x_{aircraft}} = \left[\frac{S_h}{S_{ref}}, x_{root}, W_{MTOW}, W_{MZFW}, T_0, x_{mg}\right]$
Wing	$\boldsymbol{x_{wing}} = \left[S_{ref}, AR, \lambda, \Lambda_{1/4}, \boldsymbol{\Delta c}, \boldsymbol{\theta}, \boldsymbol{t(x_e)}, \boldsymbol{t(x_f)}, \boldsymbol{t(x_a)}, \boldsymbol{t_s}, \boldsymbol{t_w}\right]$
Pressure	$\boldsymbol{x_{pressure}} = \left[\boldsymbol{x_r}, \boldsymbol{C_{p_{LEl}}}, \boldsymbol{C_{p_{LEu}}}, \left(\frac{\boldsymbol{dC_p}}{\boldsymbol{dx}}\right)_{\boldsymbol{u}}, \left(\frac{\boldsymbol{dC_p}}{\boldsymbol{dx}}\right)_{\boldsymbol{l}}, \boldsymbol{S_u}\right]$
Transition	$\boldsymbol{x_{transition}} = \boldsymbol{x_t}$
MLA	$\boldsymbol{x_{MLA}} = \boldsymbol{\delta}$
GLA	$\boldsymbol{x_{GLA}} = [\boldsymbol{k_p}, \boldsymbol{k_d}]$

Table 5.2. Summary of all optimization variables.

The wing trailing edge extensions, twist and wing box geometry are defined at all wing break sections. The section pressure distributions and transition locations are defined at the wing break sections for the cruise segment. The transition variables are only included in the optimization for NLF sections with free transition. The MLA

control surface is scheduled for each maneuver condition. The GLA control gains are defined for each trailing edge control surface.

5.5 Constraints

The optimization is subject to the large number of design constraints discussed in chapter 2. Within the optimization the constraints are normalized by the appropriate reference values to improve convergence. All of the design constraints are summarized in table 5.3 for clarity.

The aircraft lift-matching, trim and stability constraints are imposed at all flight conditions outlined in section 2.2. The aileron effectiveness constraint is imposed at the structural cruise speed V_c:

The wing maximum lift constraints are imposed at each wing station for all flight conditions. The wing static stress constraints are imposed at each wing station in the cruise, gust and maneuver flight conditions. The wing dynamic stress constraints are imposed at each wing station over the time frame of each gust encounter.

The pressure, wing box and transition compatibility constraints are imposed at each wing break section in the cruise segment. Transition compatibility are only enforced for surfaces with free transition. Since we assume that the bottom surface of NLF wing is turbulent, no transition compatibility constraints are imposed on the bottom surfaces.

Aircraft	$x_{mg} = \dfrac{\max(\boldsymbol{x_{CG}}) - 0.08x_{ng}}{0.92}$ $W_{MTOW} = W_{MZWF} + W_{fuel} + W_{res}$
Performance	$l_{to} < 7{,}900\text{ft},\ l_{land} < 5{,}500\text{ft},\ h_c > 0.024$ $\dfrac{D}{T}_i < 0.88,\ \dfrac{D}{T}_f < 0.88,\ R > 2{,}000\text{nm}$
Trim	$C_{Lh} < C_{Lhmax},\ nW = \dfrac{\rho v^2 S_{ref} C_L}{2}$
Stability	$-\dfrac{dC_{Mac}}{dC_L} > 0.10\overline{c}$
Maximum Lift	$C_l(\eta) < \begin{cases} C_{lmax}(\eta) & \text{if } \eta < 0.75 \\ C_{lmax}(\eta) - 0.2 & \text{otherwise} \end{cases}$
Pressure	$\int_0^c \left[C_{p_l}(x) - C_{p_u}(x)\right] dx > C_l(\eta)$ $M_{ru\perp} < 1.1,\ M_{rl\perp} < 0.95$
Wing Box	$t_{inv}(x_e) > t_e,\ t_{inv}(x_f) > t_f$ $t_{inv}(x_a) > t_a,\ t_{inv}(x_{te}) = 0$
Transition	$Re_x(x_t) < Re_{e^9}(x_t)$
Static Stress	$\{\sigma(\eta)\} < \sigma_a,\ \{\tau(\eta)\} < \tau_a$
Dynamic Stress	$\{\sigma(\eta, t)\} < \sigma_a,\ \{\tau(\eta, t)\} < \tau_a$
Aileron Reversal	$\left.\dfrac{L_{e\delta_4}}{L_{r\delta_4}}\right\rvert_{V_c} > 0.525$

Table 5.3. Summary of all optimization constraints.

Chapter 6

Results

This chapter details the results of a number of design studies meant to demonstrate the workings of the aeroservoelastic conceptual design framework. We first present a series of optimized turbulent aircraft with varying degrees of active load alleviation: no load alleviation, MLA-only, GLA-only and finally both MLA and GLA (MLA+GLA). This is followed by an analogous series of laminar aircraft with different load alleviation systems. Finally, we compare the turbulent and laminar MLA+GLA designs in detail to highlight the potential synergy between active load alleviation and laminar flow. The results include both "point optimizations" at a cruise Mach number of 0.78 and optimization sweeps with cruise Mach numbers ranging from 0.70 to 0.82. We treat the Mach 0.78 turbulent aircraft designed without load alleviation as the baseline against which all other data are normalized.

6.1 Turbulent Designs

6.1.1 Point Optimizations

The four optimized turbulent aircraft are compared in fig. 6.1. In each design we force flow transition near the leading edge to ensure turbulent flow over the wing. The transition lines are highlighted in green.

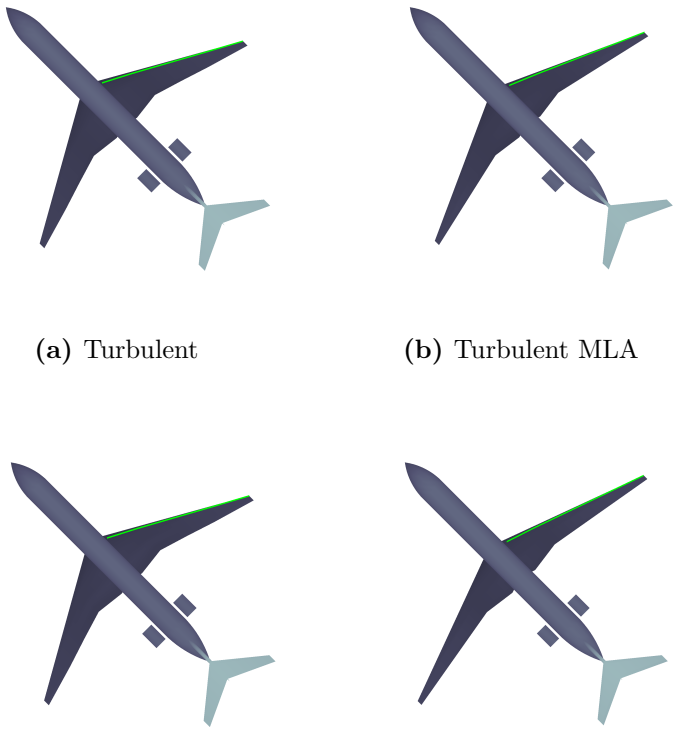

(a) Turbulent **(b)** Turbulent MLA

(c) Turbulent GLA **(d)** Turbulent MLA+GLA

Figure 6.1. The optimized Mach 0.78 turbulent aircraft with different levels of active load alleviation.

The details of the aircraft and wing configuration are tabulated in table 6.1.

The optimized Mach 0.78 turbulent aircraft in fig. 6.1a represents a conventional

	Turbulent	Turbulent MLA	Turbulent GLA	Turbulent MLA+GLA
W_{MTOW} (lb)	158,065	153,146	158,547	148,139
W_{fuel} (lb)	25,916	25,030	25,779	23,520
W_{wing} (lb)	19,200	16,582	19,720	14,637
T_0 (lb)	21,367	20,607	21,267	18,963
S_{ref} (ft^2)	1,652	1,512	1,678	1,497
b (ft)	136	140	137	151
AR	11.2	13.0	11.2	15.3
$\Lambda_{1/4}$ (Deg)	26.6	21.7	26.6	17.6
$\overline{t/c}$	0.096	0.089	0.096	0.091
L/D	18.2	18.3	18.4	19.0
z_i	30,095	30,535	30,178	30,951
z_f	41,514	41,496	41,554	41,190

Table 6.1. Summary of optimized Mach 0.78 turbulent aircraft design parameters.

short-haul design in the same class as the Boeing 737 and the Airbus A320. In fact, the optimized maximum takeoff weight matches well with the published figure of the Boeing 737-800 at 155,500 lb. The wing sweep of 26.6° and average cruise L/D of 18 are also in line with the 737. The optimized span at 136 feet is on the other hand substantially greater than the span of both the 737-800 at 117 feet and the Airbus A320 at 111 feet. The difference is in part attributable to the absence of gate compatibility constraints in the optimization. We examine the sensitivity of the aircraft design to gate constraints in the next chapter.

Compared with the baseline, the Turbulent MLA aircraft in fig. 6.1b shows a modest increase in span from 136 to 140 feet. The introduction of MLA decreases the optimum wing sweep by 5°. A simultaneous decrease in the area-weighted average thickness-to-chord $\overline{t/c}$ from 9.6 to 8.9% compensates for the compressibility penalties of reduced sweep.

The MLA wing is both thinner and longer than the baseline wing but still manages to be some 3,000 lb *lighter*. Load alleviation clearly leads to tangible gains in structural efficiency. The effectiveness of the MLA system acting alone also suggests that maneuver loads likely size a substantial portion of the baseline wing.

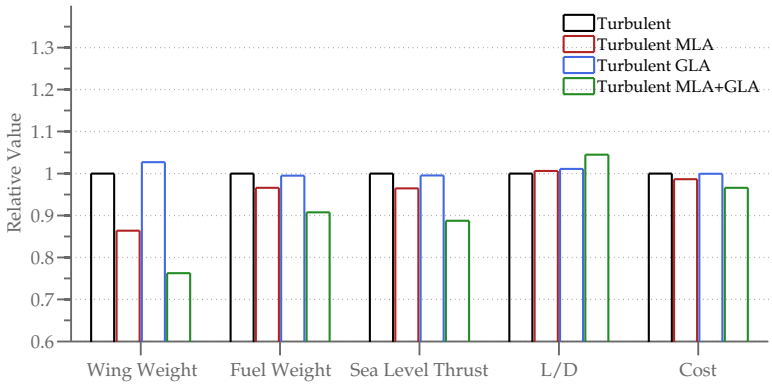

	Turbulent	Turbulent MLA	Turbulent GLA	Turbulent MLA+GLA
Wing Weight	1.000	0.864	1.027	0.762
Fuel Weight	1.000	0.966	0.995	0.908
Sea Level Thrust	1.000	0.964	0.995	0.888
L/D	1.000	1.006	1.011	1.045
Cost	1.000	0.987	0.999	0.966

Figure 6.2. A comparison of the optimized turbulent aircraft. The performance metrics and configuration parameters are normalized against the corresponding values of the Mach 0.78 turbulent baseline.

The GLA design shown in fig. 6.1c on the other hand, is nearly identical to the baseline. The only difference is the formers slightly larger wing. The other planform parameters are all within 1% of their baseline values. Gust loads then are clearly not sizing the baseline wing in any significant way. This result is not surprising because high wing sweep leads to significant aerodynamic stiffness and damping in gust encounters.

Figure 6.1d shows that the application of *both* MLA and GLA significantly alters the optimized configuration. Compared to the baseline the MLA+GLA wing is not only 15 feet longer but also 25% lighter. The sweep is reduced to 18°. The gain in L/D is modest in part because the ATA cost model used in the present analysis scales the aircraft manufacturing cost against the zero-fuel weight. Under this model the light aircraft is not only more efficient in lift but also costs less. It should be emphasized that the results in this chapter are all based on a fuel price of \$2.5/gal. The balance between weight and fuel savings is fundamentally dependent on fuel prices.

In certain cases it is convenient to examine the *relative* changes in performance metrics and design parameters. The parameters in fig. 6.2 are normalized to their baseline values in the Mach 0.78 turbulent design. We observe that the independent application of MLA has led to a modest but tangible 3.4% reduction in fuel burn and 1.3% reduction in cost. The independent application of GLA on the other hand produces only negligible gains. The combination of MLA and GLA has led to a significant 10% reduction in fuel burn and 3.4% reduction in cost.

The exposed wing planforms of the turbulent aircraft are compared in fig. 6.3. Once again we normalize the relevant parameters by their baseline values. The figure highlight visually the similarity between the baseline and GLA wing and a clear trend towards increased span and decreased wing sweep with the successive addition of load alleviation technologies.

Figure 6.4 compares the turbulent wing and skin thickness distributions. The increased structural efficiency of the MLA and MLA+GLA aircraft leads to reduced wing and skin thicknesses. As load alleviation reduces the stress constraints, aeroelasticity can become dominant considerations. The optimizer chooses therefore to

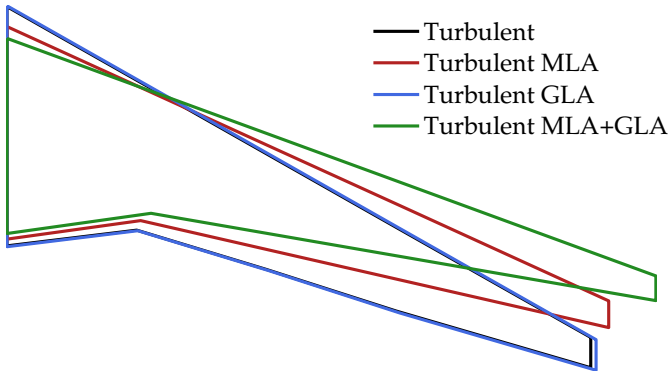

	Turbulent	Turbulent MLA	Turbulent GLA	Turbulent MLA+GLA
S_{ref}	1.00	0.92	1.02	0.91
b	1.00	1.03	1.01	1.11
Λ	1.00	0.82	1.00	0.66
$\overline{t/c}$	1.00	0.93	1.00	0.95
AR	1.00	1.16	1.00	1.36

Figure 6.3. A comparison of the optimized turbulent wing planforms. All parameters are normalized by their values in the Mach 0.78 turbulent baseline.

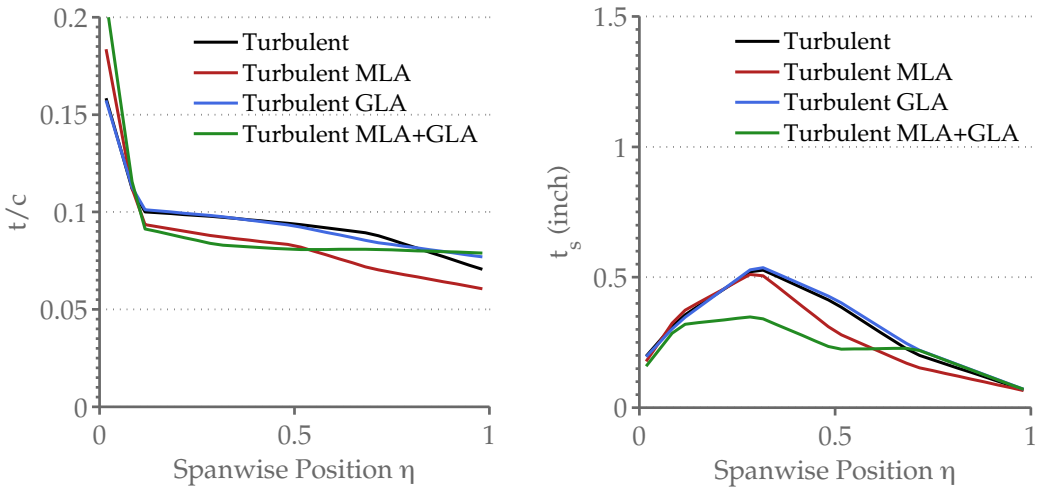

(a) Wing t/c **(b)** Skin Thickness (inch)

Figure 6.4. Turbulent wing and skin thickness distributions.

increase the outboard stiffness to prevent aileron reversal and increase MLA control authority.

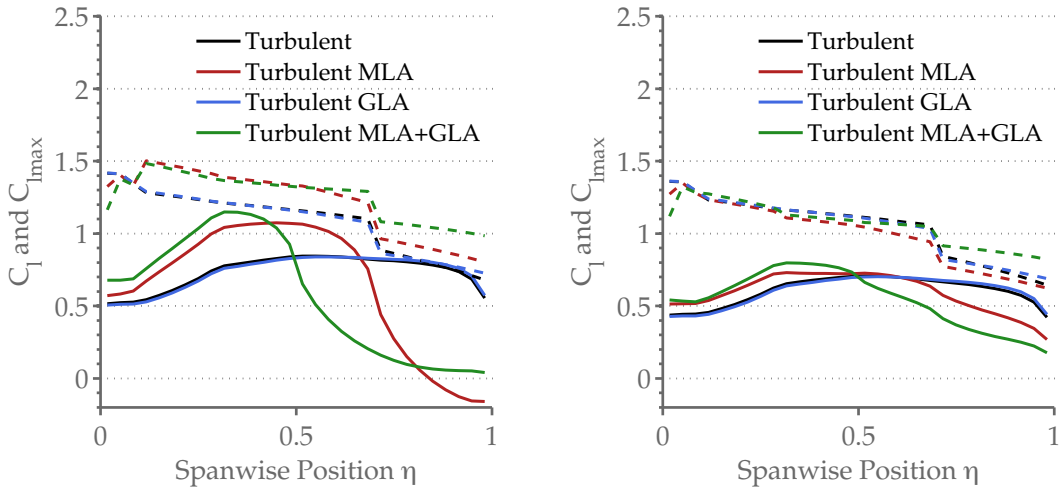

(a) 2.5-g at 30,000 ft **(b)** 1.3-g at 40,000 ft

Figure 6.5. Comparisons of the turbulent maneuver C_l (solid lines) and $C_{l_{max}}$ (dashed lines) distributions.

We compare the maneuver C_l distributions of the turbulent aircraft in fig. 6.5. The C_l distributions show that the MLA system has concentrated load inboard to reduce bending and shear stresses. In the MLA design for example the wing tips are actually *negatively* loaded in the 2.5-g maneuvers. In this case the lift penalties are more than offset by the greatly increased load alleviation inboard. The drag penalties from the negatively loaded tips do not directly affect the design because the maneuvers do not have to be performed at constant altitude.

The dashed lines in fig. 6.5 corresponds to the section $C_{l_{max}}$. A discontinuous change in the section maximum lift indicates a change in the trailing edge controls surface deflection. The actions of the MLA system on the turbulent designs, which gave relatively thick wings enabled by sweep, are not constrained by the lift limit.

We examine the structure design in more detail in fig. 6.6, which overlays the maneuver and gust-induced wing stresses to highlight which load is sizing each section of the

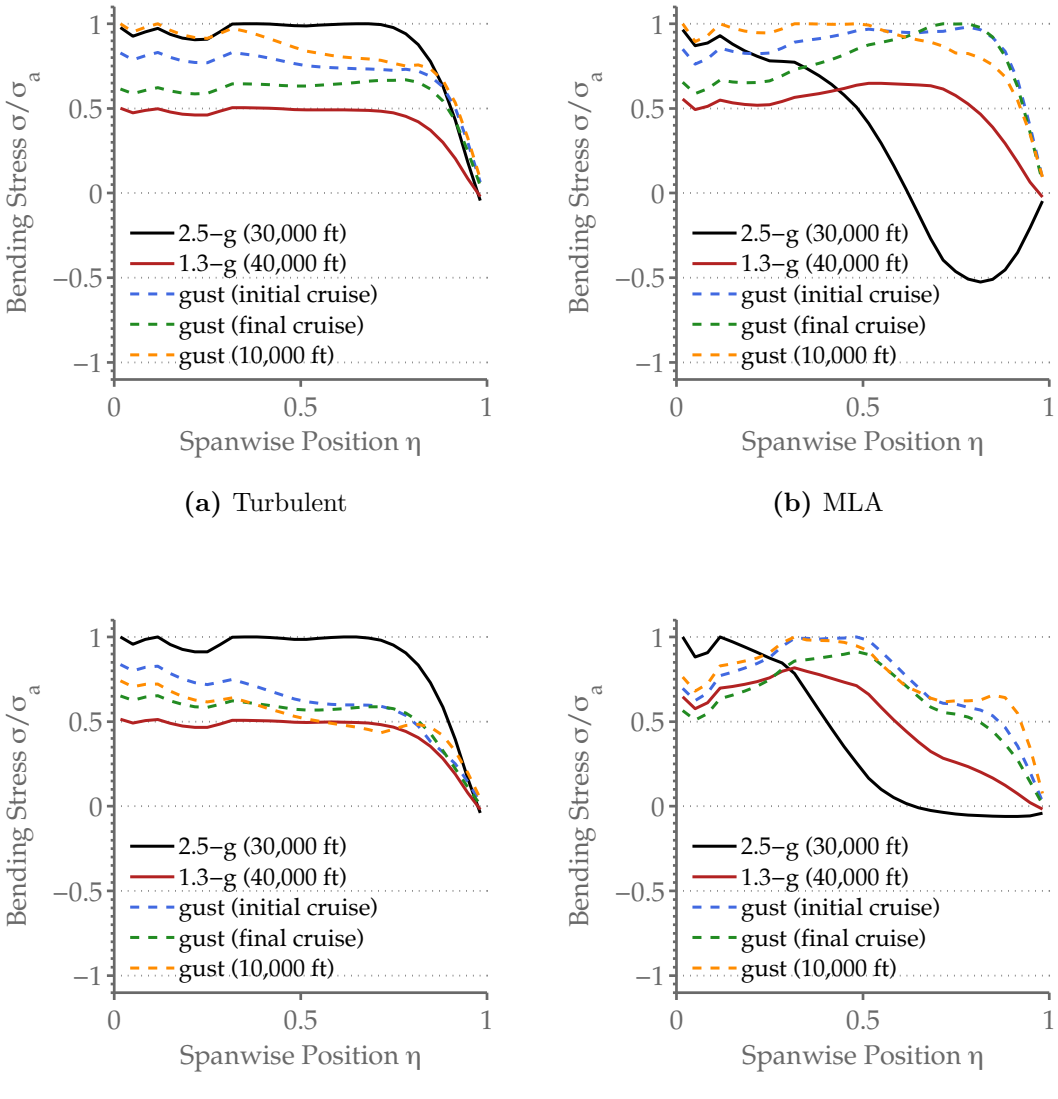

(a) Turbulent **(b)** MLA

(c) GLA **(d)** MLA+GLA

Figure 6.6. Maneuver and gust bending stresses for the optimized turbulent designs at Mach 0.78. The wing bending stresses σ are normalized by the allowable stress σ_a. The gust stresses represent the maximum values encounter by each wing section at all gust gradient lengths.

wing. The maneuver loads at 1.3 and 2.5-g are shown as solid lines. The dashed lines are formed by the maximum stresses at each wing section for all of the time-domain gust simulations at a given altitude. The maximum stresses are normalized by the allowable stresses σ_a. fig. 6.6 is therefore a visual representation of both the optimized state of the static and dynamic stress constraints discussed in chapter 4. A wing section is deemed stress-critical if the local stress ratio σ/σ_a reaches their limit values of 1 or -1.

The plot of stress constraints confirms that the turbulent baseline wing structure is essentially sized by maneuver loads. Much of the inboard wing is fully-stressed in maneuver. The outboard sections are designed by minimum gauge. The MLA system significantly reduces the maneuver load but leaves the wing to be designed by gust. Figure 6.6b shows that the Turbulent MLA wing is designed by low-altitude gusts inboard and cruise stage gusts outboard. So while the MLA system has diminished the role of maneuver loads in structural sizing, the gust loads remain to undercut the potential structural savings. The opposite is true in the case of the GLA wing stresses shown in fig. 6.6b. Here the wing is designed almost exclusively by maneuver loads.

Finally, fig. 6.6d demonstrates that the MLA+GLA wing is designed by both maneuver and gust loads. We also observe that the outboard portions of the wing are far from being fully-stressed; they are instead sized by the aforementioned aeroelastic and minimum gauge considerations.

6.1.2 Mach Number Sweeps

The aircraft presented thus far are all designed to cruise at Mach 0.78. We now present the cost and fuel burn trends of the four turbulent aircraft as functions of the cruise Mach number. The cost and fuel burn metrics shown in figs. 6.7 and 6.8 are normalized by the cost and fuel weight of the baseline design at Mach 0.78.

The results in Figure 6.7 demonstrate that at a fuel price of $2.5 per gallon the

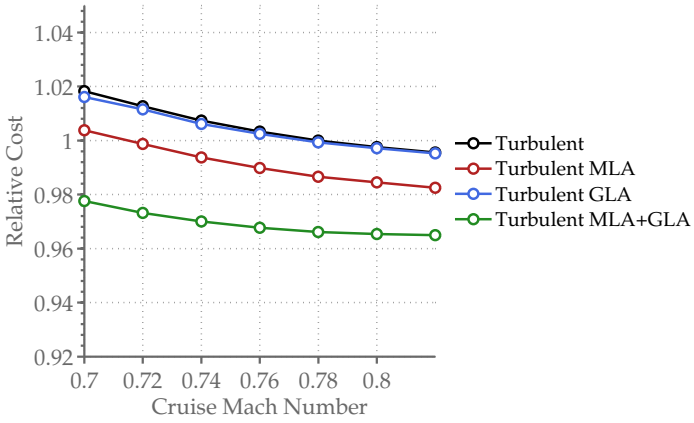

Figure 6.7. A plot of the relative operating cost of optimized turbulent designs as functions of Mach number. Each point represents an optimized aircraft. The performance metrics are normalized to the Mach 0.78 baseline.

minimum-cost objective continues to favor speed over fuel savings. Cost continues to fall with increasing Mach number. Only the MLA+GLA design flat-lines near Mach 0.82. So while the turbulent designs can slow down to reduce fuel burn, they can only do so at higher costs.

Figures 6.7 and 6.8 show that the relative savings from the independent application of MLA and GLA are constant across the range of Mach numbers. The savings from the MLA+GLA are however dependent on the Mach number. We reason that aileron reversal constraints, which become more critical with increased speed, diminish the savings from load alleviation.

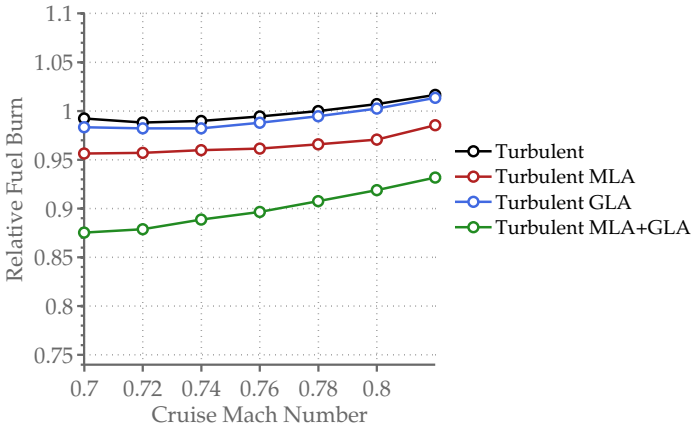

Figure 6.8. A plot of the relative fuel burn of optimized turbulent designs as functions of Mach number. Each point represents an optimized aircraft. The performance metrics are normalized to the Mach 0.78 baseline.

6.2 Laminar Designs

6.2.1 Point Optimizations

The optimized NLF aircraft with different levels of load alleviation are compared in fig. 6.9. The wing sweeps of the NLF designs are restricted to less than 10°– a limit that is inevitably reached. The upper wing surfaces are designed for laminar flow while the lower surfaces are assumed to be turbulent.

We observe that in all but the MLA+GLA aircraft, the region of extensive laminar flow is restricted to the outboard portions of the wings. This result underscores the severe structural penalties faced by a low-sweep NLF design at transonic speed. The optimizer favors weight savings from improved structural efficiency than aerodynamic benefits from extensive laminar flow. The data in table 6.2 show that all of the laminar designs reach their maximum wing sweep of 10°. This result is also consistent with the strong aerodynamic and aeroelastic incentives to increase wing sweep. Moreover, since the boundary layer analysis does not include crossflow, there is no viscous penalty against high wing sweep.

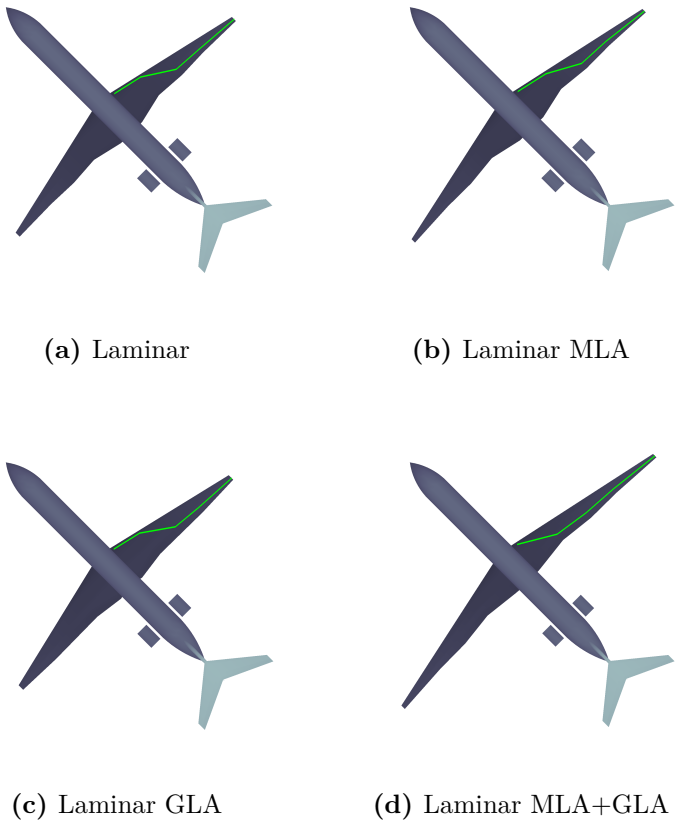

(a) Laminar **(b)** Laminar MLA

(c) Laminar GLA **(d)** Laminar MLA+GLA

Figure 6.9. The optimized Mach 0.78 turbulent aircraft with different levels of active load alleviation.

	Laminar	Laminar MLA	Laminar GLA	Laminar MLA+GLA
W_{MTOW} (lb)	160,904	157,382	158,961	148,897
W_{fuel} (lb)	25,780	25,036	25,032	21,833
W_{wing} (lb)	21,701	20,295	20,783	17,437
T_0 (lb)	21,569	20,756	20,638	17,845
S_{ref} (ft^2)	1,503	1,376	1,647	1,489
b (ft)	145	155	141	169
AR	14.0	17.4	12.0	19.1
$\Lambda_{1/4}$ (Deg)	10.0	10.0	10.0	10.0
t/c	0.088	0.091	0.091	0.090
L/D	18.7	18.9	19.1	20.9
z_i	29,531	30,310	30,191	30,019
z_f	41,998	41,784	41,604	42,000

Table 6.2. Summary of Mach 0.78 high sweep NLF aircraft parameters.

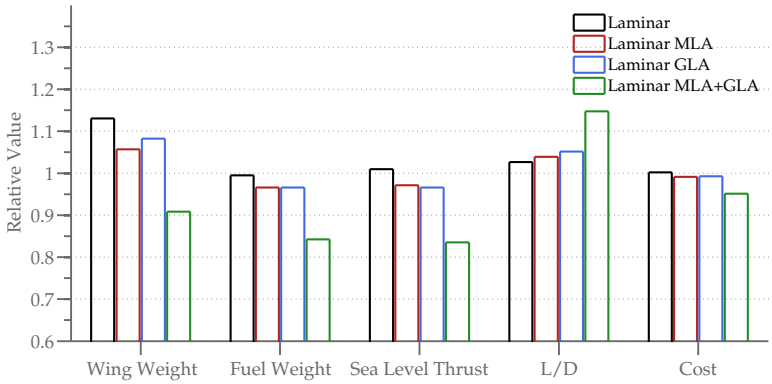

	Laminar	Laminar MLA	Laminar GLA	Laminar MLA+GLA
Wing Weight	1.130	1.057	1.082	0.908
Fuel Weight	0.995	0.966	0.966	0.842
Sea Level Thrust	1.009	0.971	0.966	0.835
L/D	1.027	1.039	1.052	1.148
Cost	1.002	0.991	0.993	0.951

Figure 6.10. A comparison of the optimized laminar aircraft. The performance metrics and configuration parameters are normalized by those of the Mach 0.78 turbulent baseline.

Figure 6.10 compares the key design parameters of the different laminar aircraft. The thrust, L/D, weight and costs are all normalized by the corresponding turbulent baseline values. The NLF aircraft achieves only a negligible 0.5% gain in fuel savings and also costs more to operate. The thin, NLF wing contributes to a 2% improvement in aircraft L/D but weighs 13% more than the baseline. The lackluster performance of the NLF design is therefore directly attributable to the penalties associated with unsweep.

The results from the independent application of MLA and GLA to the NLF wing are comparable: both produce less than 1% improvements in cost and more than 3% improvements in fuel burn. While the turbulent designs benefit more from MLA than GLA. The laminar design with its gust-sensitive low-sweep wing stands to benefit more from GLA.

As in the case of the turbulent designs, the greatest performance gains come from the coordinated application of both MLA and GLA. The Laminar MLA+GLA aircraft sees an impressive 15% reduction in fuel burn and a 5% reduction in cost relative to the baseline. The improvement comes from both aerodynamics and structural improvements: a 15% increase in average cruise L/D coupled with a 5% reduction in wing weight.

The planforms of the optimized NLF laminar aircraft are overlaid in fig. 6.11. The combination of MLA and GLA leads to a 24% increase optimized wingspan. Aircraft designed without GLA have smaller wing areas. This is expected as gust load intensity scales linearly with wing area. In the absence of GLA the optimum wing loading increases.

The wing thickness and t/c distributions are compared in fig. 6.12. The significant increases in the outboard t/c in the MLA+GLA wing are once again motivated by the need to increase wing torsional rigidity and improve control authority.

Figure 6.13 shows the wing C_l and $C_{l_{max}}$ distributions in maneuver. Unlike its turbulent counterpart the laminar MLA+GLA aircraft is lift-critical in a 2.5-g maneuver.

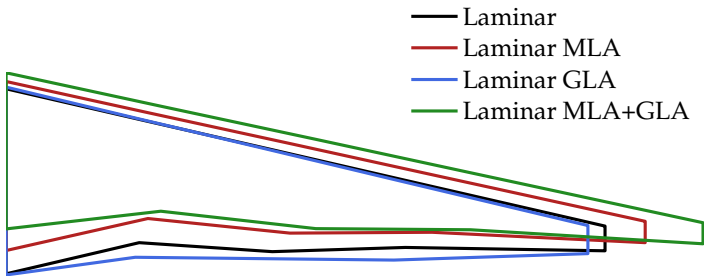

	Laminar	Laminar MLA	Laminar GLA	Laminar MLA+GLA
S_{ref}	0.91	0.83	1.00	0.90
b	1.06	1.14	1.03	1.24
Λ	0.38	0.38	0.38	0.38
$\overline{t/c}$	0.92	0.95	0.94	0.94
AR	1.25	1.55	1.07	1.70

Figure 6.11. A comparison of the optimized laminar wing planforms. All parameters are normalized by their values in the Mach 0.78 turbulent baseline.

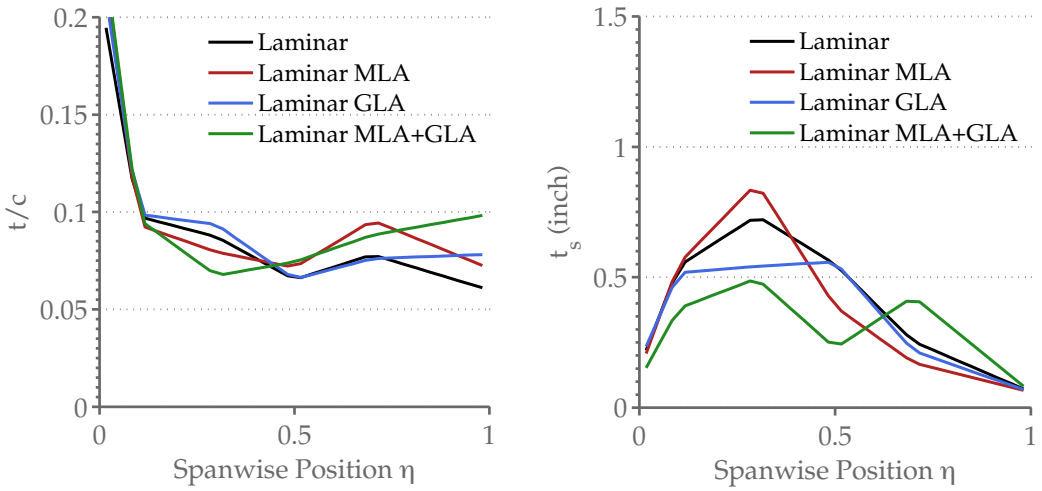

(a) Wing t/c **(b)** Skin Thickness

Figure 6.12. Laminar wing and skin thickness distributions.

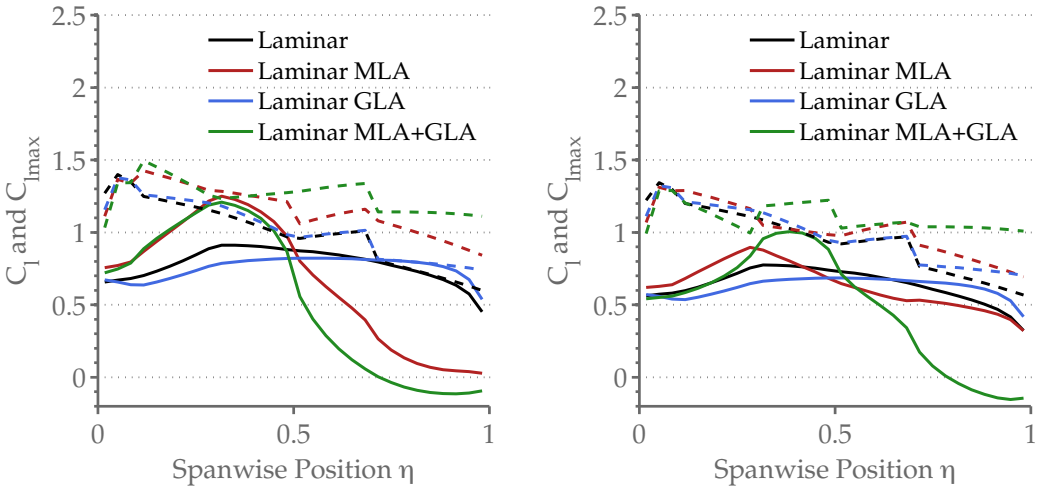

(a) 2.5-g Maneuver **(b)** 1.3-g Maneuver

Figure 6.13. Laminar wing C_l and C_{lmax} distributions.

The maximum lift constraints limit then the effectiveness of the MLA system. Although the reduction in wing sweep has a small, positive effect on maximum lift, the thinner wings need to cope with increased compressibility drag produce a more significant reduction in C_{Lmax}

The normalized maneuver and gust-induced wing stresses are overlaid in fig. 6.14. Solid lines correspond to maneuver loads; dashed lines to the maximum gust loads. Figure 6.14a shows that absent any load alleviation the wing of the laminar aircraft is designed by gust loads inboard and by maneuver loads outboard. When comparing the laminar wing stress distribution to its turbulent counterpart in fig. 6.6a it is clear that a greater portion of the laminar wing is sized by gust. The result is attributable to the low aerodynamic damping associated with the nearly unswept wing.

The stress distributions in fig. 6.14b show that while the MLA system is successfully suppresses the maneuver stresses, gusts continue to size the wing. Similarly, while the GLA system can eliminate the effects of intermediate and long-wave gusts, the maneuvers emerge to become critical design conditions. The simultaneous application

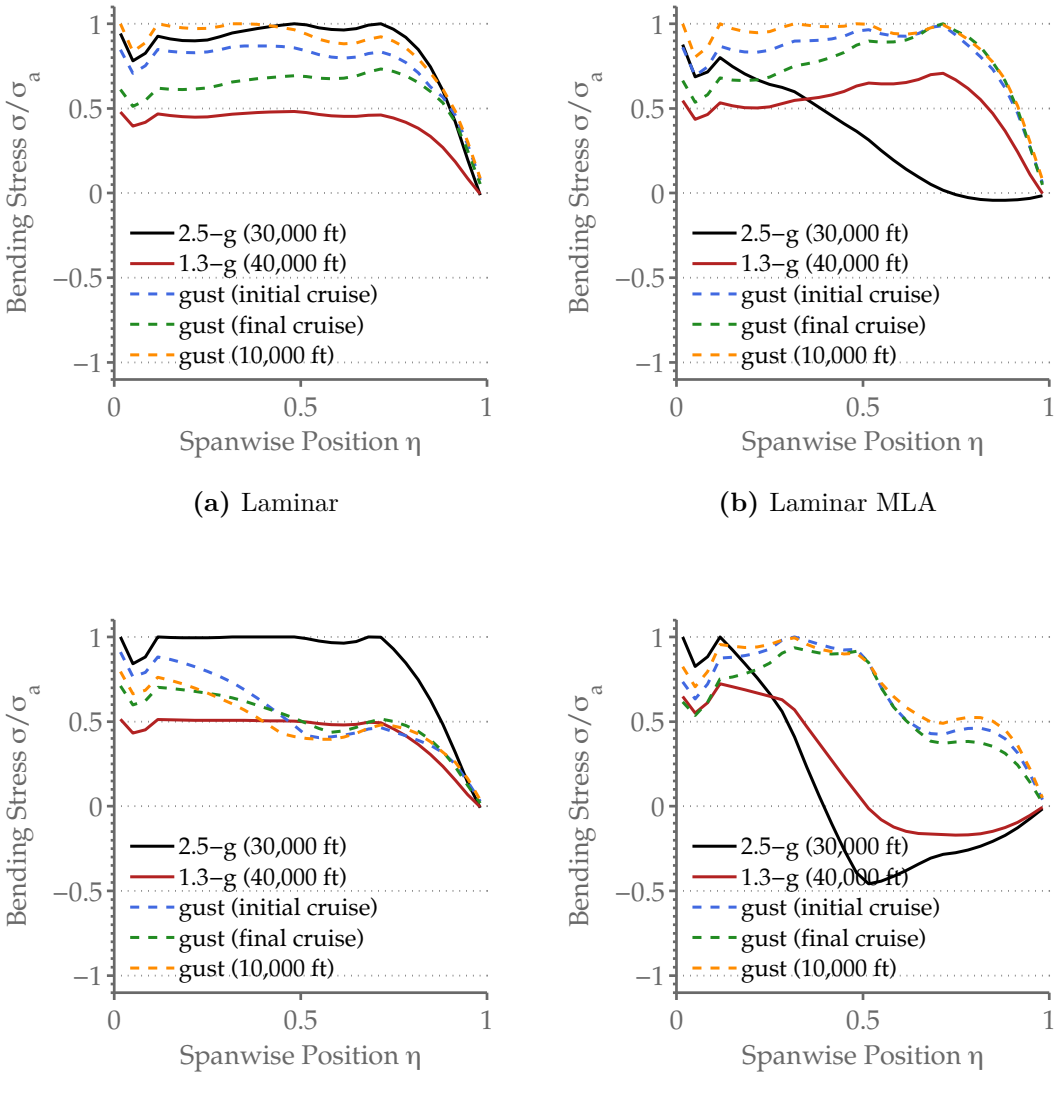

(a) Laminar

(b) Laminar MLA

(c) Laminar GLA

(d) Laminar MLA+GLA

Figure 6.14. Maneuver and gust bending stresses for the optimized laminar designs at Mach 0.78. The wing bending stresses σ are normalized by the allowable stress σ_a. The gust stresses represent the maximum values encounter by each wing section at all gust gradient lengths.

of both load alleviation systems lead to a MLA+GLA design that balances the need to suppress both gust and maneuver loads. The outboard portions of the MLA+GLA wing are once again designed by elastic constraints.

6.2.2 Mach Number Sweeps

The variation in cost and fuel burn performance for the laminar aircraft as a function of the cruise Mach number are shown in figs. 6.15 and 6.16. We observe that the performance of the MLA aircraft is progressively diminished by the need to sustain stronger gust loads at high speed. The more important observation is that the combination of the two load alleviations has unlocked much of the potential of NLF.

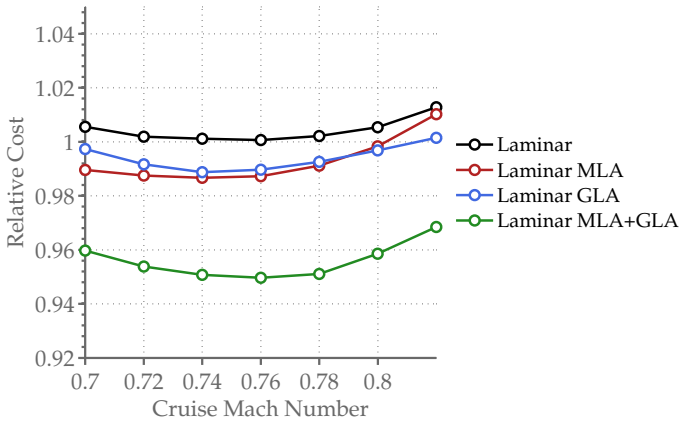

Figure 6.15. A plot of the relative cost of optimized laminar designs as functions of Mach number. Each point represents an optimized aircraft. The performance metrics are normalized to the Mach 0.78 baseline.

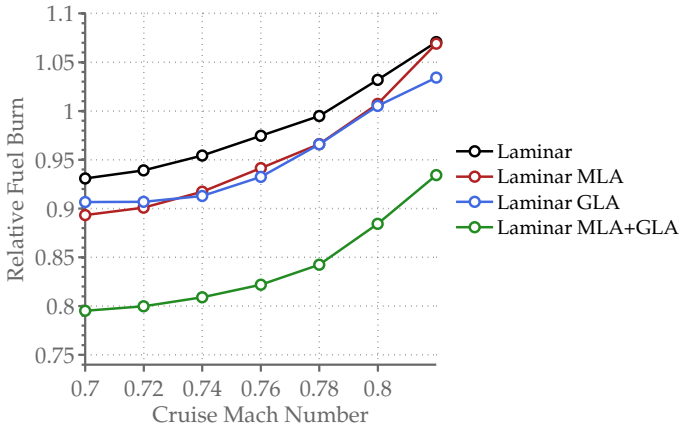

Figure 6.16. A plot of the relative fuel burn of optimized laminar designs as functions of Mach number. Each point represents an optimized aircraft. The performance metrics are normalized to the Mach 0.78 baseline.

6.3 Turbulent and Laminar Comparison

We compare the turbulent and laminar MLA+GLA designs side-by-side in fig. 6.17. In the turbulent design the efficiency gains come primarily from increased structural efficiency though active control. The Laminar MLA+GLA design on the other hand *invests* a portion of the weight savings from load alleviation to enable extensive laminar flow. So while the Turbulent MLA+GLA wing manages to be 24% lighter than the baseline, the corresponding wing weight reduction in the laminar wing is only 9.2%. But the addition of laminar flow has led to a 14.8% improvement in aircraft L/D relative to the baseline while the improvement in the turbulent aircraft L/D is limited to 4.5%. An inspection of the Laminar MLA+GLA design shows extensive laminar flow even in the inboard portions of the wing.

Figures 6.18 and 6.19 show the trends in cost and fuel burn as we change the cruise Mach number. We compare the aircraft designed without any load alleviation with the respective MLA+GLA designs. The results demonstrate that active load alleviation increases the Mach number at which NLF can be efficiently exploited. Without load alleviation, the NLF aircraft has to be designed to cruise at Mach 0.74 or less to realize

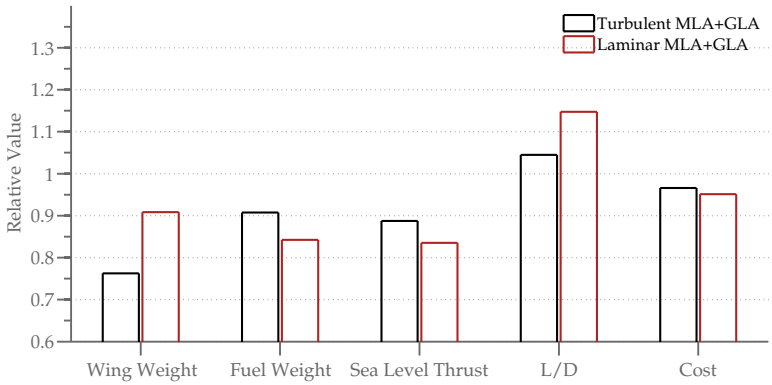

	Turbulent MLA+GLA	Laminar MLA+GLA
Wing Weight	0.762	0.908
Fuel Weight	0.908	0.842
Sea Level Thrust	0.888	0.835
L/D	1.045	1.148
Cost	0.966	0.951

Figure 6.17. A comparison of the optimized MLA+GLA aircraft parameters. The displayed parameters are normalized by the value of the Mach 0.78 turbulent baseline.

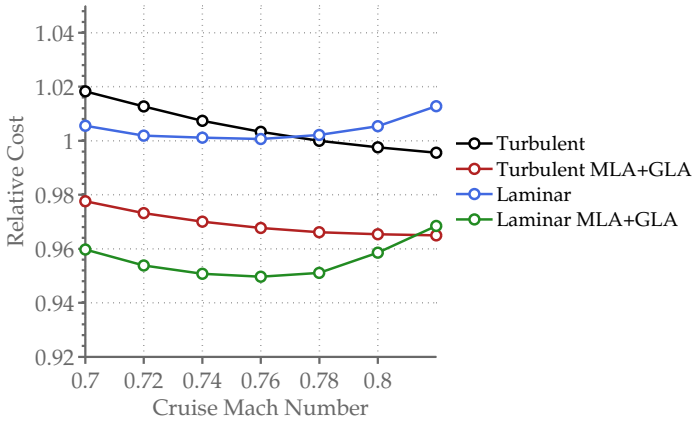

Figure 6.18. Relative cost of turbulent and laminar designs as functions of Mach number.

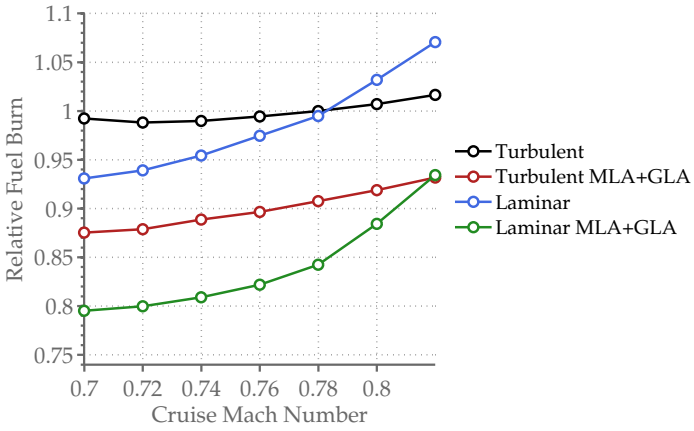

Figure 6.19. Relative fuel burn of turbulent and laminar designs as functions of Mach number.

tangible fuel and cost savings over the turbulent baseline. The Laminar MLA+GLA aircraft on the other hand can achieve savings over turbulent MLA+GLA counterpart at up to Mach 0.80, which match the cruise Mach number of typical airliners. The combination of MLA and GLA therefore alters the terms of the transonic $M\Lambda T$ trade in favor of a low-sweep, natural laminar flow wing. The results presented in this chapter assume conventional aluminum structures and in-service engines. The gains in efficiency are realized through laminar flow, active control and configuration changes. The incorporation of advanced engines and composites would compound the savings.

Chapter 7

Sensitivity Studies

The results presented in chapter 6 are based on a number of important assumptions: 1) the NLF wing sweep are less than 10°, 2) the bottom surface of NLF wings are turbulent, 3) all trailing edge control surfaces are available for load alleviation, 4) the maximum load alleviation control surface deflections and rates are restricted to 10° and 25°/s respectively and 5) there are no gate compatibility constraints on wingspan. Many of these assumptions are operational and difficult to set in conceptual design. Yet changes in these assumptions can have profound impacts on the optimized design. It is instructive therefore to examine the sensitivities of the design studies to changes in our assumptions.

7.1 NLF Wing Sweep

A number of recent studies[11,13] suggest that the 10° limit on the maximum NLF wing sweep is likely conservative. It is not surprising then that the NLF aircraft without load alleviation should compare unfavorably against its turbulent counterpart. The results in the previous chapter demonstrate that a low-sweep transonic NLF wing only becomes viable after the introduction of aggressive load alleviation technologies.

But unsweeping the wing is not the only way to maintain laminar flow. One can certainly tailor the 3-D wing pressure distribution to suppress both T-S and crossflow instabilities.[12,13] For completeness, the performance of a low-sweep NLF wing should be compared to its high-sweep counterpart.

However, the design of a 3-D NLF wing is a non-trivial problem that requires sophisticated flow solvers and transition prediction tools. In this section we use the 2-D inverse design tools at hand to give an *optimistic* estimate of 3-D NLF wing performance. We design the Laminar-25 and Laminar-25 MLA+GLA aircraft in fig. 7.1 with a maximum wing sweep of up to 25°. We assume that the wings of these aircraft are designed with tailored 3-D pressure distributions and/or hybrid laminar flow control (HLFC) technologies to suppress crossflow instabilities without compromising streamwise boundary layer stability. By neglecting all-together the design trade-offs associated with stabilizing the crossflow, we arrive *by definition* at an optimistic projection of what 3-D boundary layer control can achieve.

(a) Laminar-25 **(b)** Laminar-25 MLA+GLA

Figure 7.1. Optimized high-sweep NLF design at Mach 0.78.

Not surprisingly, fig. 7.1a shows that the sweep of the optimized Laminar-25 wing reaches its upper bound of 25°. Without the effect of crossflow the optimizer has every incentive to increase sweep to moderate compressibility drag and increase aerodynamic damping. The wing sweep of the Laminar-25 MLA+GLA design is only 18°– a consequence of the increased effective structural efficiency from load alleviation. The

fact that the load alleviation drives the optimum sweep closer to the low sweep NLF wing is important.

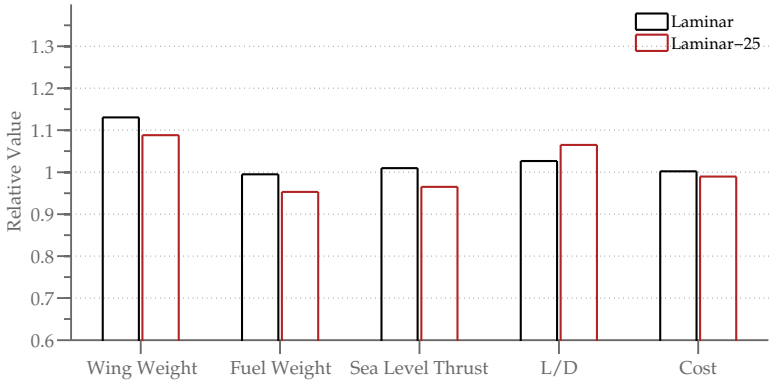

	Laminar	Laminar-25
Wing Weight	1.130	1.088
Fuel Weight	0.995	0.953
Sea Level Thrust	1.009	0.965
L/D	1.027	1.065
Cost	1.002	0.990

Figure 7.2. Comparison of high-sweep laminar-25 aircraft.

We compare the Laminar-25 design with its low-sweep counterpart in fig. 7.2. The table shows that the high sweep NLF wing has a higher L/D and lower wing weight, which combine to produce a 1% reduction in cost and a more than 4% reduction in fuel burn. The Laminar-25 MLA+GLA design in fig. 7.3 on the other hand offers only negligible benefits over its low sweep counterpart. The cost is virtually unchanged and the fuel burn savings amounts to less than 1%. The results confirm that as the load alleviation systems moderate the transonic $M\Lambda T$ trade, the low-sweep NLF wing becomes more and more attractive.

This result is of course a function of the Mach number. The performance of the unswept wing is still constrained at high Mach numbers. Figures 7.4 and 7.5 show the variation of the optimized cost and fuel burn metrics as functions of the cruise Mach numbers. As expected the Laminar-25 designs outperform the low-sweep designs at all Mach numbers. After all the additional wing sweep is "free". However, in

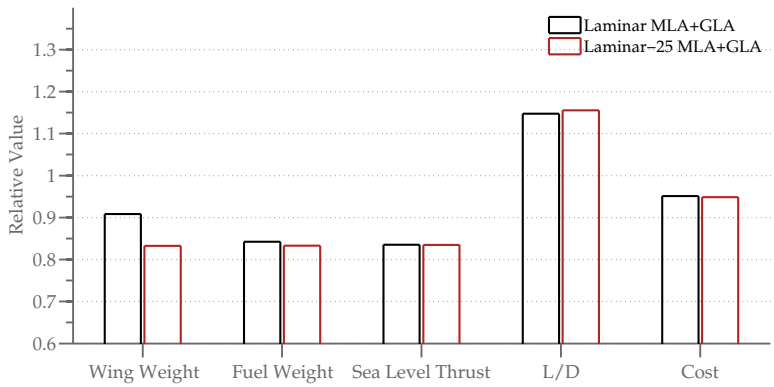

	Laminar MLA+GLA	Laminar-25 MLA+GLA
Wing Weight	0.908	0.832
Fuel Weight	0.842	0.833
Sea Level Thrust	0.835	0.835
L/D	1.148	1.156
Cost	0.951	0.948

Figure 7.3. Comparison of high-sweep laminar-25 MLA+GLA aircraft.

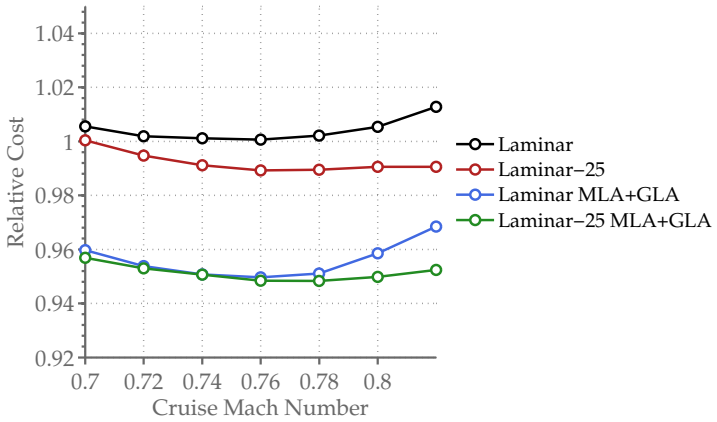

Figure 7.4. Optimized aircraft cost as functions of Mach number.

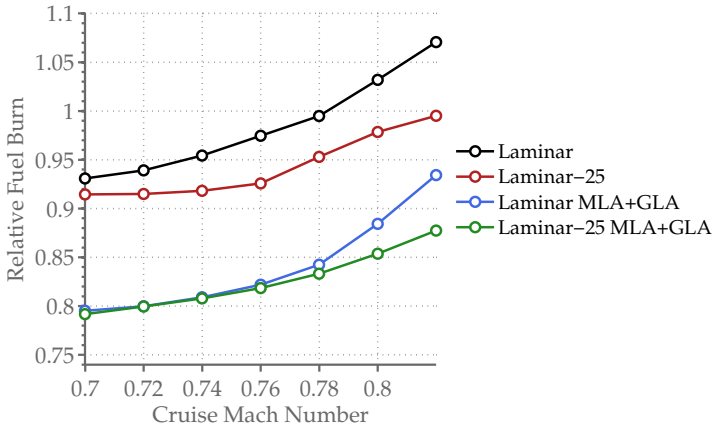

Figure 7.5. Optimized aircraft fuel burn as functions of Mach number.

the MLA+GLA designs the benefits of increased wing sweep are negligible at Mach numbers below 0.78. The results suggest that the combination of active load control and low-sweep NLF wing can be a potential alternative to more sophisticated 3-D NLF wing design and complex active laminar flow control systems.

7.2 MLA and GLA Control Surface Deflection

The effectiveness of the load alleviations systems can be a strong function of the practical range of high speed control surface deflections $\max \delta$. Yet determining the rational bounds on these control deflections is complex problem – one that involves detailed considerations of hinge moment, reserve control authority, aeroelasticity and actuator design and integration. It is instructive therefore to examine the aircraft design sensitivities to changes in $\max \delta$.

Figures 7.6 and 7.7 show the variation in optimized MLA+GLA aircraft cost and fuel burn as functions of the maximum allowable high-speed control surface deflections. The cost and fuel burn trends both flatten beyond a deflection of 10°. The combination of maximum lift constraints, elastic constraints and minimum gauge thickness combine to eliminate further gains from increased deflection bounds. The results

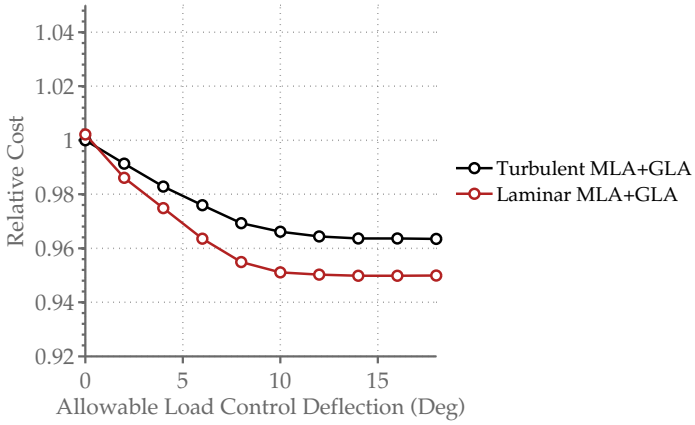

Figure 7.6. Optimized MLA+GLA aircraft costs as functions of maximum load alleviation control surface deflections.

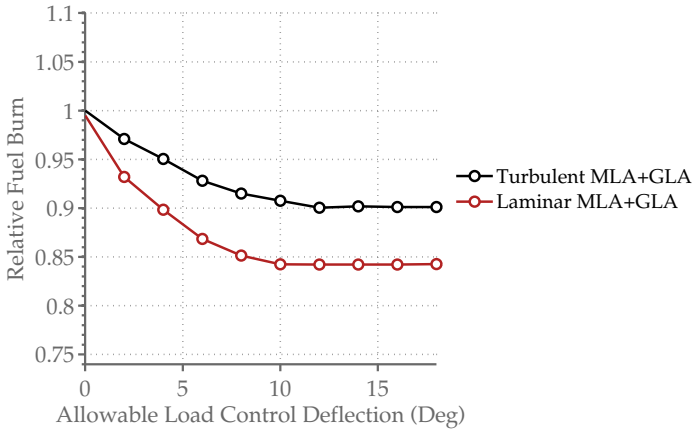

Figure 7.7. Optimized MLA+GLA aircraft fuel burns as functions of maximum load alleviation control surface deflections.

also demonstrate that our assumed MLA and GLA control surface deflection ranges – based on published parameters of existing load alleviation systems – are sufficient to achieve effective load control.

7.3 GLA Control Surface Bandwidth

The effectiveness of the GLA systems is a function of actuator bandwidth. In this section we examine the sensitivity of the aircraft design to changes in actuator bandwidths.

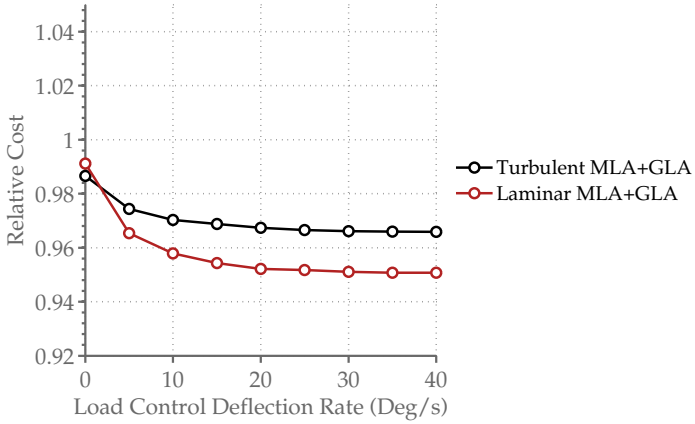

Figure 7.8. MLA+GLA aircraft cost trends as functions of maximum allowable load alleviation control surface deflection rates.

Figures 7.8 and 7.9 show the variation in the optimized MLA+GLA aircraft cost and fuel burn as functions of the maximum control surface deflection rate $\max(d\delta/dt)$. The results confirm that slow actuators can indeed restrict the effectiveness of the GLA system. However, the trends for both the laminar and turbulent aircraft flatten out beyond a rate of 20°/s – a rate that is well within the operating parameters of commercial aircraft ailerons at 35-40°/s.[55] The diminishing returns can mean one of two things: 1) typical aileron actuators are powerful enough to cope with the high frequency gusts specified by the 1–Cosine criteria or 2) if a gust is fast enough to saturate high-speed aileron actuators then it is also probably too fast to substantially

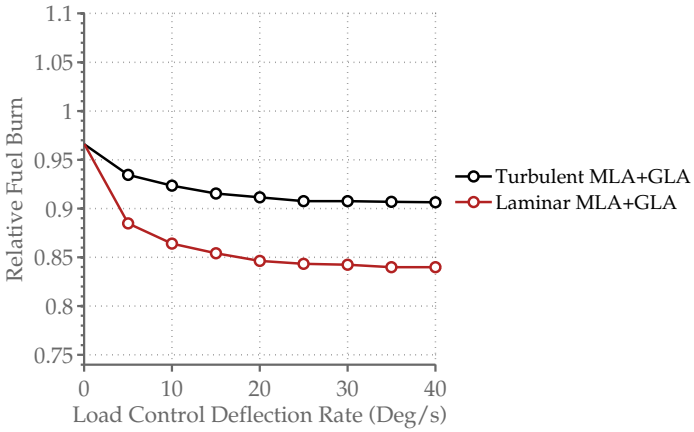

Figure 7.9. MLA+GLA aircraft fuel burn trends as functions of maximum allowable load alleviation control surface deflection rates.

excite the wing structure modes. The consistent rate-saturation of the GLA actuators in the dynamic simulations suggests that the second explanation is likely correct.

7.4 GLA with Only Ailerons

We assume that all trailing edge control surfaces can be used for both MLA and GLA and that all control surfaces can sustain the same deflection rate. However, aircraft flaps are not typically sized as control surfaces. In fact, most flap actuators on commercial aircraft tend to be quite slow – a deflection rate of less than $2°/s$ is typical for complex, multi-slotted flaps[55] . So while flaps can be reasonably allocated to the MLA system to work with anticipated, pseudo-static loads, their utilities in gust encounters are questionable at best.

An conservative approach is to simply remove the flaps from the GLA control system and see how the design might change. To this end we set the two inboard GLA control channel gains to 0. This leaves the outboard control surface deflections δ_3 and δ_4 shown in fig. 7.10 for GLA. The MLA system remains unchanged and can schedule all trailing edge control channels. The control arrangement represents a GLA system

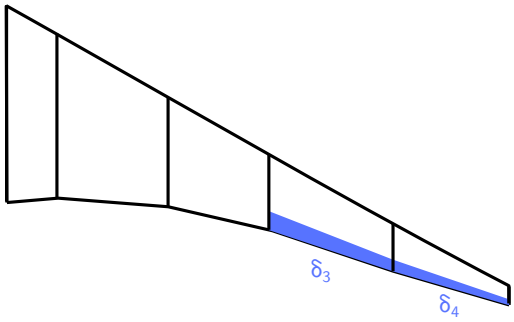

Figure 7.10. GLA using only outboard control surfaces.

that uses only ailerons.

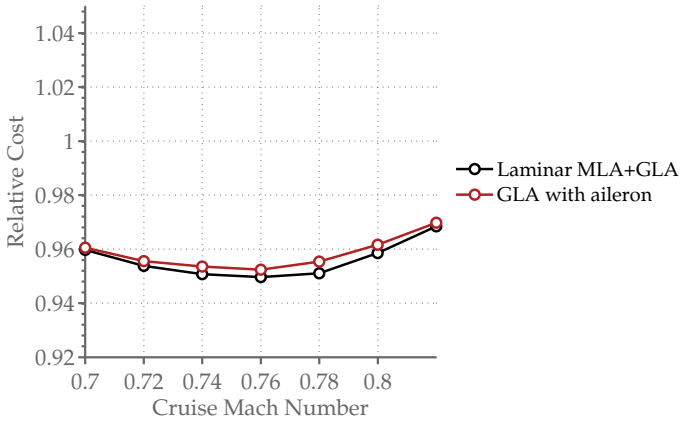

Figure 7.11. Laminar MLA+GLA aircraft cost trends with different GLA control allocations.

The results in figs. 7.11 and 7.12 demonstrate that most of the savings from the GLA can be achieved with the outboard aileron control channels. This result suggests that the control arrangements found on typical airliners should be adaquate for effective GLA.

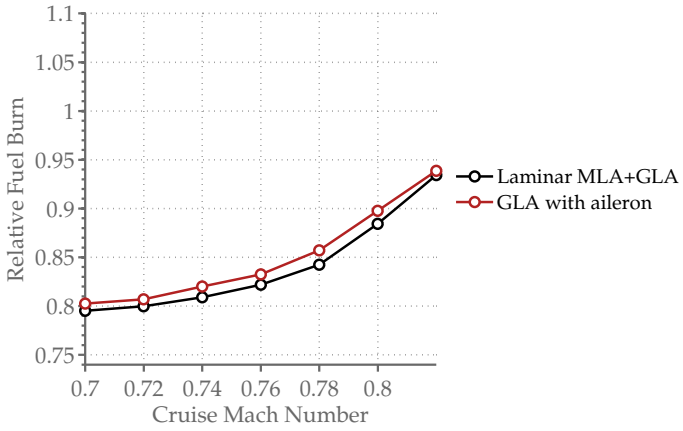

Figure 7.12. Laminar MLA+GLA aircraft fuel burn trends with different GLA control allocations.

7.5 Lower Surface Laminar Flow

We study the sensitivities of the aircraft design to laminar flow on the bottom surface. We add the lower surface transition locations x_{tl} as design variables and impose compatibility constraints to ensure laminar flow up to x_{tl}:

$$Re_x(x_{tl}) < Re_{e^9}(x_{tl})$$

The optimized MLA+GLA aircraft with turbulent and laminar bottom surfaces are compared in fig. 7.13. The similarity between the two aircraft suggests that only modest changes to the pressure distributions are needed to stabilize the lower surface boundary layer.

The normalized aircraft parameters and performance metrics in fig. 7.14 show that maintaining laminar flow on both the upper and lower surfaces nets a tangible 1% improvement in cost and 5% improvement in fuel burn. The total fuel burn reduction over the baseline turbulent design now stands at 20%.

The fuel and cost trends plotted in sections 7.5 and 7.5 confirm that the improvement from lower surface laminar flow are consistent across a wide range of cruise Mach

(a) Laminar MLA+GLA **(b)** Laminar Bottom Surface

Figure 7.13. Comparison of the MLA+GLA aircraft designed with turbulent and laminar bottom surfaces.

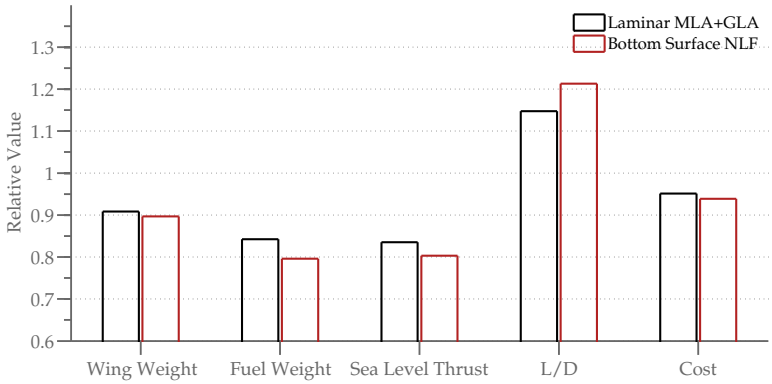

	Laminar MLA+GLA	Bottom Surface NLF
Wing Weight	0.908	0.897
Fuel Weight	0.842	0.796
Sea Level Thrust	0.835	0.803
L/D	1.148	1.213
Cost	0.951	0.939

Figure 7.14. Comparison of the MLA+GLA aircraft designed with turbulent and laminar bottom surfaces.

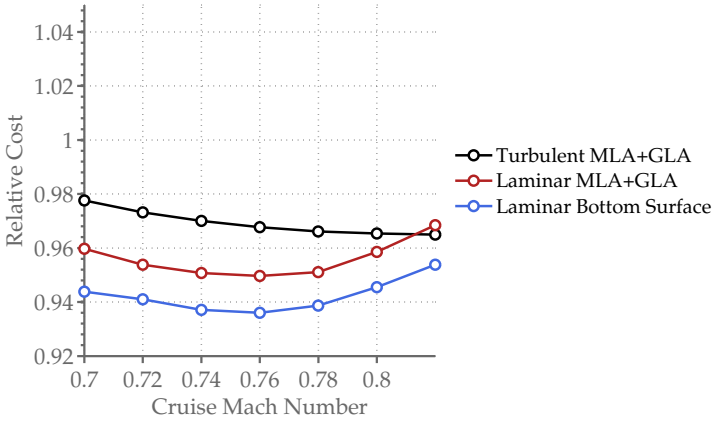

Figure 7.15. Cost trends for the Laminar MLA+GLA aircraft with turbulent and laminar bottom surfaces. The results of the Turbulent MLA+GLA are included for reference.

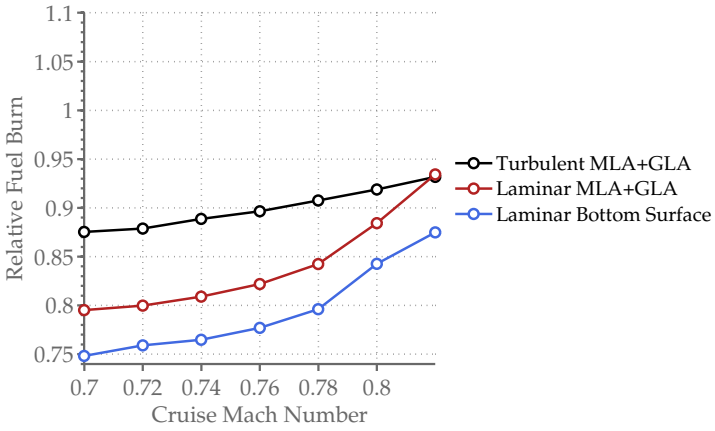

Figure 7.16. Duel burn trends for the Laminar MLA+GLA aircraft with turbulent and laminar bottom surfaces. The results of the Turbulent MLA+GLA are included for reference.

numbers. The plots also demonstrate that achieving laminar flow on the upper surface still accounts for the bulk of the fuel savings.

7.6 Gate Constraints

Active load alleviation systems can greatly increase the wingspan and reduce drag. However, the wingspans of commercial aircraft are limited by more than just stress and aeroelastic constraints. Gate and runway compatibility requirements can restrict the wingspan and pose indirect *operational* constraints on MLA and GLA effectiveness. Figure 7.17 shows the Mach 0.78 Turbulent, Turbulent MLA+GLA and Laminar MLA+GLA aircraft designed with a 120 feet limit on wingspan.

(a) Turbulent **(b)** Turbulent MLA+GLA **(c)** Laminar MLA+GLA

Figure 7.17. A comparison of gate-constrained aircraft.(b<120 ft)

We first ground the analysis with a comparison of the baseline turbulent aircraft designed with and without gate constraints in fig. 7.18. The results, not surprisingly, demonstrate that the baseline is insensitive to the gate constraint.The span restrictions produce only a negligible increase in cost and a modest 2% increase in fuel burn. While the gate constraint reduces the span, the difference is made up in part by reduced wing weight.

The results in figs. 7.19 and 7.20 show that the addition of gate constraints *halves*

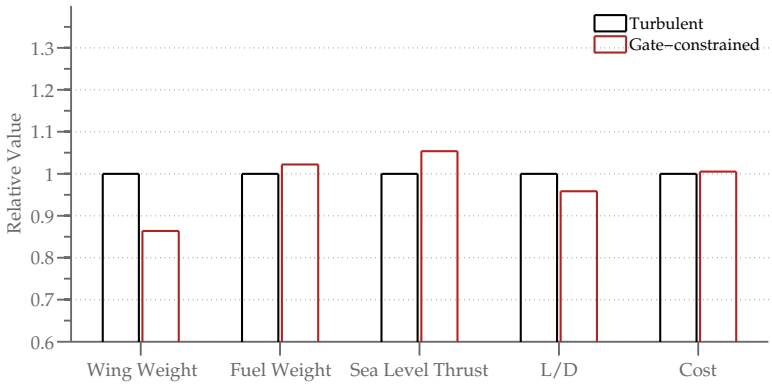

	Turbulent	Gate-constrained
Wing Weight	1.000	0.864
Fuel Weight	1.000	1.022
Sea Level Thrust	1.000	1.054
L/D	1.000	0.958
Cost	1.000	1.005

Figure 7.18. A comparison of the turbulent aircraft designed with and without gate constraints.

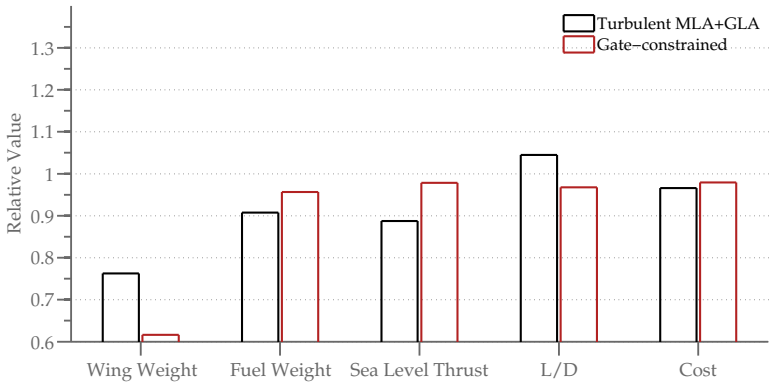

	Turbulent MLA+GLA	Gate-constrained
Wing Weight	0.762	0.616
Fuel Weight	0.908	0.957
Sea Level Thrust	0.888	0.978
L/D	1.045	0.968
Cost	0.966	0.979

Figure 7.19. A comparison of the Turbulent MLA+GLA aircraft designed with and without gate constraints.

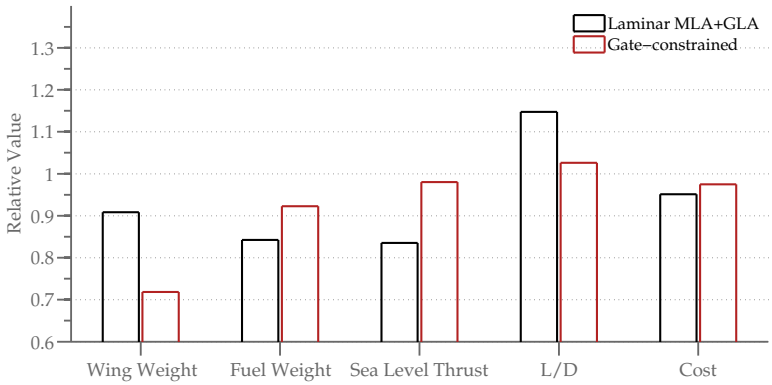

	Laminar MLA+GLA	Gate-constrained
Wing Weight	0.908	0.718
Fuel Weight	0.842	0.923
Sea Level Thrust	0.835	0.980
L/D	1.148	1.026
Cost	0.951	0.975

Figure 7.20. A comparison of the Laminar MLA+GLA aircraft designed with and without gate constraints.

the fuel savings in both the Turbulent and Laminar MLA+GLA aircraft. Unable to increase the span, the optimizer reduces the wing weight to take advantage of load alleviation. Hence gate-constrained wing is 40% lighter than the baseline. But the weight savings cannot match the benefits from increased span. An aggressive load alleviation system may be hard to justify if aircraft remain constrained by existing airport footprints. However, experience show that gate constraints can evolve with new operational realities. The potentials of load alleviation and other new technologies can motivate re-evaluations of aircraft gate constraints.

Chapter 8

Conclusions and Future Work

In this thesis we develop a conceptual aircraft design framework that formally incorporates active load alleviation and natural laminar flow. We design the aircraft concurrently with its load control system. The design framework incorporates both aircraft dynamic simulations and modal solutions of the wing structural dynamics to obtain gust loads. A hybrid-inverse viscous design tool is used to incorporate laminar flow into aircraft design. By directly operating on the wing pressure distribution, we capture the trade-off between structure efficiency, compressibility drag and natural laminar flow.

A series of design studies demonstrates two important results: first, the gains from the *independent* application of MLA and GLA control are modest. This is intuitive: as MLA or GLA reduces one type of stress, other loads can emerge as critical design conditions. Only by combining MLA and GLA can we realize significant improvements in efficiency. Second, active load alleviation can tilt the balance of the transonic aerostructural trade in favor of high-span, low-sweep laminar flow wings. Without load alleviation, a low-sweep NLF wing offers little real advantage over its turbulent counterpart at high transonic speeds. Active load alleviation can increase the Mach number at which NLF can be efficiently exploited. The combination of MLA, GLA and NLF represents therefore a potential alternative to the long-established transonic

paradigm of high-sweep turbulent wing.

The results demonstrate that a minimum cost turbulent aircraft designed concurrently with MLA and GLA control systems can a achieve a significant 10% reduction in fuel burn and 3.4% reduction in cost relative to a baseline design without load control. The efficiency gains come primarily from reduced weight and increased span though active load control. The corresponding NLF aircraft invests the weight savings from load alleviation to enable extensive laminar flow and reduce drag. In this case the fuel and cost savings grow to 15% and 5% respectively.

Sensitivity studies demonstrate that the control requirements for effective active load control are within the parameters of today's aircraft control actuators. We demonstrate that a GLA system that utilizes only aileron to affect load control can be effective. Comparisons with idealized high-sweep NLF wing also suggest that the combination of active load control and low-sweep NLF wing is a potential alternative to more sophisticated 3-D NLF wing design or complex active laminar flow control (LFC) systems.

The design framework developed in this thesis represents only the first step toward the design of more intelligent and responsive wings and their associated load control systems. There is certainly room for improvement.

The development and integration of higher fidelity boundary layer solvers that account for compressibility and crossflow would complete the viscous design. Flutter and its suppression are also important considerations for the high span, flexible wings enabled by load alleviation. Finally, while the application of quasi-steady aerodynamics in the gust simulations is likely conservative,[37] this assumption should be validated.

The most important area of improvement is in the GLA design process. In this thesis we consider only reactive GLA control laws. Future research examine in more detail the performance of different GLA control policies. Detailed exploration of controller design also raises interesting questions of sensor selection and emplacement. Equally important is the needs to account for measurement uncertainties and time delay in

the dynamic simulations.

Sophisticated GLA controller design also requires a more physical description of the gust. The 1–Cosine gust may be the FAR specified design criteria, but it does not reflect the stochastic nature of atmospheric gust, nor does it produce the worst-case gust.[37] And since the 1–Cosine gust is fully characterized by the gust gradient length, it can be anticipated by a sophisticated controller.

The matched filter technique (MFT)[26] and statistical discrete gust (SDG)[28] represent two attempts to address the shortfalls of the 1–Cosine gust in the context of controller design. For linear systems the MFT method exploits superposition to directly solve for the worst-case gust.[26,27,61] The SDG method on the other hand is an extension of the 1–Cosine gust description with stochastic elements.[62] A logical next step is to incorporate SDG or MFT gusts into the design framework and understand their impact on total aircraft design. However, as the gust description becomes more complex, the combinatorial growth in the number of possible gust waveforms may require a completely different optimization strategy.

Finally, aerodynamic load alleviation is by no means the only way to increase the wing structural efficiency. Pfenninger first proposed the strut-braced wing (SBW) in the 1960s as a means to enable wings of very high span or thin wings that are compatible with transonic laminar flow.[63–66] SBW and aerodynamic load alleviation represent therefore two different ways to exploit the same aerostructural synergy. The current design framework can be readily extended to study the relative merits of the different load alleviation schemes and their combined effect on natural laminar flow and aircraft design.

Appendix A

Airfoil Inverse Design

In this appendix we present the results of a series of airfoil optimizations to illustrate the workings of the hybrid-inverse airfoil design tool. The objective in each case is to minimize the sum of the section profile and compressibility drag with respect to the pressure variables. We first presents the results of a point airfoil optimization at a chord Reynolds number of 20 million, a wing sweep of 10° and a freestream Mach number of 0.75. The elastic axis x_e is assumed to be at 43% of the chord. The optimization is subject to pressure distribution, boundary layer and airfoil geometry constraints:

Pressure Distribution

$$M_{x_m} < 1.1$$
$$C_l > 0.4$$
$$C_{m0} > -0.2$$

Transition

$$Re_x(x_t) < Re_{E9}(x_t)$$

Geometry

$$t_{inv}(x_e) > 0.09c$$
$$t_{inv}(x_{TE}) = 0$$

The optimized airfoil geometry, pressure distributions and boundary layer properties are shown in fig. A.1. The airfoil designed at the reference condition has 42 counts of parasite drag with upper surface transition at 60% chord.

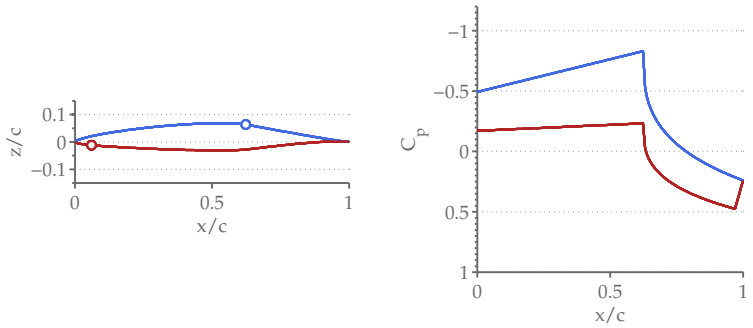

(a) Airfoil **(b)** C_p

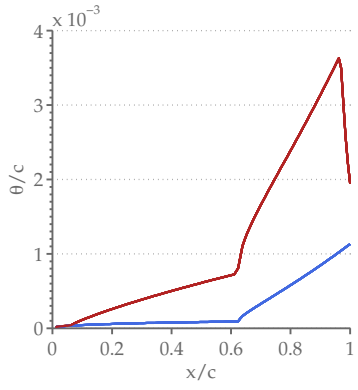

(c) Momentum Thickness

Figure A.1. Example airfoil optimization geometry, C_p and boundary layer momentum thickness results.

In the example optimization we force transition on the bottom surface near the leading edge. There are two reasons for this simplification: 1) the lower surface of an airfoil is responsible for only about 1/3 of the total parasite drag[12] and 2) slat gaps, track

fairings and contaminants can lead to early transition on the bottom surface despite the presence of favorable pressure gradients. Hence only the upper surface transition x_{tu} point is subject to optimization and the transition compatibility is also only imposed on the upper surface. Finally, the constraint on C_{m0} is added to impose a trim penalty on severely aft-loaded airfoil designs.

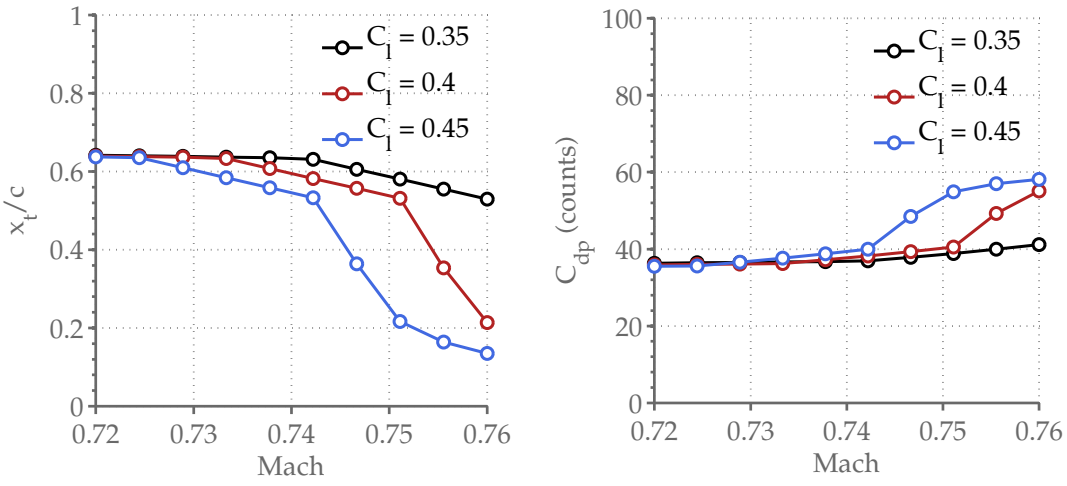

(a) x transition **(b)** C_{dp}

Figure A.2. Optimized airfoil transition and C_{dp} as a function of C_l and $Mach_\infty$. The section t/c and Re_c are fixed at 9% and 20 million respectively.

Figures A.2 and A.3 show the optimized airfoil C_{dp} and x_t as a function of variations in C_l, t/c and M_∞. Each point corresponds to the results of an optimized airfoil. The performance of the low-sweep NLF section is constrained by compressibility: once the maximum M_{x_m} is reached, any increase in M_∞, C_l or t/c has to be compensated by reduced flow acceleration. The result could well be earlier transition and increased drag. The inverse method captures therefore the fundamental tradeoff among structural efficiency, compressibility and laminar flow.

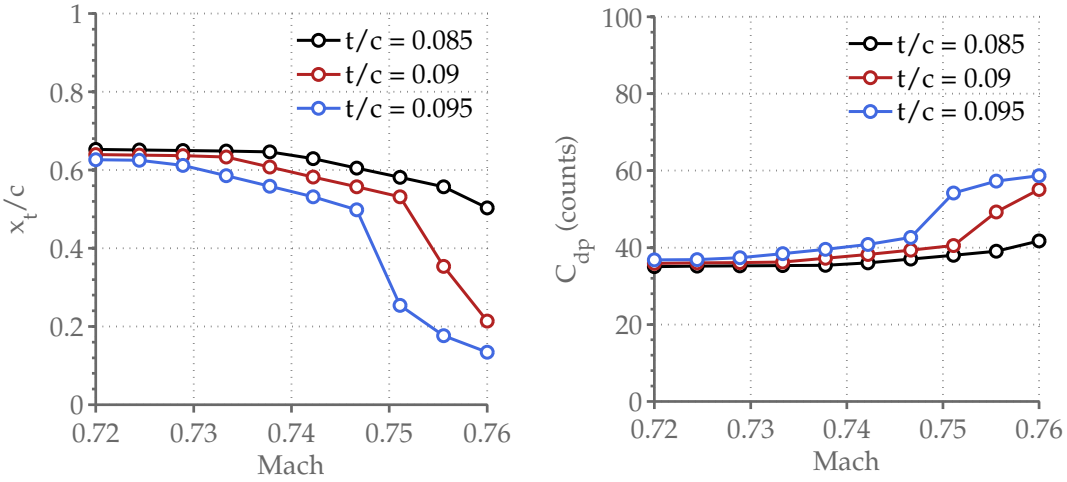

(a) x transition **(b)** C_{dp}

Figure A.3. Optimized airfoil transition and drag as a function of t/c and $Mach_\infty$. The C_l and Re_c are fixed at 0.4 and 20 million respectively.

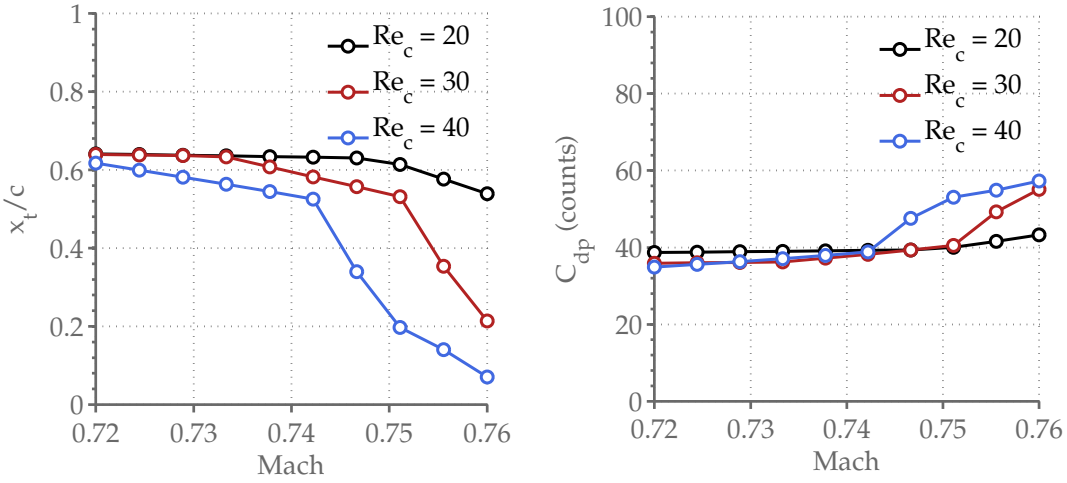

(a) x transition **(b)** C_{dp}

Figure A.4. Optimized airfoil transition and drag as a function of Re_c and $Mach_\infty$. The C_l and t/c are fixed at 0.4 and 9% respectively.

Appendix B

Numerical Solution of Second-Order ODEs

Modal decomposition can be used to decouple a system of ODEs into scalar inhomogeneous second-order ODEs:

$$\ddot{y}_i(t) + 2\zeta_i\omega_i\dot{y}_i(t) + {\omega_i}^2 y_i(t) = \bar{f}_i(t)$$

The transient forced response of each mode i can be solved by the superposition of piece-wise impulse responses at discrete timesteps. The time-marching integration

scheme used in the structural dynamics solver is as follows:[59]

$$
\begin{aligned}
A_0 &= \frac{a}{{\omega_i}^2} - \frac{2\zeta_i b}{{\omega_i}^3} \\
A_1 &= \frac{b}{{\omega_i}^2} \\
A_2 &= y_i(t_0) - A_0 \\
A_3 &= \frac{\dot{y}_i(t_0) + \omega_i \zeta_i A_2 - A_1}{\omega_{di}} \\
B_1 &= e^{-\omega_i \zeta_i \Delta t} \cos(\omega_{di} \Delta t) \\
B_2 &= e^{-\omega_i \zeta_i \Delta t} \sin(\omega_{di} \Delta t) \\
y(t_1) &= A_0 + A_1 \Delta t + A_2 B_1 + A_3 B_2 \\
\dot{y}(t_1) &= A_1 + (\omega_{di} A_3 - \omega_i \zeta_i A_2) B_1 - (\omega_{di} A_2 + \omega_i \zeta_i A_3) B_2
\end{aligned}
$$

Here the solution $y(t)$ is propagated from step 0 to 1. If the timestep Δt is constant then only the A_2 and A_3 coefficients need to be evaluated at every time step.

Appendix C

Cost Model

In this appendix we detail the methods contained in the extended Air Transport Association (ATA) cost model.[60] The cost objective used in the analysis in the previous chapters is the estimated ticket price c_{tic} (\$/pax) in eq. (C.1). In chapters 6 and 7 the ticket price are presented in relative terms against the Mach 0.78 turbulent baseline aircraft. The application reflects the fact that the simple cost model is at best very approximate measure of *relative* economic performance. The methods detailed in this section are heavy on empiricism. They represent a preliminary attempt to inject cost-sensitivity into the design process.

$$c_{tic} = 1.1 \left(\frac{DOC}{100} \frac{N_{seat}}{N_{pax}} R + IOC \right) \tag{C.1}$$

The distinction between N_{seat} and N_{pax} is that the former refers to the number of seats in a one-class configuration while the latter is the number of passengers in the typical 3-class arrangement. The ticket price can be decomposed into *direct* and *indirect* operating component. The next section discusses the buildup of the aircraft direct operating cost (DOC). This is followed by the discussion of the indirect operating cost (IOC).

C.1 Direct Operating Cost

The DOC includes all of the cost items that are associated with the flight operations of the aircraft. This includes the cost of fuel, the pilot (which is deemed essential for flight) and maintenance. Also included in the DOC estimates are the cost to insure the aircraft and the cost of depreciation, which are strong functions of the acquisition cost of the aircraft and the utilization rate. The DOC in cents per seat-mile can be written as:

$$DOC = (c_{fuel} + c_{pilot} + c_{depreciation} + c_{insurance} + c_{maintenance})\frac{100}{N_{seat}}$$

C.1.1 Fuel Cost

We estimate the combined cost of fuel and lubrication oil as a function of thrust, the price aviation fuel p_{fuel} and the price of lubricants p_{oil}:

$$c_{fuel} = \frac{1.02(p_{fuel}W_{fuel} + 0.135p_{oil}N_eT_0)}{R}$$

Unless otherwise specified, the assumed fuel and oil prices are \$2.5/gal and \$20/lb respectively.

C.1.2 Pilot Cost

The pilot cost is correlated to the number and types of engines mounted on the aircraft. For the twin turbofan configuration in this study the following equation is used:

$$c_{pilot} = \kappa_{if}\frac{0.05(W_{MTOW}/1000) + 100}{V_{block}}$$

Where the block speed – an important utilization parameter – is estimated as follows:

$$V_{block} = \frac{R}{T_m + T_{cl} + T_{cr}}$$

Here the climb time T_{cl} and ground and air maneuver time T_m are based on historical data. The cruise time in turn represents a small increase in the flight time.

$$T_{cr} = \frac{1.02R + 20}{\overline{V}}$$

The estimate of the block time is based on the assumption that the climb and descend segments adds no additional distance to the mission. The descent is assumed to incur no additional flight time.

C.1.3 Depreciation and Insurance Costs

The depreciation of the capital value of an airplane is dependent to a large degree on the individual airline and the world economic and competitive conditions as the airplane is maintained in a fully airworthy condition throughout its life.

$$c_{depr} = \frac{c_t + 0.10(c_a) + 0.40N_e c_t}{D_a U_a V_b}$$

The insurance rate is roughly a function of the aircraft total cost and the utilization rate. A typical insurance rate I_{ra} is in the neighborhood of 0.2%. The insurance cost is estimated using the following relationship:

$$c_{insurance} = \frac{I_{ra}(c_t)}{U_a V_b}$$

C.1.4 Maintenance Cost

The aircraft maintenance cost includes both labor and material components. The airframe and engine maintenance costs are computed separately to reflect the different operational cost sensitivities of the different aircraft components. The total aircraft maintenance cost can be written as a sum of the engine and airframe maintenance labor and material costs:

$$c_{maintenance} = 1.8\left[c_{(af,labor)} + c_{(af,mat)} + c_{(en,labor)} + c_{(en,mat)}\right]$$

The material costs are dependent on the engine c_e and the airframe costs c_a. We estimate the engine cost based on a fit of published engine cost to engine T/W. The total aircraft cost is estimated using the per-lb cost of aircraft subsystem collected in Thomas.[60] The weight data of the various components comes from historical data and the PASS aircraft sizing modules. The total aircraft cost is as follows:

$$c_t = (c_a + c_e n_e)$$

Labor Cost

The aircraft maintenance labor costs is composed of per-flight-cycle (landing and takeoff) and per-flight-hour components. The labor man-hours per flight cycle t_{ca} and per flight hour t_{ha} are extrapolated using historical data:

$$\begin{aligned} c_{(af,labor)} &= \frac{\left[t_{ha}(t_{block} - 0.25) + t_{ca}\right] R_L}{R} \\ t_{ca} &= 0.05\frac{W_a - W_e}{1000} + 6 - \frac{630}{\frac{W_a}{1000} + 120} \\ t_{ha} &= 0.59 l_{ca} \end{aligned}$$

The labor rate R_L is a user input and reflects the prevailing wage of aircraft maintenance personal. No inflation factor is applied to the labor cost if up-to-date labor rates

are used. W_a refers to the aircraft empty weight excluding the engine weight. The engine labor cost is also described by per-flight-hour and per-cycle components:

$$c_{(en,labor)} = \frac{(t_{he}t_f + t_{ce})R_L}{R}$$
$$t_{ce} = (0.6 + \frac{0.027T_0}{10{,}000})N_e$$
$$t_{he} = (0.3 + \frac{0.03T_0}{10{,}000})N_e$$

Material Cost

The aircraft material cost $c_{(af,mat)}$ is correlated to the estimated aircraft cost:

$$c_{(af,mat)} = \kappa_{if}\frac{3.08c_at_f + 6.24c_a}{10^6R}$$

The engine material cost $c_{(en,mat)}$ is broken down into per flight hour and per flight cycle components:

$$c_{(en,mat)} = \kappa_{if}\frac{c_{he}t_f + c_{ce}}{R}$$
$$c_{he} = \frac{2.5n_ec_e}{10^5}$$
$$c_{ce} = \frac{2.0n_ec_e}{10^5}$$

C.2 Indirect Operating Cost

Indirect operating costs (IOC) as the name may suggest include airline-specific costs that are not directly connected with the flight of the aircraft. They can include the cost of the cabin crew, landing fees, ground handling labor and even advertising. Indirect costs are operational by nature and can be difficult to define. The IOC is

coarsely estimated using a simple correlation of domestic flight IOC to the maximum takeoff weight and the anticipated load factor LF:

$$IOC = \kappa_{if} \left[-0.04 + 0.00129 \frac{W_{MTOW}}{1000} + 0.00119 n_p + 0.0127 n_p LF \right]$$

Bibliography

[1] Bradley Marty K. and Droney Christopher K. Subsonic ultra green aircraft research: Phase i final report. *NASA Technical Report*, NASA/CR–2011-216847, 2011.

[2] Dev Rajnarayan and Peter Sturdza. *Extensible Rapid Transition Prediction for Aircraft Conceptual Design*, pages 1–15. Number June. 2011.

[3] R. White. Improving the airplane efficiency by use of wing maneuver load alleviation. *Journal of Aircraft*, 8:769, 1971.

[4] PC Arcara Jr, DW Bartlett, and LA McCullers. Analysis for the application of hybrid laminar flow control to a long-range subsonic transport aircraft. Technical report, National Aeronautics and Space Administration, Hampton, VA (United States). Langley Research Center, 1991.

[5] E. Waggoner, R. Campbell, P. Phillips, and J. Viken. Computational design of natural laminar flow wings for transonic transport application. In *Langley Symposium on Aerodynamics,*, volume 1, 1986.

[6] G. Redeker, KH Horstmann, H. Koster, and A. Quast. Investigations of high reynolds number laminar flow airfoils. *Journal of Aircraft*, 25:583–590, 1988.

[7] J. Driver and DW Zingg. Numerical aerodynamic optimization incorporating laminar-turbulent transition prediction. *AIAA Journal*, 45(8):1810, 2007.

[8] U. Cella, D. Quagliarella, R. Donelli, and B. Imperatore. Design and test of the uw-5006 transonic natural-laminar-flow wing. *Journal of Aircraft*, 47(3):783–795, 2010.

[9] J. Lee and A. Jameson. Natural-laminar-flow airfoil and wing design by adjoint method and automatic transition prediction, 2009.

[10] DM Bushnell and MH Tuttle. Survey and bibliography on attainment of laminar flow control in air using pressure gradient and suction, volume 1. *NASA STI/Recon Technical Report N*, 79:33438, 1979.

[11] R.D. Joslin. Aircraft laminar flow control. *Annual Review of Fluid Mechanics*, 30(1):1–29, 1998.

[12] J.E. Green. Laminar flow control-back to the future? *AIAA Paper*, 2008.

[13] Allison Eric and Kroo Ilan. Aircraft conceptual design with laminar flow. 2010.

[14] D.M. Somers. *Design and Experimental Results for a Natural-Laminar-Flow Airfoil for General Aviation Application*. National Aeronautics and Space Administration, Scientific and Technical Information Branch, 1981.

[15] C. Atkin. Laminar flow control: Leap or creep? In *38th Fluid Dynamics Conference and Exhibit, Seattle, Washington*, 2008.

[16] RD Wagner, DW Bartlett, and FS Collier. Laminar flow- the past, present, and prospects. In *AIAA, Shear Flow Conference, 2 nd, Tempe, AZ*, page 1989, 1989.

[17] FA Cleveland. Size effects in conventional aircraft design. *Journal of Aircraft*, 7:483–512, 1970.

[18] J. Szodruch and R. Hilbig. Variable wing camber for transport aircraft. *Progress in Aerospace Sciences*, 25(3):297–328, 1988.

[19] D.L. Carter, R.F. Osborn, J.A. Hetrick, and S. Kota. The quest for efficient transonic cruise. In *7th AIAA ATIO Conference, Belfast, Northern Ireland*, 2007.

[20] R. Hilbig and J. Szodruch. The intelligent wing-aerodynamic developments for future transport aircraft. *27th AIAA Aerospace Sciences Meeting, January 9-12, 1989/Reno,Nevada*, 1989.

[21] S.A. Ning and I. Kroo. Multidisciplinary considerations in the design of wings and wing tip devices. *Journal of Aircraft*, 47(2), 2010.

[22] Airbus. A319/a320/a321 flightdeck and systems briefing for pilots. STL 945.7136/97, 1998.

[23] Airbus. A330 and a340 flight crew training manual. 2004.

[24] SG Lehner, LB Lurati, GC Bower, EJ Cramer, WA Crossley, F. Engelsen, IM Kroo, SC Smith, and KE Willcox. Advanced multidisciplinary optimization techniques for efficient subsonic aircraft design. 2010.

[25] Karr C.L., Zeiler T.A., and Mehrotra R. Determining worst-case gust loads on aircraft structures using an evolutionary algorithm. *Applied Intelligence*, 20(2):135–145, 2004.

[26] R.C Scott, A. Pototzky, and B. Perry. A computer program to obtain time-correlated gust loads for nonlinear aircraft using the matched-filter-based method. *NASA TM*, 109768, 1994.

[27] A. Pototzky and T Zeiler. Maximum dynamic responses using matched filter theory and random process theory. *NASA TM*, 100653, 1988.

[28] JG Jones. Statistical discrete gust method for predicting aircraft loads and dynamic response. *Journal of Aircraft*, 26:382–392, 1989.

[29] GH Watson, K. Gilholm, and JG Jones. A wavelet-based method for finding inputs of given energy which maximize the outputs of nonlinear systems. *International Journal of Systems Science*, 30(12):1297–1307, 1999.

[30] SS Rao. Optimization of airplane wing structures under gust loads. *Computers & Structures*, 21(4):741–749, 1985.

[31] S. Suzuki and S. Yonezawa. Simultaneous structure/control design optimization of a wing structure with a gust load alleviation system. *Journal of Aircraft*, 30(2):268–274, 1993.

[32] J.S. Yang, E. Nikolaidis, and R.T. Haftka. Design of aircraft wings subjected to gust loads: A system reliability approach. *Computers & Structures*, 36(6):1057–1066, 1990.

[33] O. Petersson. Optimization of aircraft wings including dynamic aeroelasticity and manufacturing aspects. *AIAA Proceedings.[np]. 04-07 May*, 2009.

[34] N. Aouf, B. Boulet, and RM Botez. Robust gust load alleviation for a flexible aircraft. *Canadian Aeronautics and Space Journal*, 46(3):131–139, 2000.

[35] A.M. Lucas, J. Valasek, and T.W. Strganac. Gust load alleviation of an aeroelastic system using nonlinear control, 2009.

[36] B. Moulin and M. Karpel. Gust loads alleviation using special control surfaces. *Journal of Aircraft*, 44(1):17, 2007.

[37] K.J. Fidkowski, F. Engelsen, K.E. Willcox, and I.M. Kroo. Stochastic gust analysis techniques for aircraft conceptual design. *AIAA Paper Number 2008-5848, 2008.*, 2008.

[38] J Xu and I Kroo. Aircraft design with maneuver and gust load alleviation. In *29th AIAA Applied Aerodynamics Conference, Honolulu, Hawaii*, 2011.

[39] I.M. Kroo. An interactive system for aircraft design and optimization. *Journal of Aircraft*, 92-1190, 1992.

[40] J.W. Gallman and I.M. Kroo. Structural optimization for joined-wing synthesis. *Journal of Aircraft*, 33(1):214–223, 1996.

[41] J.J. Bertin and M.L. Smith. *Aerodynamics for engineers*. Inc, 1998.

[42] I.H. Abbott and A.E. Von Doenhoff. *Theory of Wing Sections*. Dover, 1959.

[43] S. Wakayama and I. Kroo. Subsonic wing planform design using multidisciplinary optimization. *Journal of Aircraft*, 32(4):746–753, 1995.

[44] G. Bindolino, G. Ghiringhelli, S. Ricci, and M. Terraneo. Multilevel structural optimization for preliminary wing-box weight estimation. *Journal of Aircraft*, 47(2):475–489, 2010.

[45] R.H. Liebeck. Design of subsonic airfoils for high lift. *Journal of Aircraft*, 15(9):547–561, 1978.

[46] BS Stratford. The prediction of separation of the turbulent boundary layer. *Journal of Fluid Mechanics*, 5(01):1–16, 1959.

[47] RC Lock. *An Equivalence Law Relating Three-and Two-Dimensional Pressure Distributions*. HMSO, 1964.

[48] A. Jameson, J.C. Vassberg, and S. Shankaran. Aerodynamic-structural design studies of low-sweep transonic wings. *Journal of Aircraft*, 47(2), 2010.

[49] T. Cebeci and J. Cousteix. *Modeling and Computation of Boundary-layer Flows: Solutions Manual and Computer Programs*. Springer, 2001.

[50] P. Vijgen, SS Dodbele, BJ Holmes, and CP Van Dam. Effects of compressibility on design of subsonic natural laminar flow fuselages. *AIAA Paper*, 1986.

[51] D. Arnal and O. Vermeersch. Compressibility effects on laminar-turbulent boundary layer transition. *International Journal of Engineering Systems Modeling and Simulation*, 3(1):26–35, 2011.

[52] M. Drela and M. Giles. Viscous-inviscid analysis of transonic and low reynolds number airfoils. *AIAA journal*, 25(10):1347–1355, 1987.

[53] J. Cliquet, R. Houdeville, and D. Arnal. Application of laminar-turbulent transition criteria in navier-stokes computations. *AIAA Journal*, 46(5):1182, 2008.

[54] AR Wazzan, C. Gazley Jr, and AMO Smith. Hr-x method for predicting transition. *AIAA Journal*, 19:810–812, 1981.

[55] National Research Council (US). Committee on the Effects of Aircraft-Pilot Coupling on Flight Safety. *Aviation safety and pilot control: understanding and preventing unfavorable pilot-vehicle interactions*. National Academies Press, 1997.

[56] J.R. Fuller. Evolution and future development of airplane gust loads design requirements. SAE International, 1997.

[57] S.S. Rao. *The Finite Element Method in Engineering*. Butterworth-heinemann, 2005.

[58] TY Yang. *Finite Element Structural Analysis*, volume 450. Prentice-Hall Englewood Cliffs, NJ, 1986.

[59] A. Ibrahimbegovic and EL Wilson. Simple numerical algorithms for the mode superposition analysis of linear structural systems with non-proportional damping. *Computers & Structures*, 33(2):523–531, 1989.

[60] E.L. Thomas. Ata direct operating cost formula for transport aircraft. *SAE Technical Papers*, 1966.

[61] T. Zeiler. Matched filter concept and maximum gust loads. *Journal of Aircraft*, 34, 1997.

[62] JG Jones et al. Documentation of the linear statistical discrete gust method, 2004.

[63] W. Pfenninger and C. Vemuru. Design philosophy of long range lfc transports with advanced supercritical lfc airfoils. In *ICAS, Congress, 16 th, Jerusalem, Israel*, pages 223–241, 1988.

[64] JM Grasmeyer, A. Naghshineh, PA Tetrault, B. Grossman, RT Haftka, RK Kapania, WH Mason, and JA Schetz. Multidisciplinary design optimization of a strut-braced wing aircraft with tip-mounted engines. *MAD Center Report MAD*, pages 98–01, 1998.

[65] F.H. Gern, A.H. Naghshineh-Pour, E. Sulaeman, R.K. Kapania, and R.T. HAFTKA. Structural wing sizing for multidisciplinary design optimization of a strut-braced wing. *Journal of aircraft*, 38(1):154–163, 2001.

[66] O. Gur, M. Bhatia, W.H. Mason, J.A. Schetz, R.K. Kapania, and T. Nam. Development of a framework for truss-braced wing conceptual mdo. *Structural and Multidisciplinary Optimization*, pages 1–22, 2010.